



# CURRENT RESEARCH FROM SCIENCE TO TECHNOLOGY

## EDITORS

Prof. Dr. Mehmet ŐİMŐİR

Prof. Dr. Salih Cem İNAN

Assoc. Prof. Dr. Sayiter YILDIZ

Assoc. Prof. Dr. Ebru YABAŐ

**ISBN: 978-625-367-597-4**  
by IKSAD Publishing House







*The editors dedicated this book to the 100<sup>th</sup> anniversary of the Republic of Türkiye. As scientists, we are proud to be citizens of this country.*

# **CURRENT RESEARCH FROM SCIENCE TO TECHNOLOGY**

## **EDITOR**

Prof. Dr. Mehmet ŐİMŐİR

Prof. Dr. Salih Cem İNAN

Assoc. Prof. Dr. Sayiter YILDIZ

Assoc. Prof. Dr. Ebru YABAŐ

## **AUTHORS**

Prof. Dr. Derya ÖZDEMİR DOĞAN, DDS, PhD

Prof. Dr. Mehmet ŐİMŐİR

Prof. Dr. Yahya Kemal TÜR

Prof. Dr. Salih Cem İNAN

Assoc. Prof. Dr. EBRU YABAŐ

Assoc. Prof. Maryam VARAVIPOUR

Assist. Prof. Dr. Betül KAFKASLIOĐLU YILDIZ

Assist. Prof. Dr. Hacımurat DEMİR

Assist. Prof. Dr. Kenan İŐIK

Dr. Dilara ÜLGER ÖZBEK

Prosthodontist, Dt. Betül KARAHASAN, DDS

Ress. Assist. Elif İŐIK

Batuhan KAYA

Elham MOHAMMADIAN

Esra KAYAŐ

Fatih ÖZAYDIN

Kadir ÜNLÜSES

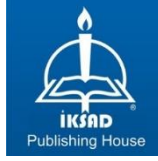
Rahmi CANPOLAT

Sheharyar MUMTAZ

Tufail HABIB

TuĐba ŐANLI

Vildan Fadime DEMİREZEN



Copyright © 2023 by iksad publishing house  
All rights reserved. No part of this publication may be reproduced,  
distributed or transmitted in any form or by  
any means, including photocopying, recording or other electronic or  
mechanical methods, without the prior written permission of the publisher,  
except in the case of  
brief quotations embodied in critical reviews and certain other  
noncommercial uses permitted by copyright law. Institution of Economic  
Development and Social  
Researches Publications

(The Licence Number of Publisher: 2014/31220)

TURKEY TR: +90 342 606 06 75

USA: +1 631 685 0 853

E mail: [iksadyayinevi@gmail.com](mailto:iksadyayinevi@gmail.com)

[www.iksadyayinevi.com](http://www.iksadyayinevi.com)

It is responsibility of the author to abide by the publishing ethics rules.

Iksad Publications – 2023©

**ISBN: 978-625-367-597-4**

Cover Design: Atabek Movlyanov

31.12. 2023

Ankara / Türkiye

Size = 16x24 cm

## **CONTENTS**

**PREFACE**.....1

### **CHAPTER 1**

#### **ANTIBACTERIAL NATURAL DYES AND APPLICATIONS**

Esra KAYAŞ

Rahmi CANPOLAT

Fatih ÖZAYDIN

Prof. Dr. Mehmet ŞİMŞİR.....3

### **CHAPTER 2**

#### **SPECTROSCOPIC TEST TYPES USED IN ANTIOXIDANT CAPACITY DETERMINATION**

Dr. Dilara ÜLGER ÖZBEK .....17

### **CHAPTER 3**

#### **THE PLACE OF ADDITIVE MANUFACTURING IN DENTAL PROSTHESES**

Prosthodontist, Dt. Betül KARAHASAN, DDS

Prof. Dr. Derya ÖZDEMİR DOĞAN, DDS, PhD.....31

### **CHAPTER 4**

#### **COMPRASION of CHARACTERISTICS of METALLIC BIOMATERIALS USED in MEDICAL IMPLANTS**

Vildan Fadime DEMİREZEN

Assist. Prof. Dr. Kenan IŞIK .....47

### **CHAPTER 5**

#### **EVALUATION OF PHYTOREMEDIATION POTENTIAL AND YIELD OF HELIANTHUS ANNUUS UNDER SEWAGE SLUDGE APPLICATION**

Elham MOHAMMADIAN

Assoc. Prof. Maryam VARAVIPOUR .....67

**CHAPTER 6**  
**FLOW CHARACTERISTICS OVER BIO-INSPIRED CORRUGATED AIRFOIL AT LOW REYNOLDS NUMBER**

Assist. Prof. Dr. Hacımurat DEMİR

Batuhan KAYA .....87

**CHAPTER 7**  
**PARAMETERS AFFECTING MICRO ARC OXIDATION PROCESS, BIOCMPATIBILITY AND PARTICLE ADDITION**

Kadir ÜNLÜSES

Prof. Dr. MEHMET ŞİMŞİR

Assoc. Prof. Dr. EBRU YABAŞ .....102

**CHAPTER 8**  
**INVESTIGATION OF LARGE EXTRA DIMENSIONS IN THE MUON COLLIDER**

Prof. Dr Salih Cem İNAN .....125

**CHAPTER 9**  
**DESIGN STRUCTURE MATRIX MODELING FOR SUSTAINABLE PRODUCT DESIGN: A CASE OF THE THERMAL MANAGEMENT SYSTEM OF AN ELECTRIC VEHICLE**

Sheharyar MUMTAZ

Tufail HABIB.....137

**CHAPTER 10**  
**DENSIFICATION AND FRACTURE STRENGTH PROPERTIES OF AL<sub>2</sub>O<sub>3</sub> BASED ZRO<sub>2</sub> AND SM<sub>2</sub>O<sub>3</sub> CONTAINING SANDWICH CERAMIC COMPOSITES**

Tuğba ŞANLI

Assist. Prof. Dr. Betül KAFKASLIOĞLU YILDIZ

Ress. Assist. Elif IŞIK

Prof. Dr. Yahya Kemal TÜR .....155

**CHAPTER 11**  
**DENSIFICATION AND FRACTURE STRENGTH PROPERTIES OF**  
**AL<sub>2</sub>O<sub>3</sub> BASED ZRO<sub>2</sub> AND SM<sub>2</sub>O<sub>3</sub> CONTAINING SANDWICH**  
**CERAMIC COMPOSITES**

Tuğba ŞANLI

Assist. Prof. Dr. Betül KAFKASLIOĞLU YILDIZ

Ress. Assist. Elif IŞIK

Prof. Dr. Yahya Kemal TÜR .....169



## **PREFACE**

While natural sciences try to understand and research nature and its laws, engineering sciences try to develop technology and produce products using these laws. The challenges faced by humans will be overcome with developments in science and technology. The basis of all of these studies is the idea of making humans and the civilization they create more prosperous. The aim of this book is to contribute to studies conducted in many different fields by giving examples. This book presents current research conducted in industry, R&D centers and universities.

Science and technology are advancing very rapidly in every field, and in this sense, it is thought that this book will be a useful resource for researchers and engineers.

Prof. Dr. Mehmet ŞİMŞİR

Prof. Dr. Salim Cem İNAN

Assoc. Prof. Dr. Sayiter YILDIZ

Assoc. Prof. Dr. Ebru YABAŞ

December 2023



## **CHAPTER 1**

### **ANTIBACTERIAL NATURAL DYES AND APPLICATIONS**

Esra KAYAŞ<sup>1</sup>

Rahmi CANPOLAT<sup>2</sup>

Fatih ÖZAYDIN<sup>3</sup>

Prof. Dr. Mehmet ŞİMŞİR<sup>4</sup>

---

<sup>1</sup>ESTAŞ Sivas, Türkiye. esra.kayas@estas.com.tr, Orcid ID: 0000-0001-6505-3216

<sup>2</sup>ESTAŞ Sivas, Türkiye. rahmi.canpolat@estas.com.tr, Orcid ID: 0009-0003-0067-8073

<sup>3</sup>ESTAŞ Sivas, Türkiye. fatih.ozaydin@estas.com.tr, Orcid ID: 0000-0002-0089-373X

<sup>4</sup>Cumhuriyet University, Faculty of Engineering, Department of Metallurgy and Materials Science Sivas, Türkiye. msimsir@cumhuriyet.edu.tr, Orcid ID: 0000-0002-8895-7821



## **1. INTRODUCTION**

Since natural dyes have therapeutic properties in the literature, these dyes have created awareness and the demand for these dyes has increased considerably. Natural dyes are obtained from naturally occurring sources. Among all natural dyes, dyes composed of pigments of plants have extensive medicinal value. The dyestuffs of natural dyes and the medicinal properties of these substances have been known for many years, but their structures and protective properties have only been understood recently. Many of the plants used for dye extraction are classified as medicinal, and some of these have recently been shown to have remarkable antimicrobial activity. New research reveals detailed information about the basic chemistry of the main pigments found in naturally occurring dye-yielding plants and their medical significance, which helps in the further development of pharmaceutical formulations (Chengaiyah et al, 2010).

### **1.1 NATURAL DYES**

Natural dyes are obtained from natural sources without any chemical processing. These natural resources are plants, insects, animals and minerals (Kadolph, 2008). These sources offer a spectrum of beautiful natural colors ranging from yellow to black. These colors are reflected by various organic and inorganic molecules (pigments) and result from the absorption of light in the visible region of 400-800 nm. This absorption of light depends on the structure of the coloring pigment or the components of that pigment. Molecules in the plant contain a variety of chromophores that are present to display the abundance of colors (Bhat et al, 2005). The therapeutic properties of natural products, along with their dyeing properties, are as old as human civilization, and for a long time the main sources of medicines were mineral, plant and animal products (Hernandez-Ceruelos, 2002).

### **1.2 DYE COMPONENTS**

The components of many dyes used in the dye industry are different and the chemicals mostly used in dye production are as follows (Paksoy, 1999);

- Connectors
- Pigments
- Filling materials
- Solvents
- Additives, (Aksongur, 2022).

### • **Connectors**

Binders are the basic components of paint. These substances ensure that the dye is distributed homogeneously within the pigment and filling materials. At the same time, it determines the substances that make up the paint, its properties and qualities. Issues such as the drying method and time of the paint, its compatibility with other layers, the resistance of the dye to external impacts, the way of application, its brightness and its behavior on the surface on which it is applied are the main characteristics of the paint. There are many types of binders and the most used ones are as follows ([http://bosad.org.tr/beneficial\\_information/dye\\_rawmaterial/TR/p2,5-21](http://bosad.org.tr/beneficial_information/dye_rawmaterial/TR/p2,5-21));

- Polyesters
- Alkyd Resins
- Cellulosic Resins
- Polyurethane Resins
- Vinyl Resins
- Acrylic Resins
- Epoxy Resins

### • **Chemistry of pigments**

Pigments are molecules that create the colors of all objects in nature. ([http://www.nanopolchemical.com/pigment-what are/](http://www.nanopolchemical.com/pigment-what%20are/)). Pigments provide an aesthetic appearance to the dye, creating a more beautiful appearance. At the same time, they prevent or delay the decay of the dye by absorbing the radiation in sunlight. Thanks to their inhibitory properties, pigments passivate the metal surface, have a galvanic effect and provide cathodic protection to the metal surface (Gürü and Yalçın, 2006). They are also found in foods and give foods their own color. For example; The main components of tomatoes are lycopene,  $\alpha$  and  $\beta$ -carotene, lutein, zeaxanthin and  $\beta$ -cryptoxanthin. Lycopene is a type of carotenoid found in tomatoes and is responsible for the red color of the fruit. 80-90% of the total amount of carotenoids in red ripe tomatoes consists of pigments. Beta carotene, the yellow pigment of carrots, is an isomer of lycopene (Shi and Maguer, 2000).

### • **Filling materials**

The purpose of using fillers is generally to reduce the cost of a particular dye formulation. In addition, it also affects the dye's properties such as fluidity, viscosity, slump stability and film strength. The sealing power of a filling material is related to its refractive index. The refractive index of

titanium dioxide is 2.7 and since it is above 1.7, this filler is considered a pigment. Some of the fillers used in dye production are as follows (<https://www.turkchem.net/filling-of-pigments-dye-and-of-plastic-impact-and-social.html>);

- Calcium Carbonate (Calcite)
- Talc (Mg Silicate)
- Talc (Mg Silicate)
- Titanium Dioxide
- Barite (BaSO<sub>4</sub>)

#### • **Solvents**

Solvents make the dye more fluid. Solvent types are very effective on dyes. Although many situations such as good adhesion of dyes to the surface and the brighter and smoother surface of the dye after drying depend on the type of solvent, solvents also affect the drying time, fluidity and application properties of the dye.

The solvent is selected according to the type of dye. For example; The resin and solvent must contain chemicals with a similar structure. Thinners, on the other hand, are chemicals used only to adjust viscosity and are distinguished from solvents in this respect (Gürü and Yalçın, 2006).

### **1.3 NATURAL COLORANTS**

Natural colorants are classified in various ways depending on functional groups (Structure) and Color Shades.

#### • **Flavonoids**

Flavonoids are found exclusively in epidermal cells in plants. They are classified in the aromatic oxygen group containing heterocyclic pigments. At the same time, it has a polyphenolic structure and is abundant in many plants, fruits and vegetables. According to the results of the research, it has been seen that it is one of the groups that has been most researched recently (Yenishlieva and Marinova, 2001).

Naturally obtained colorants are more preferred because they are healthier and perform better. Many synthetic colorants are banned because they cause allergy-like symptoms or cancer. This situation has increased the demand for natural colorants. Natural dyes are widely used in the cosmetic industry. The reasons for this are that it has no side effects today, UV protection and anti-aging properties. There are more than 450 plants in India

that can produce dyes. Some of these plants have medicinal value as well as dyeing properties. Natural dyes are environmentally friendly, for example turmeric, the brightest of the naturally occurring yellow dyes, is a powerful antiseptic that revitalizes the skin, while indigo gives a cooling sensation (Siva, 2007).

(Singh et al., 2005) examined the antimicrobial activity of some natural dyes. Optimized natural dye powders from *Acacia catechu* (L.f.) Willd, *Kerria lacca*, *Rubia cordifolia* L. and *Rumex maritimus* were commercially obtained and showed antimicrobial activity. Plant by products are potential sources of valuable components such as polyphenols, tannins, flavonoids and many other bioactive compounds with a wide range of antibacterial activities (Morais et al., 2016 ; Bhuyan et al., 2016 ). After natural dyes began to be used in textiles, research on antibacterial colorants began. Research has generally focused on the natural antibacterial activity of plant natural colorants and the antibacterial properties of fabrics dyed with natural dyes. They mainly focused on the use of aluminum (Al), iron (Fe), copper (Cu), chromium (Cr), cobalt (Co), tin (Sn) and nickel (Ni) metal salts for enrichment purposes (Ghaheh et al., 2012; Ghoranneviss and Shahidi, 2013). However, although the use of metal salts improves color quality and has antibacterial properties, it also causes environmental problems. The use of biomordants and natural antibacterial treatments for natural dyeing of textiles has received more attention due to increased environmental awareness to avoid hazardous metallic salts ( Dong et al., 2018 ; Saleem and Saeed, 2020 ).

According to some studies, when fibers are dyed or mordanted with plant compounds containing phenolic and terpenoids, essential oils, alkaloids, lectins, polypeptides and polyacetylenes, they have high color quality and antibacterial properties (Joshi et al., 2009).

Therefore, due to increasing environmental awareness and their toxicity or non-biodegradable nature and harmful effects, the use of synthetic dyes is gradually decreasing and being replaced by natural dyes. Additionally, the use of natural dyes does not create any waste problems. Moreover, natural dyes cannot completely replace synthetic dyes, but they have their own place in the market (Prabhu and Bhute, 2012). On the other hand, although the price range and color palette of synthetic dyes are wider than natural dyes, these dyes can cause allergies, toxic waste and harm to the human body (Samanta and Agarwal, 2006).



Therefore, due to increasing environmental awareness and their toxicity or non-biodegradable nature and harmful effects, the use of synthetic dyes is gradually decreasing and being replaced by natural dyes. Additionally, the use of natural dyes does not create any waste problems. Moreover, natural dyes cannot completely replace synthetic dyes, but they have their own place in the market (Prabhu and Bhute, 2012). On the other hand, although the price range and color palette of synthetic dyes are wider than natural dyes, these dyes can cause allergies, toxic waste and harm to the human body (Samanta and Agarwal, 2006).

#### **1.4 MEDICAL IMPORTANCE OF NATURAL DYES**

Natural dyes are used in textiles, paper, wood, etc. It is used to add color to an endless variety of materials, such as, and is also widely used in the cosmetics, food and pharmaceutical industries.

Plants used in natural dyeing contain different chemical components in their structures. Therefore, they have different antibacterial effects and many different properties (Han and Yang, 2005; Singh et al., 2005). One of these features is that they have wide medical importance in the pharmaceutical industry. Some important natural dye plants are:

- **Turmeric:** Commonly known as Indian saffron. It consists of dried and fresh rhizomes of the *Curcuma longa* Linn plant.

- The main component of curcuminoids is known as “curcumin”. Chemically, curcuma species contain essential oils, starch and curcumin (50 – 60%). It is reported that curcumin and other related curcuminoids are responsible for the yellow color of the dye (Kokate et al., 2007).

- **Safflower:** Safflower (*Carthamus tinctorius* L.) is an oilseed plant and has been used in agriculture since the past as a source of red dye (cartamine). The main components of aspirin are cartamine and cartamidine. Cartamine is responsible for producing red dye and cartamidine is responsible for producing yellow dye. Cartamine is insoluble in water, whereas cartamidine is soluble in water (Kizil et al., 2008). In addition to its coloring properties, safflower leaves are also used in the treatment of many chronic diseases such as hypertension, coronary heart diseases, rheumatism, male and female fertility problems (More et al., 2005), (Rajvanshi, 2005). It is obtained from Carthamine flowers and is used as an infusion in the treatment of diseases related to the circulatory system (Carapetian and Zarei, 2005).

- And other components saffron yellow, arctigenin, tacheloside, N-feruloyltryptamine, N-feruloylserotonin, steroids, flavonoids, polyacetylenes (Takahashi, 1982).

### **1.5 ANTIBACTERIAL FEATURES IN DYES**

Today, factors such as changing living conditions, increased public transportation, changing eating habits and increased international travel cause microorganisms to easily pass from individual to individual in public living spaces, resulting in an increase in infectious diseases. Since microorganisms can easily reproduce in moist environments, these environments are very risky places. When the amount of microorganisms on living things exceeds a certain level, it can cause infectious diseases of varying severity depending on personal and environmental factors, and more importantly, epidemic diseases. For this reason, we take precautions in our daily lives to prevent the damage caused by microorganisms in the environment we live in. Medical, textile, etc. with antibacterial properties. The need for products is increasing day by day (Palamutçu et al., 2009; Hussein et al., 1997). Since the chemical components of plants are different from each other, their antibacterial effects also vary.

Studies are being carried out to increase the antibacterial effect of textile products belonging to different sectors such as health, security, informatics and cosmetics, without causing changes or deterioration in the appearance of the product or the comfort of use. Apart from medical textiles, people prefer clothes such as baby clothes, upholstery, sportswear, socks and towels to have antibacterial properties (Ezgi and Bulut, 2013).

Textile products, in terms of their structure and the places they are used, are environments that provide suitable temperature, humidity and nutrients for microorganisms to live and multiply. Microorganisms settled between textile fibers can harm the textile product and the user. The bacterium that causes this condition enters the cell membrane and opens the phospholipid layer. In this case, the cell begins to take in water and explodes when it takes in too much water. In this case, the membrane balance of the cell is disrupted and the cell dies (Shahidi and Naczki, 2006; Tavassoli and Djomeh, 2011). Considering these situations, efforts are being made to reduce the negative effects caused by microorganisms by adding antibacterial properties to textile products.

These products are produced to prevent odor, staining, color change, product deformation, allergic effects and various diseases that come with it, and to prevent possible infections (Thiry, 2001). Products can be given an antibacterial effect if the fibers used have this feature or by using antibacterial substances in textile weaving processes or plants with antibacterial properties used in natural dyeing.

Some plants that have antibacterial effects are:

• ***Lavender***

Lavender is from the Labiatae family. *Lavandula stoechas* and *L. Angustifolia* species are widely found in Turkey. In many studies, it has been determined that lavender oil has an antioxidant effect (Yang et al., 2010). It has been shown that it has a high level of activity in the 2,20-diphenylpicrylhydrazil (DPPH) free radical scavenging test (Yang et al., 2010). In addition, in this study, it was shown that linoleic acid, one of the important components of lavender oil, prevented peroxidation by 58% in the lipid peroxidation test.

In another study; A 1,1-diphenyl-2-picrylhydrazil (DPPH) free radical scavenging test was performed on the saliva secretions of people smelling lavender oil and it was determined that there was an increase in free radical scavenging activation. This effect of lavender oil is attributed to its effect on the intersympathetic nervous system. In another study; It was determined that there were improvements in the testicles of rats to which lavender oil was applied along with formaldehyde exposure. It is stated that this improvement is due to the antioxidant effect of lavender oil. The main active ingredients it contains are; 1,8-Cineole, Linalol, Camphor, Linalyl acetate, Caryophyllene.

• ***Clove***

The essential oil called "eugenol" is what gives cloves its scent and flavor. Eugenol, which is insoluble in water but easily soluble in alcohol or oil, is the antioxidant source of cloves and is the substance that makes up the majority of cloves. A study has shown that clove has strong antiseptic, antifungal, antiviral and local anesthetic effects. For this reason, clove has long been used as a pain reliever for toothaches. In skin care, it is used in acne treatment and wound healing due to its antiseptic properties, and in the treatment of herpes due to its antiviral properties (Çoban and Patır, 2010).

• **Rose**

Rose (*Rosa damascena* Mill.) belongs to the Rosaceae family. It is produced from the flowers of these plants with four basic products: rose oil, rose water, concrete and absolute. rose flower; It is widely used in natural dyeing as well as in the fragrance, cosmetics and perfume industries. Also dried rose flower; It is also used in herbal tea production, aromatherapy and hydrotherapy. Although rose water has a high degree of antibacterial effect, some bacteria can cause rose water to spoil (Baydar, 2009).

In a study conducted by (Özkan et al., 2004); They found that rose pomace has an antiradical and antioxidant effect at least as high as the fresh flower, and that it has an antibacterial effect against many bacteria, especially *Salmonella enteritidis*, *Mycobacterium smegmatis* and *Aeromonas hydrophilla*.

• **Oregano**

It belongs to the thyme (*Thymus vulgaris*) species. It is mostly used as a spice. It contains high amounts of pigments for yellow color when used in dyeing. According to recent studies, people use this plant in wool dyeing in the Taurus Mountains. The common feature of thyme species that are widely used and traded in our country is that they contain essential oils and the main components of these essential oils are thymol and carvacrol. These substances are phenolic compounds that give thyme its unique smell and antioxidant properties. These compounds constitute 78–82% of essential oils (Botsoglou et al., 2003). The dyestuff contained in the thyme plant is Luteolin (Natural Painting, 2007).

• **Turmeric**

*Curcuma longa* L., belonging to the Zingiberaceae family, is a perennial herbaceous plant with yellow flowers. In the past, turmeric was used instead of litmus paper. Although it is mostly used as a colorant and condiment in food; It is also used in dyeing silk, wool and fine leather. The dye it contains is curcumin (Doğal dyeing, 2007). Turmeric contains tetrahydrocurcumin, an odorless, heat-stable, antioxidant compound. Curcuminoids (curcumin, demethoxy curcumin, bisdemethoxy curcumin) constitute the main component of turmeric. The molecular formula of curcumin, which melts at 184°C, is C<sub>21</sub>H<sub>20</sub>O<sub>6</sub> and constitutes 3-5% of turmeric.

## REFERENCES

- Aksongur, (2022) Boron-Based Antibacterial Dye Production and Characterization. Gazi University, Institute of Science and Technology, Master's Thesis, Ankara, 1-86pp.
- Baydar, H. (2009). Book of Medicinal and Aromatic Plants Science and Technology. *Extended*, 3, 229-230.
- Benli, M., & Yiğit, N. (2005). Antimicrobial activity of the thyme (*Thymus vulgaris*) plant, which is widely used in our country. *Orlab On-Line Microbiology Journal*, 3(8), 1-8.
- Bhat, S. V., Nagasampagi, B. A., & Sivakumar, M. (2005). *Chemistry of natural products*. Alpha Science Int'l Ltd..
- Bhuyan, S., Gogoi, N., & Kalita, B. B. (2016). Natural dyes and its Antimicrobial effect. *Int. J. Eng. Trends Technol*, 42(3), 102-105.
- Botsoglou, N. A., Grigoropoulou, S.H., Botsoglou, E., Govaris, A., & Papageorgiou, G. (2003). The effects of dietary oregano essential oil and  $\alpha$ -tocopheryl acetate on lipid oxidation in raw and cooked turkey during refrigerated storage. *Meat science*, 65(3), 1193-1200
- Carapetian, J., & Zarei, G. (2005). Variation in Protein, oil and fatty acid contents in three wild species of safflower (*Carthamus*) from West Azerbaijan, Iran. *International Journal of Botany*.
- Chengaiyah, B., Rao, K. M., Kumar, K. M., Alagusundaram, M., & Chetty, C. M. (2010). Medicinal importance of natural dyes-a review. *International Journal of PharmTech Research*, 2(1), 144-154.
- Çoban, Ö. E., & Patır, B. (2010). Use of some herbs and spices with antioxidant effects in foods. *Electronic Journal of Food Technologies*, 5(2), 7-19.
- Dong, G., Liu, H., Yu, X., Zhang, X., Lu, H., Zhou, T., & Cao, J. (2018). Antimicrobial and anti-biofilm activity of tannic acid against *Staphylococcus aureus*. *Natural product research*, 32(18), 2225-2228.
- Duke, J. A. (2002). *Handbook of medicinal herbs*. CRC press.
- Ezgi, A. K. A. R., & Bulut, M. (2013). Test methods used for antibacterial properties and activity of some textile dye plants. *Journal of Technical Sciences*, 3(2), 1-6.
- Ghaheh, F. S., Nateri, A. S., Mortazavi, S. M., Abedi, D., & Mokhtari, J. (2012). The effect of mordant salts on antibacterial activity of wool fabric dyed with pomegranate and walnut shell extracts. *Coloration Technology*, 128(6), 473-478.

- Ghoranneviss, M., & Shahidi, S. (2013). Effect of various metallic salts on antibacterial activity and physical properties of cotton fabrics. *Journal of Industrial Textiles*, 42(3), 193-203.
- Gürü, M. and Yalçın, H. (2006). Materials Information (Second Edition). Ankara: PALME Publishing, 263-306.
- Han, S., & Yang, Y. (2005). Antimicrobial activity of wool fabric treated with curcumin. *Dyes and pigments*, 64(2), 157-161.
- Hernandez-Ceruelos, A., Madrigal-Bujaidar, E., & De La Cruz, C. (2002). Inhibitory effect of chamomile essential oil on the sister chromatid exchanges induced by daunorubicin and methyl methanesulfonate in mouse bone marrow. *Toxicology letters*, 135(1-2), 103-110.
- Hussein, S. A., Barakat, H. H., Merfort, I., & Nawwar, M.A. (1997). Tannins from the leaves of punica granatum. *Phytochemistry*, 45(4), 819-823.
- Joshi, M., Ali, S. W., Purwar, R., & Rajendran, S. (2009). Ecofriendly antimicrobial finishing of textiles using bioactive agents based on natural products.
- Kadolph, S. (2008). Natural dyes: a traditional craft experiencing new attention. *Delta Kappa Gamma Bulletin*, 75(1), 14.
- Kizil, S., Çakmak, Ö., Kirici, S. A. L. İ. H. A., & İnan, M. (2008). A comprehensive study on safflower (*Carthamus tinctorius* L.) in semş-arid conditions. *Biotechnology & Biotechnological Equipment*, 22(4), 947-953.
- Kokate.C.K, Purohit.A.P, Gokhale.S.B, Test book of Pharmacognosy, Edition no:39, 2007, 414-415.
- Morais, D. S., Guedes, R. M., & Lopes, M. A. (2016). Antimicrobial approaches for textiles: from research to market. *Materials*, 9(6), 498.
- More, S. D., Raghavaiah, C. V., Hangarge, D. S., Joshi, B. M., & Dhawan, A. S. (2005). Tolerant genotypes and management for alleviation of salinity stress in safflower (*Carthamus tinctorius* L.) in India. In *Proceedings of the VIth International Safflower Conference, İstanbul-Turkey, 6-10 June, 2005. SAFFLOWER: a unique crop for oil spices and health consequently, a better life for you* (pp. 3-186). Engin Maatbacilik Ltd. Scedilla~ ti.
- Özkan, G., Sagdıç, O., Baydar, N. G., & Baydar, H. A. S. A. N. (2004). Note: Antioxidant and antibacterial activities of *Rosa damascena* flower extracts. *Food science and technology international*, 10(4), 277-281.
- Paksoy, A. S. (1999). Paint manual. Ankara: Chamber of Chemical Engineers, 1 281

- Palamutcu, S., Keskin, R., Devrent, N., Şengül, M., & Hasçelik, B. (2009). Functional textiles II: antimicrobial textiles. *Electronic Journal of Textile Technologies*, 3(3), 95-108.
- Prabhu, K.H., & Bhute, A. S. (2012). Plant based natural dyes and mordants: A Review. *J. Nat. Prod. Plant Resour*, 2(6), 649-664.
- Rajvanshi A.K., In: VIth International Safflower Conference (Ed. Esendal E.), Istanbul, Turkey, June 2005, 6-10.
- Saleem, M., & Saeed, M. T. (2020). Potential application of waste fruit peels (orange, yellow lemon and banana) as wide range natural antimicrobial agent. *Journal of King Saud University-Science*, 32(1), 805-810.
- Samanta, A. K., & Agarwal, P. (2009). Application of natural dyes on textiles. Shahidi, F., & Naczki, M. (2003). *Phenolics in food and nutraceuticals*. CRC press.
- Shi, J., & Maguer, M. L. (2000). Lycopene in tomatoes: chemical and physical properties affected by food processing. *Critical reviews in food science and nutrition*, 40(1), 1-42.
- Singh, R., Jain, A., Panwar, S., Gupta, D., & Khare, S. K. (2005). Antimicrobial activity of some natural dyes. *Dyes and pigments*, 66(2), 99-102.
- Siva, R. (2007). Status of natural dyes and dye- yielding plants in India. *Current science*, 916-925.
- Takahashi, Y. Et al. *Tetrahedron Lett.* 23,1982, 51-63. Tavassoli, S., & Djomeh, Z. E. (2011). Total phenols, antioxidant potential and antimicrobial activity of methanol extract of rosemary (*Rosmarinus officinalis* L.). *Global Veterinaria*, 7(4), 337-341.
- Thiry, M. C. (2001). Antimicrobials take the field. *AATCC Rev.*, 11, 11-175. Natural Dyeing, 2007. T.R. Ministry of Culture and Tourism, Ankara.
- Yang, S. A., Jeon, S. K., Lee, E. J., Shim, C. H., & Lee, I. S. (2010). Comparative study of the chemical composition and antioxidant activity of six essential oils and their components. *Natural Product Research*, 24(2), 140-151.
- Yanishlieva, N. V., & Marinova, E. M. (2001). Stabilisation of edible oils with natural antioxidants. *European journal of lipid science and technology*, 103(11), 752-767.
- <https://www.turkchem.net/filling-of-pigments-dye-and-of-plastic-impact-and-social.html>

<http://www.nanopolchemical.com/pigment-ne>



**CHAPTER 2**  
**SPECTROSCOPIC TEST TYPES USED IN ANTIOXIDANT  
CAPACITY DETERMINATION**

Dr. Dilara ÜLGER ÖZBEK<sup>1</sup>

---

<sup>1</sup>Advanced Technology Research and Application Centre, Sivas Cumhuriyet University, Sivas, Turkey. ORCID ID: 0000-0002-6834-020X, e-mail: dilaraulger@cumhuriyet.edu.tr



## **INTRODUCTION**

These days, antioxidants are an essential component of our life. Before free radicals, also known as "Reactive Oxygen Species" (ROS), may harm cells, antioxidants aid in their neutralization or destruction. This chapter offers an understanding of the several kinds of damaging free radicals generated during metabolic processes, along with an overview of the *in vitro* assays that are utilized to assess the antioxidant potential of dietary supplements and plant metabolites. Many illnesses are caused by imbalances in the oxidant-antioxidant balance. As a result, using antioxidants, whether natural or synthetic, benefits human health. Test procedures that gauge these supplements' antioxidant capability are crucial in this regard.

### **1.FREE RADICALS**

Radicals are chemical formations with unshared electrons in their outer orbitals. A chemical species might be as simple as an atom or as complex as an organic molecule. Radicals are chemical species with extremely high reactivity due to the existence of unshared electrons in the outer orbitals, which greatly increases the reactivity of the substance in question. Because of different physical and chemical reasons, radicals are constantly produced in the world we live in. Radicals are created by three fundamental methods, regardless of where or how they are produced. These arise as a result of processes such as homolytic covalent bond breaking, electron loss from a normal molecule, and electron transfer to a normal molecule (Kilinc & Kilinc, 2002). Under cellular circumstances, a substantial volume and diversity of free radicals are created.

The most significant free radicals in biological systems are oxygen and nitrogen radicals (Aruoma, 1998). Reactive nitrogen and oxygen species (RNS-ROS) serve two functions in the organism's system: they are both harmful and useful. Lower doses have favorable benefits and participate in several physiological processes such as redox control, mitogenic responses, cellular signaling pathways, and immunological function, but greater quantities cause nitrosative and oxidative stress (Phaniendra, Jestadi, & Periyasamy, 2015). The generation of highly reactive ROS is an important feature of the normal cellular system such as fertilization, ovulation, arachidonic acid metabolism, phagocytosis, and mitochondrial respiratory chain (Snezhkina et al., 2019). Nitric oxide, alkoxy, peroxy, hydroxyl, hydrogen peroxide, and superoxide are examples of reactive species.

Superoxide radicals are primarily produced by microsomal and mitochondrial electron transport systems. Except for cytochrome oxidase, which retains the reduced form of oxygen intermediates at their active site to protect the cell from oxidative damage. All other elements of the respiratory chain of mitochondria transfer electrons directly to oxygen and do not retain any reduced intermediate of oxygen at their active site. The auto-oxidation of semiquinones on the inner membrane of mitochondria may yield superoxide anions. Dismutation of superoxide anions produced by mitochondria is a significant process. The free radicals alkoxyl and hydroxyl are reactive and immediately target the main macromolecules in cells (Strzelak, Ratajczak, Adamiec, & Feleszko, 2018). ROS-produced free radicals cause undesired changes such as lipid peroxidation, DNA fragmentation, cell death, DNA damage, protein alteration, and membrane degradation (Stephenson, Nathoo, Mahjoub, Dunn, & Yong, 2014).

## **2.ANTIOXIDANTS**

Antioxidants are chemicals that protect cells from harm by either blocking the creation of free radicals or scavenging existing radicals. They often contain a phenolic function in their chemical composition (Kähkönen et al., 1999). These chemical molecules, which operate as barriers in the body, have the property of neutralizing free radicals by giving their own electrons while not becoming free radicals themselves (Prior & Cao, 2000). The chemical structures, solubility, structure/activity connections, and accessibility from natural sources are the most essential variables determining antioxidants' significance in human health (Kaur & Kapoor, 2002). Antioxidant molecules occur naturally in tissues and control various oxidation processes. Furthermore, a decrease in the endogenous production of antioxidant molecules or some components of antioxidant defense systems might result in a variety of disorders (Cutler & Pryor, 1984).

Under normal physiological circumstances, antioxidant defense mechanisms protect cells from oxidative damage produced by substances such as free radical radicals and peroxides. Antioxidant defense mechanisms are classified into two types: enzymatic and non-enzymatic (Rice-Evans, Miller, & Paganga, 1997).

The first of them are enzymatic antioxidants can lower the quantity of reactive species in the biological system by inhibiting the expression or activity of free radical-generating enzymes such as, xanthine oxidase (XO)

and nicotinamide adenine dinucleotide phosphate oxidase (NADPH oxidase). Alternatively, antioxidants boost the production and activity of antioxidant enzymes such glutathione peroxidase (GPx), catalase (CAT), glutathione reductase (GR), glutathione-S-transferase (GST) and superoxide dismutase (SOD) (Aziz, Diab, & Mohammed, 2019).

Non-enzymatic antioxidants are the second type of antioxidant. Vitamin C, vitamin E, polyphenolic chemicals, and carotenoids are all natural. Butylated hydroxyanisole (BHA), butylated hydroxytoluene (BHT), gallic acid, tertiary butylhydroquinone (TBHQ), and nordihydroguaretic acid (NDGA) are examples of synthetic ones (Rice-Evans et al., 1997).

To limit or avoid free radical-directed oxidative damage, the human body has evolved an antioxidant defense system that includes free radical scavenging, metal chelation, and enzymatic activity to eliminate reactive species as soon as they occur. Furthermore, consuming dietary antioxidants can help to maintain a sufficient quantity of antioxidants in the organism's body (Lobo, Patil, Phatak, & Chandra, 2010).

### **3. ANTIOXIDANT CAPACITY DETERMINATION TESTS**

The public's, health professionals, and food researchers increased interest in antioxidants is due to their protective activity in consumed foods against oxidative degradation and in the body of the organism against oxidative stress-directed aberrant processes. These powerful antioxidants from nature are in high demand as pharmaceutical/nutritional ingredients and food preservatives (Shahidi & Zhong, 2015). To effectively seek for novel sources of naturally occurring antioxidants and formulate new antioxidant molecules, dependable methods for assessing antioxidant activity are required. Various biological examples, food models, and chemical tests have been created to quantify the reducing strength, elimination of radicals activity, and other relevant qualities in increasingly complicated biological systems and food items, as well as total oxidation inhibition (Chaudhary & Janmeda, 2022).

As of now, several techniques for measuring antioxidant capacity have been identified (Albayrak, Sagdıç, & Aksoy, 2010). While antioxidant activity (AOA) is assessed in proportion to the reaction kinetics rate in these approaches, antioxidant capacity (AOC) may be determined using reaction thermodynamics. Various sources classify these procedures as *in vitro* and *in vivo*, enzymatic and non-enzymatic, or direct and indirect. Furthermore, the most frequently recognized categorization techniques are those based on

hydrogen atom transfer (HAT) and electron transfer (ET) (Özyürek, Güçlü, & Apak, 2011). Many of the HAT-based methodologies are selective reactions based on competing for peroxy radicals produced by the breakdown of azo compounds between antioxidant and substrate. ET techniques are color change-based methods for determining an antioxidant's oxidant-reducing activity (Albayrak et al., 2010). In general, HAT reactions occur in a relatively short period and are somewhat independent of solvent and pH changes. ET reactions, on the other hand, are solvent and pH dependent and take longer to complete (Apak et al., 2007).

### **3.1. Reactions involving hydrogen transfer (HAT)**

On the basis of HAT analyzes assess an antioxidant's capacity for neutralizing free radicals (often peroxy radicals) by H-atom donation. In HAT-based antioxidant studies, the antioxidant capacity may be determined from the competitive kinetics since both the antioxidants and the fluorescent probe react with ROO. By calculating the area under these graphs and assessing the probe's fluorescence decay curve in the presence and absence of antioxidants (Huang, Ou, & Prior, 2005). HAT-based tests include the oxygen radical absorbance capacity (ORAC) test, total radical scavenging antioxidant parameter (TRAP) test,  $\beta$ -carotene bleaching test, and crocin bleaching test.

#### **3.1.1. Oxygen radical absorbance capacity (ORAC) test**

ORAC quantifies the reduction of peroxy radicals by antioxidants. Using this technique, a fluorescent molecule (probe) and a peroxy radical combine to generate a non-fluorescent result (Glazer, 1990). Using the integrated net area under the fluorescence decay curve, the protective effect of the antioxidant is calculated. Therefore, by tracking the target molecule's breakdown using fluorescence monitoring, one may ascertain the degree to which an antioxidant protects an oxidized target molecule caused by peroxy radicals (Prior, Wu, & Schaich, 2005).

The usual procedure uses a bis azide initiator, 2,2'-azobis-2-methylpropanimidamide dihydrochloride (AAPH), to break down fluorescein fluorescence over time as a result of peroxy-radical production at 37° centigrade. Antioxidant activity is measured by the slowing of fluorescence loss in the presence of antioxidants, and the decrease in fluorescence is monitored visually. Fluorescein (3', 6'-dihydroxy-spiro [isobenzofuran-1[3H], 9' [9H]-xanthen]-3-one) may be oxidized by the peroxy radical to produce a compound devoid of fluorescence. Through a hydrogen atom transfer

mechanism, antioxidants stifle this process and prevent the fluorescein signal from degrading oxidatively. Thirty minutes are used to measure the fluorescence signal, with the cutoff at 530 nm, emission at 538 nm, and excitation at 485 nm. Test örneğindeki antioksidan konsantrasyonu, testin seyri boyunca floresans yoğunluğuyla orantılıdır ve eğri altındaki net alanın bilinen bir antioksidan olan troloks ile karşılaştırılması yoluyla değerlendirilir (Gupta, 2015).

### **3.1.2. Total radical scavenging antioxidant parameter (TRAP) Test**

The basis of this technique is the measurement of oxygen consumption during a regulated reaction of lipid peroxidation brought on by the thermal breakdown of an azo molecule (Ali et al., 2008). The fluorescence probe in this technique is R-phycoerythrin (R-PE). Fluorometric monitoring of the reaction progress of R-PE with AAPH is done using  $\lambda_{ex}=495$  nm and  $\lambda_{em}=575$  nm. R-PR, which was initially separated from the red algae *Gracilaria*, is the brightest fluorescent dye ever discovered. The duration of the lag phase brought on by the antioxidant in comparison to Trolox's is used to compute TRAP values. Additionally, luminol can be employed as a chemiluminescent material (Pisoschi & Negulescu, 2011).

### **3.1.3. Crocin Bleaching Test**

Naturally developing, crocin is a carotenoid derived from the dried stigma of the culinary spice *Crocus sativus L.*, often known as saffron (Bors, Michel, & Saran, 1984). The colorimetric technique known as the crocin bleaching method is used to examine both individual components and complicated structures (Albayrak et al., 2010). By comparing with parallel reactions, this seldom used approach determines the extent of peroxy radical bleaching caused by crocin during the thermal breakdown of diazo compounds. By adjusting the solvent, this technique may be used on both lipophilic and hydrophilic components. The antioxidant capacity is then determined in relation to Trolox C or  $\alpha$ -tocopherol (Bortolomeazzi, Sebastianutto, Toniolo, & Pizzariello, 2007).

### **3.1.4. $\beta$ -carotene bleaching test**

The antioxidant capacity of non-polar antioxidants and essential oils may be estimated using this approach. The basis of the  $\beta$ -carotene bleaching process is the fact that  $\beta$ -carotene loses its yellow color when it reacts with

radicals created in an emulsion by linolenic acid oxidation (peroxyl radicals). Antioxidants can stop the rate of  $\beta$ -carotene bleaching by giving a hydrogen atom to squelch the free radical, which leads to the creation of lipid derivatives and antioxidant radicals. When it comes to peroxyl radicals, the antioxidants compete with  $\beta$ -carotene (Velioglu, Mazza, Gao, & Oomah, 1998).

### **3.2. Methods based on electron transfer (ET)**

In a reaction mixture, spectrophotometric ET-based approaches comprise two components: antioxidant and oxidant. The oxidant obtains an electron from the antioxidant, causing the oxidant's color to shift. The degree of color change is related to the concentration of antioxidants (Huang et al., 2005).

The amount of antioxidants present in the sample is connected with the degree of color change, which can be either an increase or reduction in absorbance at a certain wavelength. The decolorization assays 2,2-diphenyl-1-picrylhydrazyl (DPPH) and Trolox equivalent antioxidant capacity (ABTS/TEAC) are conducted, while the Folin total phenols assay, ferric reducing antioxidant power (FRAP) and cupric reducing antioxidant capacity (CUPRAC) exhibit an increase in absorbance at a predetermined wavelength due to the antioxidant's reaction with the chromogenic reagent methods. In these assays, the lower valencies of iron and copper, Fe(II) and Cu(I), respectively, form charge-transfer complexes with the ligands (Apak et al., 2007).

#### **3.2.1. DPPH radical scavenging capacity test**

The fact that delocalization on aromatic rings stabilizes DPPH (2,2-diphenyl-1-picrylhydrazyl) makes it a stable radical. While DPPH does not dimerize, it is easily able to capture other radicals. The DPPH radical solution takes on a deep violet hue due to the presence of a strong absorption band that is centered at around 515 nm. When the radical reacts with a hydrogen donor, it becomes light yellow or colorless. The concentration of antioxidants has a linear relationship with the absorbance reduction. The standard antioxidant utilized is trolox (Abuin, Lissi, Ortiz, & Henriquez, 2002). This technique is considered to be easy to use, quick, and appropriate for monitoring the radical scavenging activity of several samples by resolving disparate samples. However, because of its sensitivity to light, oxygen, and pollution results in certain application restrictions (Moț, Silaghi-Dumitrescu, & Sârbu, 2011).



### **3.2.2. Trolox equivalent antioxidant capacity (TEAC/ABTS) test**

The TEAC technique measures a reduction in the 2, 2'-azino-bis (3-ethylbenzthiazoline-6-sulphonic acid (ABTS) radical's absorbance in solution when antioxidants are present. ABTS, which produces a bluish-green radical cation when it reacts with sodium, potassium persulfate, or  $MnO_2$ . The peaks of the ABTS radical cation's distinctive absorption spectra are located at 660, 734, and 820 nm (Re et al., 1999). ABTS, which is generated as a radical cation, is used in conjunction with basic spectrophotometry to quantify the overall antioxidant activity of different compounds (Ali et al., 2008).

### **3.2.3. Copper ion reducing antioxidant capacity (CUPRAC) test**

The copper (II) neocuproine chemical serves as the chromogenic oxidizing factor in the copper ion reducing antioxidant capacity experiment. The CUPRAC test technique outlines the creation of an easy-to-use and broadly applicable assay for measuring the antioxidant capacity of flavonoids, phenolic acids, thiols, hydroxycinnamic acids, synthetic antioxidants, and vitamins C and E (Apak et al., 2013).

### **3.2.4. Total phenolic substance determination**

Since numerous non-phenolic substances can diminish Folin-Ciocalteu reagent (FCR), it is not unique to phenolic compounds. In actuality, the FC technique gauges a sample's potential to reduce. FCR and phenolic chemicals only react in certain basic conditions. A phenolate anion, which may reduce FCR, is created when a phenolic proton dissociates. The structure of the phenolic compounds has no bearing on the blue chemicals that are created when phenolate and FCR combine. Spectrophotometric measurement of blue-colored complex formation occurs at 765 nm. Results are given in gallic acid equivalents (mg/L), with gallic acid frequently serving as the benchmark (Büyüktuncel, 2013).

### **3.2.5. Iron ion reducing antioxidant power test (FRAP)**

The ferric reducing antioxidant power (FRAP) test is used to quantify total antioxidant activity. The FRAP test employs an easily reduced oxidant system that is present in stoichiometric excess and employs antioxidants as reductant in a redox-linked colorimetric technique. A shift in absorbance at 593 nm can be used to track the reduction of ferric tripyridyl triazine complex to ferrous form at low pH (3.6) (Benzie & Strain, 1999).

## **CONCLUSION**

Research indicates that the greatest harm that industrialization and the swift advancement of technology have done to humanity is the detrimental impact that new goods and habits have on health. Significant problems may arise from altering the oxidant-antioxidant balance inside a live organism. Antioxidant-rich diets and dietary supplements are crucial in guarding against these deficiencies in this regard. This section discusses the several sorts of tests that are performed to examine antioxidant species that are vital to life. Two distinct sets of antioxidant capacity approaches are analyzed using different test procedures. A general description of the examinations was provided. Significant problems may arise from altering the oxidant-antioxidant balance inside a live organism. Antioxidant-rich diets and dietary supplements are crucial in guarding against these deficiencies in this regard.

## REFERENCES

- Abuin, E., Lissi, E., Ortiz, P., & Henriquez, C. (2002). Uric acid reaction with DPPH radicals at the micellar interface. *Boletín de la Sociedad Chilena de Química*, 47(2), 145-149.
- Albayrak, S., Sagdıç, O., & Aksoy, A. (2010). Bitkisel ürünlerin ve gıdaların antioksidan kapasitelerinin belirlenmesinde kullanılan yöntemler. *Erciyes Üniversitesi Fen Bilimleri Enstitüsü Fen Bilimleri Dergisi*, 26(4), 401-409.
- Ali, S. S., Kasoju, N., Luthra, A., Singh, A., Sharanabasava, H., Sahu, A., & Bora, U. (2008). Indian medicinal herbs as sources of antioxidants. *Food research international*, 41(1), 1-15.
- Apak, R., Gorinstein, S., Böhm, V., Schaich, K. M., Özyürek, M., & Güçlü, K. (2013). Methods of measurement and evaluation of natural antioxidant capacity/activity (IUPAC Technical Report). *Pure and Applied Chemistry*, 85(5), 957-998.
- Apak, R., Güçlü, K., Demirata, B., Özyürek, M., Çelik, S. E., Bektaşoğlu, B., . . . Özyurt, D. (2007). Comparative evaluation of various total antioxidant capacity assays applied to phenolic compounds with the CUPRAC assay. *Molecules*, 12(7), 1496-1547.
- Aruoma, O. I. (1998). Free radicals, oxidative stress, and antioxidants in human health and disease. *Journal of the American oil chemists' society*, 75(2), 199-212.
- Aziz, M. A., Diab, A. S., & Mohammed, A. A. (2019). Antioxidant categories and mode of action. *Antioxidants*, 2019, 3-22.
- Benzie, I. F., & Strain, J. (1999). [2] Ferric reducing/antioxidant power assay: direct measure of total antioxidant activity of biological fluids and modified version for simultaneous measurement of total antioxidant power and ascorbic acid concentration. In *Methods in enzymology* (Vol. 299, pp. 15-27): Elsevier.
- Bors, W., Michel, C., & Saran, M. (1984). Inhibition of the bleaching of the carotenoid crocin a rapid test for quantifying antioxidant activity. *Biochimica et Biophysica Acta (BBA)-Lipids and Lipid Metabolism*, 796(3), 312-319.
- Bortolomeazzi, R., Sebastianutto, N., Toniolo, R., & Pizzariello, A. (2007). Comparative evaluation of the antioxidant capacity of smoke flavouring phenols by crocin bleaching inhibition, DPPH radical scavenging and oxidation potential. *Food Chemistry*, 100(4), 1481-1489.

- Büyüktuncel, E. (2013). Toplam fenolik içerik ve antioksidan kapasite tayininde kullanılan başlıca spektrofotometrik yöntemler. *Marmara Pharmaceutical Journal*, 17(2), 93-103.
- Chaudhary, P., & Janmeda, P. (2022). Quantification of phytochemicals and in vitro antioxidant activities from various parts of *Euphorbia neriifolia* Linn. *Journal of Applied Biology and Biotechnology*, 10(2), 133-145.
- Cuttler, R., & Pryor, W. (1984). In free radical in biology. *Free Radicals in Biology*, 6, 371-423.
- Glazer, A. N. (1990). [14] Phycoerythrin fluorescence-based assay for reactive oxygen species. In *Methods in enzymology* (Vol. 186, pp. 161-168): Elsevier.
- Gupta, D. (2015). Methods for determination of antioxidant capacity: A review. *International Journal of Pharmaceutical Sciences and Research*, 6(2), 546.
- Huang, D., Ou, B., & Prior, R. L. (2005). The chemistry behind antioxidant capacity assays. *Journal of agricultural and food chemistry*, 53(6), 1841-1856.
- Kähkönen, M. P., Hopia, A. I., Vuorela, H. J., Rauha, J.-P., Pihlaja, K., Kujala, T. S., & Heinonen, M. (1999). Antioxidant activity of plant extracts containing phenolic compounds. *Journal of agricultural and food chemistry*, 47(10), 3954-3962.
- Kaur, C., & Kapoor, H. C. (2002). Anti-oxidant activity and total phenolic content of some Asian vegetables. *International Journal of Food Science & Technology*, 37(2), 153-161.
- Kilinc, K., & Kilinc, A. (2002). Oksijenin Toksisitesinin Aracı Molekülleri Olarak Oksijen Radikalleri. *Hacettepe Tıp Dergisi*, 33(2), 100-118.
- Lobo, V., Patil, A., Phatak, A., & Chandra, N. (2010). Free radicals, antioxidants and functional foods: Impact on human health. *Pharmacognosy reviews*, 4(8), 118.
- Moş, A. C., Silaghi-Dumitrescu, R., & Sârbu, C. (2011). Rapid and effective evaluation of the antioxidant capacity of propolis extracts using DPPH bleaching kinetic profiles, FT-IR and UV-vis spectroscopic data. *Journal of Food Composition and Analysis*, 24(4-5), 516-522.
- Özyürek, M., Güçlü, K., & Apak, R. (2011). The main and modified CUPRAC methods of antioxidant measurement. *TrAC Trends in Analytical Chemistry*, 30(4), 652-664.

- Phaniendra, A., Jestadi, D. B., & Periyasamy, L. (2015). Free radicals: properties, sources, targets, and their implication in various diseases. *Indian journal of clinical biochemistry*, 30, 11-26.
- Pisoschi, A. M., & Negulescu, G. P. (2011). Methods for total antioxidant activity determination: a review. *Biochem Anal Biochem*, 1(1), 106.
- Prior, R. L., & Cao, G. (2000). Analysis of botanicals and dietary supplements for antioxidant capacity: a review. *Journal of AOAC International*, 83(4), 950-956.
- Prior, R. L., Wu, X., & Schaich, K. (2005). Standardized methods for the determination of antioxidant capacity and phenolics in foods and dietary supplements. *Journal of agricultural and food chemistry*, 53(10), 4290-4302.
- Re, R., Pellegrini, N., Proteggente, A., Pannala, A., Yang, M., & Rice-Evans, C. (1999). Antioxidant activity applying an improved ABTS radical cation decolorization assay. *Free radical biology and medicine*, 26(9-10), 1231-1237.
- Rice-Evans, C., Miller, N., & Paganga, G. (1997). Antioxidant properties of phenolic compounds. *Trends in plant science*, 2(4), 152-159.
- Shahidi, F., & Zhong, Y. (2015). Measurement of antioxidant activity. *Journal of functional foods*, 18, 757-781.
- Snezhkina, A. V., Kudryavtseva, A. V., Kardymon, O. L., Savvateeva, M. V., Melnikova, N. V., Krasnov, G. S., & Dmitriev, A. A. (2019). ROS generation and antioxidant defense systems in normal and malignant cells. *Oxidative medicine and cellular longevity*, 2019.
- Stephenson, E., Nathoo, N., Mahjoub, Y., Dunn, J. F., & Yong, V. W. (2014). Iron in multiple sclerosis: roles in neurodegeneration and repair. *Nature Reviews Neurology*, 10(8), 459-468.
- Strzelak, A., Ratajczak, A., Adamiec, A., & Feleszko, W. (2018). Tobacco smoke induces and alters immune responses in the lung triggering inflammation, allergy, asthma and other lung diseases: a mechanistic review. *International journal of environmental research and public health*, 15(5), 1033.
- Velioglu, Y., Mazza, G., Gao, L., & Oomah, B. (1998). Antioxidant activity and total phenolics in selected fruits, vegetables, and grain products. *Journal of agricultural and food chemistry*, 46(10), 4113-4117.



**CHAPTER 3**  
**THE PLACE OF ADDITIVE MANUFACTURING IN DENTAL**  
**PROSTHESES**

Prosthodontist, Dt. Betül KARAHASAN, DDS<sup>1</sup>  
Prof. Dr. Derya ÖZDEMİR DOĞAN, DDS, PhD<sup>2</sup>

---

<sup>1</sup>Cumhuriyet University, Faculty of Dentistry, Sivas, Türkiye. ygtbetl@gmail.com, Orcid ID: 0000-0003-1878-7561

<sup>2</sup>Cumhuriyet University, Faculty of Dentistry, Sivas, Türkiye. dtderya@hotmail.com  
Orcid ID: 0000-0003-2470-9930





## INTRODUCTION

### Computer Aided Production Methods

The impact of rapidly developing technology in our age is great in the dentistry sector, as in other sectors. With computer systems, the design and production of dental restorations can be carried out in a much shorter time.

The 3D design of the restoration to be produced is made using Computer Aided Design (CAD - Computer Aided Design) and Computer Aided Manufacturing (CAM - Computer Aided Manufacturing) systems, and the design can be produced with computer systems. (Jedynakiewicz & Martin, 2001)

CAD/CAM systems have been used for industrial production since 1950. This technology entered the dental sector in 1970, and the first CAD/CAM systems that could take digital measurements were launched by Francois Duret under the name "Sopha Bioconcept". (Liu & Essig, 2008)

After the first system, which was costly and very complicated to use, Werner Mörmann and Marco Brandesti, who further developed this system, presented the first scientifically accepted and usable CAD/CAM system to the dental industry under the name "Cerec". (Mörmann, 2006)

Today, CAD/CAM technology is used in the production of many restorations and materials, including fixed prostheses, implant abutments, removable partial denture frames, complete dentures, surgical stents and maxillofacial prostheses. (Ucar et al., 2009)

CAD/CAM systems consist of 3 basic parts;

- 1. Three-dimensional surface scanner:** It enables the transfer of image data scanned from inside the mouth or from the model to the computer system.
- 2. The software system in which the design is made:** It is the software system that enables the design for the restoration to be produced by processing the data received from the scanner.
- 3. Hardware system where the design is produced:** It is the unit where the restoration is produced in line with the processed data, the design and the selected material. (Beuer et al., 2008; Ucar et al., 2009)

### **Advantages of using CAD/CAM system;**

- No need for traditional impression taking by using an intraoral scanner
- Faster production of restorations
- Less potential for error during production
- Producing restorations more harmoniously
- Ability to control parameters
- Better quality use of production materials
- Saving labor and time by eliminating multi-stage and technical precision-requiring processes such as casting (Mehl et al., 2013; Miyazaki et al., 2009)

### **Disadvantages of using CAD/CAM system;**

- Owning the system requires serious financial investment
- Üretimin geleneksel yöntemlere göre oldukça maliyetli olması
- Inability to fully transfer the information of the teeth to be restored to the computer system because of the scanner's insufficient data acquisition in inappropriate intraoral conditions.
- Requirement of trained experts to use the system (Çetindağ et al., 2016; Christensen, 2001)

### **Production in CAD/CAM systems is carried out by two basic methods;**

1. Subtractive Manufacturing Method
2. Adding Additive Manufacturing Methods

#### **1. Subtractive Manufacturing Method**

In this method, restorations; Production is carried out by abrading blocks produced for dental use such as metal, zirconium, polymethylmethacrylate and ceramics with diamond burs or discs on a computer-aided numerical control device. (Beuer et al., 2008; Uzun, 2008)

It is possible to produce restorations with complex structures, which are difficult to obtain with traditional methods, with much more precision and in a shorter time with the milling system. (Van Noort, 2012)

With the scraping process, after the production of the restorations is completed, the remaining unusable block parts are wasted, which creates a great disadvantage by increasing the production cost. (Witkowski, 2005)

## **2. Additive Manufacturing Methods**

Industry 4.0, the last stage of the industrial revolution, combines information technologies and production systems. Additive manufacturing is a crucial component of these developments.

Additive manufacturing, also known as 3D printing; It is a method of combining raw materials by creating layer upon layer to produce parts in line with the data of the 3D model. Allows parts with high design complexity to be created precisely and quickly. (Dilberoglu et al., 2017)

Additive manufacturing methods are classified and named according to the ISO/ASTM 52900 standard published by the joint work of the International Organization for Standardization (ISO) and the American Society for Testing and Materials (ASTM)

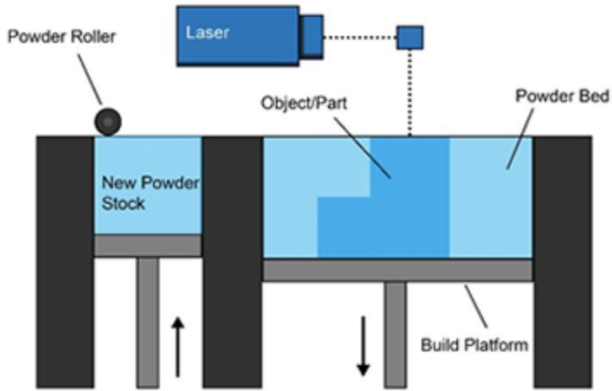
### **Additive Manufacturing Methods**

1. Powder Bed Fusion
2. Material Extrusion
3. Vat Photopolymerization
4. Material Jetting
5. Sheet Lamination
6. Direct Energy Deposition
7. Binder Jetting (ISO/ASTM 52900:2021, n.d.)

### **Powder Bed Fusion**

In this additive manufacturing method, powder particles are partially or completely melted and fused in selected areas in the powder bed laid on the table by a thermal power source using a laser or electron beam. The process of laying a powder layer by a roller is repeated in each layer of production. (Lee et al., 2017)

The powder bed melting process includes Selective Laser Melting (SLM), Selective Laser Sintering (SLS) and Electron Beam Melting (EBM) techniques. The basic bonding mechanisms of these processes are sintering and melting. In the sintering process; While superficial coalescence occurs as a result of the partial melting of powder particles with thermal energy, a complete melting of the powdered material occurs by using higher energy in the melting process. (Lee et al., 2017; C. Y. Yap et al., 2016)



*(Powder Bed Fusion / Additive Manufacturing Research Group / Loughborough University, n.d.)*

### Selective Laser Melting

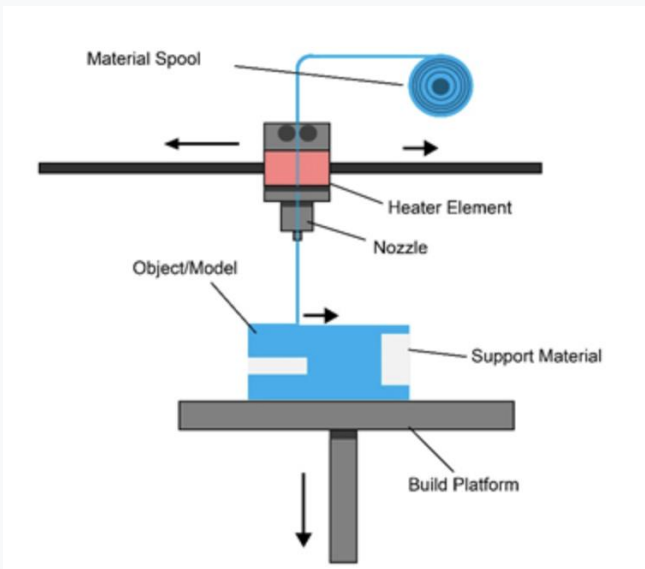
This additive manufacturing method, which provides layer-by-layer production by completely melting the powder layers with high laser energy, is quite popular compared to other additive manufacturing methods. The SLM method has many advantages over other production methods. Compared to the traditional casting method, it can produce very detailed complex parts in detail, the produced parts are almost void-free. It uses raw materials efficiently, and the powders left over from melting can be reused. It can produce materials with superior dimensional accuracy by machining a variety of materials and alloys. Thanks to the high mechanical properties and corrosion and temperature resistance of Co-Cr alloys, parts produced by SLM; It is widely used in many fields such as aviation, orthopedics and dental sector. (Babacan & Seremet, 2022; Wu et al., 2014)

SLM is an additive manufacturing technology that has been widely used in recent years, especially in dental restorations such as personalized crowns, bridges, abutments and screw-retained restorations. SLM can fabricate metal substructure by melting metal powder into nearly porous layers. This technique uses a focused high-power laser beam and results in products with almost 100% density. Laser may also be the key to hardening

metals and ceramics. Additionally, objects with complex geometries can be obtained with high dimensional accuracy. Compared to casting and milling processes, SLM reduces the possibility of operator error, minimizes defects and wastes almost no material as the remaining powder can be used more. (Han et al., 2018)

### Material Extrusion

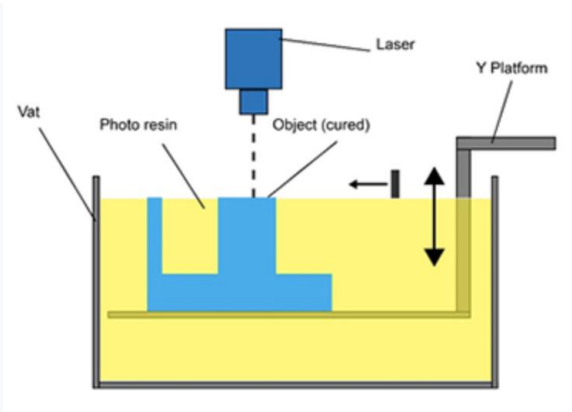
In this method, also known as Melt Deposition Modeling, the filament-shaped material is heated from the nozzle under a constant pressure and removed according to a certain pattern. When placed on the substrate, it completely solidifies and the production of objects is carried out layer by layer. (Lee et al., 2017)



*(Material Extrusion | Additive Manufacturing Research Group | Loughborough University, n.d.)*

### Vat Photopolymerization

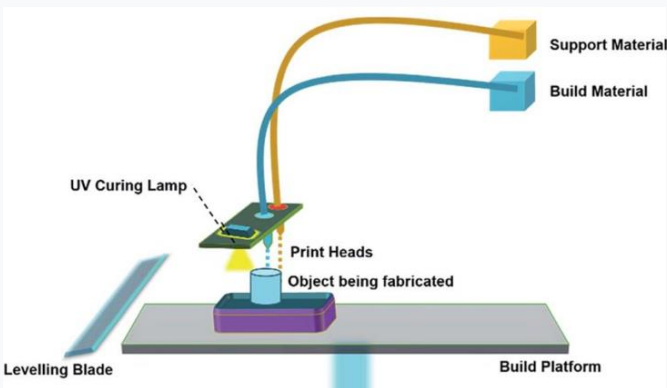
In the pool photopolymerization technique, also known as stereolithography, a tank is filled with ultraviolet light-sensitive resin. With the light focused on the surface, the areas suitable for the design enter into a chemical reaction and solidify in each layer, producing the material. (Gibson et al., 2021; Lee et al., 2017)



(VAT Photopolymerisation | Additive Manufacturing Research Group / Loughborough University, n.d.)

### Material Jetting

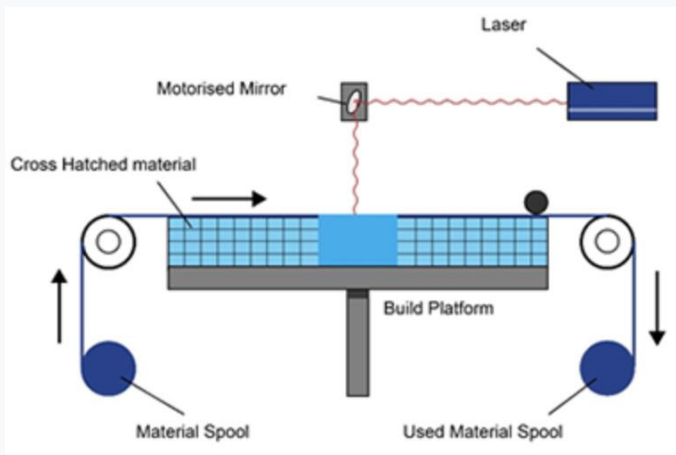
In this method, also called material spraying or ink spraying, different photopolymer droplets in liquid form are deposited into the layers and produced by hardening with ultraviolet lamps. This 3D printer allows the production of parts with different materials on the same object by spraying materials with different mechanical properties from different ends on the same part. (Y. L. Yap et al., 2017)



(Material Jetting | Additive Manufacturing Research Group / Loughborough University, n.d.)

### Sheet Lamination

It is a production technique in which paper, plastic or metal sheets are produced in layers, glued, and the desired shape of the 3D model is cut by a laser source, rather than produced from a material source. It allows the rapid production of large structures, but the objects produced are not durable enough to be a building material, and the cut material pieces cannot be reused and are wasted. (Jadhav & Jadhav, 2022)

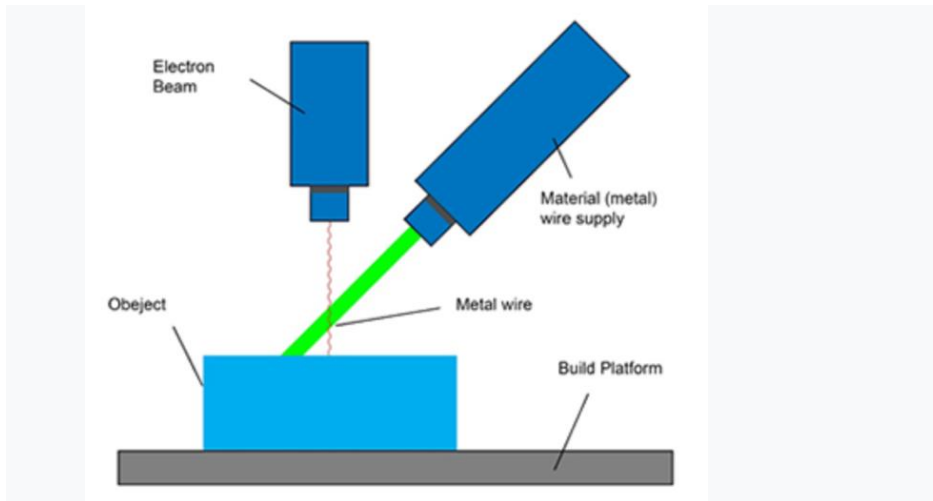


*(Sheet Lamination | Additive Manufacturing Research Group | Loughborough University, n.d.)*

### Direct Energy Deposition

This manufacturing technique uses a powerful laser where energy is focused on a small area to melt metal powders. Production is carried out by dropping the molten material at the end area of the machine to the surface where it solidifies with multi-axis movement capability. (Lee et al., 2017)

Although it produces less resolution than the powder bed assembly process, it can be used to produce larger structures. Using as much material as needed prevents waste and increases efficiency. It is a fast production technique. (Li et al., 2017)



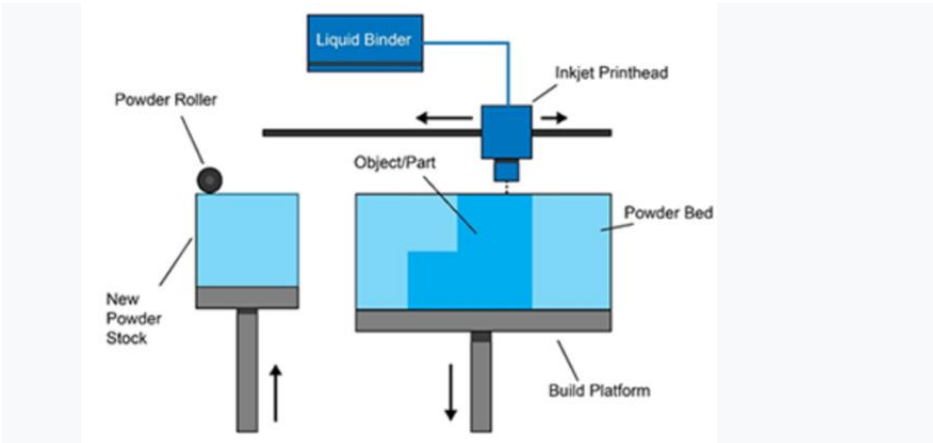
*(Directed Energy Deposition | Additive Manufacturing Research Group | Loughborough University, n.d.)*

### **Binder Jetting**

In this method, also called additive manufacturing with adhesives, production is carried out by selectively bonding the material consisting of powder particles, layer by layer, with a liquid-based binder. The function of the liquid drops is to bind the layers in the powder bed. In each layer, the powder material is laid on the production table with the help of a roller. Printhead deposits connectors into selected areas to produce the design based on CAD data. (Gibson et al., 2021)

The advantages of the binder spraying method include the ability to design without support, produce large materials, fast production and relatively low cost. (Lee et al., 2017)





(Binder Jetting / Additive Manufacturing Research Group / Loughborough University, n.d.)

## REFERENCES

- Babacan, N. & Seremet, H. (2022). INVESTIGATION OF THE LOAD-BEARING CAPACITY OF Co-Cr LATTICE STRUCTURES FABRICATED BY SELECTIVE LASER MELTING. *J. of 3D Printing Tech. Dig. Ind.*, 6(2), 286–291. <https://doi.org/10.46519/ij3dptdi.1139802>
- Beuer, F., Schweiger, J. & Edelhoff, D. (2008). Digital dentistry: an overview of recent developments for CAD/CAM generated restorations. *British Dental Journal*, 204(9), 505–511. <https://doi.org/10.1038/SJ.BDJ.2008.350>
- Binder Jetting | Additive Manufacturing Research Group | Loughborough University*. (n.d.). Retrieved May 25, 2023, from <https://www.lboro.ac.uk/research/amrg/about/the7categoriesofadditivemanufacturing/binderjetting/>
- Çetindağ, M., Toköz, M. & Ayşef, M. (2016). DİŞ HEKİMLİĞİNDE KULLANILAN CAD/CAM (BİLGİSAYAR DESTEKLİ TASARIM/BİLGİSAYAR DESTEKLİ ÜRETİM) SİSTEMLERİ VE MATERYALLER. *Atatürk Üniversitesi Diş Hekimliği Fakültesi Dergisi*, 26(3), 524–533. <https://doi.org/10.17567/ATAUNIDFD.290443>
- Christensen, G. J. (2001). Computerized restorative dentistry. State of the art. *Journal of the American Dental Association (1939)*, 132(9), 1301–1303. <https://doi.org/10.14219/JADA.ARCHIVE.2001.0377>
- Dilberoglu, U. M., Gharehpapagh, B., Yaman, U. & Dolen, M. (2017). The Role of Additive Manufacturing in the Era of Industry 4.0. *Procedia Manufacturing*, 11, 545–554. <https://doi.org/10.1016/J.PROMFG.2017.07.148>
- Directed Energy Deposition | Additive Manufacturing Research Group | Loughborough University*. (n.d.). Retrieved May 25, 2023, from <https://www.lboro.ac.uk/research/amrg/about/the7categoriesofadditivemanufacturing/directedenergydeposition/>
- Gibson, I., Rosen, D., Stucker, B. & Khorasani, M. (2021). Development of Additive Manufacturing Technology. *Additive Manufacturing Technologies*, 23–51. [https://doi.org/10.1007/978-3-030-56127-7\\_2](https://doi.org/10.1007/978-3-030-56127-7_2)
- Han, X., Sawada, T., Schille, C., Schweizer, E., Scheideler, L., Geis-Gerstorfer, J., Rupp, F. & Spintzyk, S. (2018). Comparative Analysis of Mechanical Properties and Metal-Ceramic Bond Strength of Co-Cr Dental Alloy Fabricated by Different Manufacturing Processes.

- Materials* 2018, Vol. 11, Page 1801, 11(10), 1801. <https://doi.org/10.3390/MA11101801>
- ISO/ASTM 52900:2021. (n.d.). *ISO/ASTM 52900:2021(en), Additive manufacturing — General principles — Fundamentals and vocabulary*. Retrieved April 2, 2023, from <https://www.iso.org/obp/ui/#iso:std:iso-astm:52900:ed-2:v1:en>
- Jadhav, A. & Jadhav, V. S. (2022). A review on 3D printing: An additive manufacturing technology. *Materials Today: Proceedings*, 62, 2094–2099. <https://doi.org/10.1016/J.MATPR.2022.02.558>
- Jedynakiewicz, N. M. & Martin, N. (2001). CEREC: science, research, and clinical application. *Compendium of Continuing Education in Dentistry (Jamesburg, N.J. : 1995)*, 22(6 Suppl), 7–13. <https://europepmc.org/article/med/11913288>
- Lee, J. Y., An, J. & Chua, C. K. (2017). Fundamentals and applications of 3D printing for novel materials. In *Applied Materials Today* (Vol. 7, pp. 120–133). Elsevier Ltd. <https://doi.org/10.1016/j.apmt.2017.02.004>
- Li, W., Zhang, J., Zhang, X. & Liou, F. (2017). Effect of optimizing particle size on directed energy deposition of Functionally Graded Material with blown Pre-Mixed Multi-Powder. *Manufacturing Letters*, 13, 39–43. <https://doi.org/10.1016/J.MFGLET.2017.07.001>
- Liu, P. R. & Essig, M. E. (2008). Panorama of dental CAD/CAM restorative systems. *Compendium of Continuing Education in Dentistry (Jamesburg, N.J. : 1995)*, 29(8). <https://pubmed.ncbi.nlm.nih.gov/18935787/>
- Material Extrusion | Additive Manufacturing Research Group | Loughborough University*. (n.d.). Retrieved May 25, 2023, from <https://www.lboro.ac.uk/research/amrg/about/the7categoriesofadditivemanufacturing/materialextrusion/>
- Material Jetting | Additive Manufacturing Research Group | Loughborough University*. (n.d.). Retrieved May 25, 2023, from <https://www.lboro.ac.uk/research/amrg/about/the7categoriesofadditivemanufacturing/materialjetting/>
- Mehl, C., Harder, S., Byrne, A. & Kern, M. (2013). Prosthodontics in digital times: a case report. *Quintessence International (Berlin, Germany : 1985)*, 44(1), 29–36. <https://doi.org/10.3290/J.QI.A28744>
- Miyazaki, T., Hotta, Y., Kunii, J., Kuriyama, S. & Tamaki, Y. (2009). A review of dental CAD/CAM: current status and future perspectives

- from 20 years of experience. *Dental Materials Journal*, 28(1), 44–56. <https://doi.org/10.4012/DMJ.28.44>
- Mörmann, W. H. (2006). The evolution of the CEREC system. *Journal of the American Dental Association*, 137(9 SUPPL.), 7S-13S. <https://doi.org/10.14219/jada.archive.2006.0398>
- Powder Bed Fusion | Additive Manufacturing Research Group | Loughborough University*. (n.d.). Retrieved May 25, 2023, from <https://www.lboro.ac.uk/research/amrg/about/the7categoriesofadditivemanufacturing/powderbedfusion/>
- Sheet Lamination | Additive Manufacturing Research Group | Loughborough University*. (n.d.). Retrieved May 25, 2023, from <https://www.lboro.ac.uk/research/amrg/about/the7categoriesofadditivemanufacturing/sheetlamination/>
- Ucar, Y., Akova, T., Akyil, M. S. & Brantley, W. A. (2009). Internal fit evaluation of crowns prepared using a new dental crown fabrication technique: laser-sintered Co-Cr crowns. *The Journal of Prosthetic Dentistry*, 102(4), 253–259. [https://doi.org/10.1016/S0022-3913\(09\)60165-7](https://doi.org/10.1016/S0022-3913(09)60165-7)
- Uzun, G. (2008). Uzun (2008) An Overview of Dental CAD/CAM Systems. *Biotechnology & Biotechnological Equipment*, 22(1), 530–535. <https://doi.org/10.1080/13102818.2008.10817506>
- Van Noort, R. (2012). The future of dental devices is digital. *Dental Materials: Official Publication of the Academy of Dental Materials*, 28(1), 3–12. <https://doi.org/10.1016/J.DENTAL.2011.10.014>
- VAT Photopolymerisation | Additive Manufacturing Research Group | Loughborough University*. (n.d.). Retrieved May 25, 2023, from <https://www.lboro.ac.uk/research/amrg/about/the7categoriesofadditivemanufacturing/vatphotopolymerisation/>
- Witkowski, S. (2005). (CAD-)/CAM in dental technology. *Quintessence Dent Technol*, 28, 169–184.
- Wu, L., Zhu, H., Gai, X. & Wang, Y. (2014). Evaluation of the mechanical properties and porcelain bond strength of cobalt-chromium dental alloy fabricated by selective laser melting. *The Journal of Prosthetic Dentistry*, 111(1), 51–55. <https://doi.org/10.1016/J.PROSDENT.2013.09.011>
- Yap, C. Y., Chua, C. K. & Dong, Z. L. (2016). An effective analytical model of selective laser melting.

*Http://Dx.Doi.Org/10.1080/17452759.2015.1133217*, 11(1), 21–26.  
<https://doi.org/10.1080/17452759.2015.1133217>

Yap, Y. L., Wang, C., Sing, S. L., Dikshit, V., Yeong, W. Y. & Wei, J. (2017). Material jetting additive manufacturing: An experimental study using designed metrological benchmarks. *Precision Engineering*, 50, 275–285.  
<https://doi.org/10.1016/J.PRECISIONENG.2017.05.015>



## **CHAPTER 4**

### **COMPRASION of CHARACTERISTICS of METALLIC BIOMATERIALS USED in MEDICAL IMPLANTS**

Vildan Fadime DEMİREZEN<sup>1</sup>  
Dr. Öğr. Üyesi Kenan IŞIK<sup>2</sup>

---

<sup>1</sup> Karabük Üniversitesi, Fen Bilimleri Enstitüsü, Biyomedikal Mühendisliği Ana Bilim Dalı, Karabük, Türkiye. vildandemirezen@hotmail.com, Orcid ID: 0000-0002-4640-6861

<sup>2</sup> Karabük Üniversitesi, Mühendislik Fakültesi, Mekanronik Mühendisliği, Karabük, Türkiye. kenanisik@karabuk.edu.tr Orcid ID: 0000-0002-0973-5180





## 1. INTRODUCTION

Due to the convergence of the advancing medical and materials industries in today's world, the development of biomaterials used in the production of medical devices has become inevitable. The biomaterials selected for the production of medical implants, mostly used within the body, can be referred to as natural or synthetic materials that can replace tissues in the human body (Güven,2014). Biomaterials can be employed with the purpose of restoring, supporting, or enhancing damaged tissue, organs, or functions.

For the efficient use of biomaterials, the most crucial factor is the correct selection of materials. In this context, biocompatibility takes precedence among the characteristics to be considered in material selection, and material choices are made by taking biomechanical properties into account as well. A biocompatible material should not leave a toxic effect or trigger any allergic reactions in the body. When examined in terms of mechanical properties, it should bear the body weight according to the area of use, be either lightweight or able to withstand tensile and compressive forces, and be resistant to corrosion (Özkan, Şişik, Öztürk, 2016).

Materials possessing these characteristics can be categorized into four groups:

- Metals
- Ceramics
- Polymers
- Composites

Metallic biomaterials are generally used to replace non-functional hard tissues. They are commonly employed in the treatment of bone fractures, hip and shoulder joints, and dental loss (Gür, Taşkın, 2004).

Ceramic biomaterials are classified as biologically inert, bioactive, or biodegradable based on their interaction with tissues. They find applications in the treatment of bone tissue and dental procedures (Pasinli, 2004)

Polymeric materials such as polyethylene (PE), polyacetal (PA), silicone rubber (SR), polylactic acid (PLA), are used in medical applications. Despite their wide range of applications, their use in certain applications (e.g., orthopedic applications) is limited due to weak mechanical properties or undesirable toxic characteristics (Pasinli, 2004).

Composites, the last group of biomaterials, are formed by combining at least two materials selected to complement the desired properties for the intended application. Compared to pure materials, composites are high-strength materials with structural compatibility, utilizing the strengths of each material to compensate for the weaknesses of the others. This characteristic makes composite materials suitable for use in orthopedics, dentistry, and artificial organs (Özkan et al., 2016).

## 2. METALLIC BIOMATERIALS

Metallic biomaterials are commonly used in medical devices designed to fulfill essential functions in limbs and hard tissues that have typically lost their functionality (Hürmüzlü, Mollaoğlu, 2023). Implants and prosthetics used in the fields of Orthopedics and Traumatology, Neurosurgery, and Dentistry are predominantly made from metallic materials.

Despite their disadvantages, such as low biocompatibility and the possibility of corrosion, metallic biomaterials are preferred in the medical sector due to their strong mechanical properties, including ease of shaping, high compressive and tensile strengths, and resistance to fatigue and wear (Özkan, et al. 2016; Pilliar, 2021).

Metallic implant materials, with the oldest history compared to currently used biomaterials, date back to around 2000 years ago in the context of dental implants. One significant piece of evidence is the discovery of artificial teeth in Egyptian mummies. However, the use of metallic materials in internal body implants began in 1938 with the application of vanadium steel in bone plate and screw systems. After approximately 20 years of use, this material was discontinued when it started corroding, posing a danger to patients (Güven, 2014; Özkan, et al, 2016).

Due to their high functional performance and ease of processing, extensive research has been conducted on metallic biomaterials, leading to the development of the materials currently used today. When examining metallic biomaterials, they can be categorized into four main groups:

- Titanium and Alloys
- Cobalt-Chromium Alloys
- Stainless Steels
- Magnesium Alloys

To determine which of these materials is more suitable and should be chosen, it is necessary to first understand the characteristics of the intended application and then the properties of the materials. Therefore, a detailed examination of material properties is essential.

## **2.1. Titanium and Alloys**

Despite the availability of various materials for medical use, pure titanium and its alloys have become more widely preferred than other metallic biomaterials. Discovered in 1790 by William Gregor in England, it was officially named titanium by Klaproth in 1795. Titanium possesses the necessary biocompatibility and biomechanical properties required for in-body implantation, making it one of the few metals that meet these conditions. This properties has increased its selection rate in the medical sector (Şap, S., Şap, Kırık, 2019).

### **2.1.1 Titanium Alloys and Their Properties**

The properties present in titanium and its alloys contribute to the longevity of implants, making them suitable for products such as partial prostheses, dental implants, prosthetic joints, and fracture treatment sets. Factors that increase their selection include:

- Acceptably low density,
- Minimal presence of harmful substance in the alloys,
- High strength,
- Low modulus of elasticity,
- Long fatigue life (Hürmüzoğlu, et al, 2023).

The low modulus of elasticity and density provide titanium and its alloys with excellent corrosion resistance and mechanical properties similar to bone. A smaller elastic modulus results in less stress shielding, considered a biomechanical advantage. Due to its higher strength compared to other metallic materials, it possesses an elastic modulus closest to human bone.

Another reason for its widespread use is the presence of an oxide layer on its surface. This layer, formed during the passivation process, provides the material with acceptable biocompatibility and corrosion resistance. Additionally, this layer contributes to coating methods applied to titanium. The inert effect of the layer facilitates the covering of the metal surface by body fluids and tissues, a process known as osseointegration.

Through osseointegration, the implanted piece becomes a part of the body, ensuring maximum strength for the implant.

To enhance the mechanical properties of titanium, alloys are created with substances such as aluminum, vanadium, and iron. The International American Testing and Material Society (ASTM) has categorized these alloys into various groups, including:

- F67- Unalloyed Titanium
- F136- Wrought Titanium 6-Aluminum 4-Vanadium ELI Alloy
- F1472- Wrought Titanium 6-Aluminum 4-Vanadium Alloy
- F1713- Wrought Titanium 13-Niobium 13-Zirconium Alloy
- F1813- Wrought Titanium 12-Molybdenum 6-Zirconium 2-Iron Alloy

The first titanium alloy used in applications is Ti6Al4V, developed in the United States in 1954. Due to its higher heat resistance, machinability, and biocompatibility compared to other alloys, it is used 75-85% more frequently.

Titanium alloys are formed by adding balance regulators, known as  $\alpha$  and  $\beta$ , to pure titanium. Alloys are divided into three main groups:  $\alpha$  alloys,  $\beta$  alloys, and  $\alpha+\beta$  alloys (Perihan, 2015).

$\alpha$  alloys, also known as alpha alloys, are created by adding elements such as Al, Sn, Ga, and Zr to titanium as balance regulators (Subaşı, Karataş, 2012). All known alpha alloys exhibit good toughness and yield strength. They maintain their ductility and toughness even at low temperatures. However, they exhibit poor formability. Ti-5Al-2.5Sn can be given as an example of an alpha alloy (Çelik, Kılıçkap,2018).

Beta alloys, formed by adding elements such as V, Mo, Nb, Ta, Cr, tend to have a brittle structure. When compared to other alloy types, they exhibit higher properties in terms of cold working and forgeability. They possess good strength both at high and low temperatures (Perihan,2015; Subaşı et al,2012).

Another alloy class,  $\alpha+\beta$  alloys, results from the combination of pure titanium with elements that enhance the stability of both phases. Ti6Al4V, which is widely used in medical production, is an  $\alpha+\beta$  alloy that combines high strength, ductility, and homogeneity. It possesses properties such as suitable elasticity for bone tissue, stress distribution, and corrosion resistance, which are essential for in-body implants.

While pure titanium is generally preferred in dentistry due to its low mechanical properties, Ti6Al4V is used in high mechanical requirement implants such as joint implants (hips, knees), intramedullary nails, bone plates, and screws in the fields of dentistry and orthopedics. It offers the necessary mechanical properties for these applications (de Viteri, Fuentes,2013).

The density of titanium and its alloys is already low, making it the lowest among metallic biomaterials, aligning well with the density of human bone. This low density helps maintain distribution along the bone structure in the used area, enhancing compatibility with the bone Sarraf, Rezvani, Alipor, Ramakrishna, Liana,2021).

Mechanical compatibility at the site of use requires capturing the right alloy, achieved by combining the correct phases and examining their mechanical properties. In this context, Table-1 provides the mechanical properties of pure titanium and some alloys.

**Table 1.** Mechanical properties of pure titanium and alloys

<b>Mechanical Properties</b>	<b>Pure Ti Grade 1</b>	<b>Pure Ti Grade 2</b>	<b>Ti-6Al-4V</b>	<b>Ti-6Al-7Nb</b>	<b>Ti-5Al-2.5Fe</b>	<b>Ti-13Nb-13Zr</b>
Tensile Strength (MPa)	40	45	60-965	9 00-1050	020	73-1037
Flow Resistance ( $\sigma_y$ )	70	75	95-875	8 80-950	95	36-908
Extension (%)	4	0	0-15	8. 1-15	5	0-16
Cross-Section Narrowing (GPa)	0	0	5-47	2 5-45	5	7-53
Elasticity Module	02.7	02.7	01-110	1 14	12	9-84
Alloy Type			+ $\beta$	$\alpha$ + $\beta$	+ $\beta$	

Besides its mechanical properties, one of the most significant reasons for using a material as a biomaterial is its biocompatibility. When an implant is placed in bone tissue, numerous physical, chemical, and biological factors determine osteointegration. Titanium and its alloys, which provide these factors, are commonly used in fields such as dentistry and orthopedics. Additionally, various coatings are applied to the surface to impart the ability to bind spontaneously to living tissue. These coatings enhance the self-binding property of titanium and alloys with good osteointegration (de Viteri, et al,2013).

As seen in Table-1, pure titanium is alloyed with many elements from the specified alpha and beta phases. By altering the ratios of these phases, numerous titanium alloys with strengthened mechanical and biological properties are obtained and used in the medical sector. Considering all these features, the advantages of titanium and its alloys include:

- High biocompatibility in implantation,
- Minimal likelihood of chemical reactions,
- MRI compatibility,
- Lightweight,
- Mechanical properties similar to bone,
- Presence of an oxide layer,
- Excellent corrosion resistance.

### **Cobalt-Chromium and Alloys**

Cobalt-chromium materials, initially used in medical applications for dental implants through the casting method, find applications in engineering fields that require heat resistance and corrosion resistance. Due to their high corrosion and wear resistance, along with excellent mechanical properties, cobalt-chromium alloys have earned a place among metallic biomaterials (Narushima, Ueda, Alfirano, 2015). Since the 1980s, these alloys have become increasingly popular in the production and use of removable and fixed prosthetics, making them some of the most well-known metal alloys (Çetiner, Tazegül, Erdem, Çimenoglu, 2014). Throughout this journey until the present day, these alloys are predominantly preferred as materials for fixation products in joint endoprostheses (for fractured bones) in addition to their use in prosthetics like knees, hips, and shoulders.

### **2.2.1. Cobalt-Chromium Alloys and Their Properties**

Due to their high wear resistance and mechanical load-bearing properties, cobalt-chromium alloys are one of the metallic materials suitable for use as biomaterials (Aygül, Yalçınkaya, Şahin, s.31) . The chromium element present in cobalt alloys is a material that enhances corrosion resistance. While cobalt provides 65% of corrosion resistance, the addition of chromium further increases corrosion resistance against solid materials (Gür, et al., 2004). Another important material added to cobalt alloy besides chromium is carbon. In the casting process, carbon increases the castability of the alloy, facilitating the machinability of the material (Şap, et al, 2019).

Categorized as base metal alloys that are both mechanically compatible and biocompatible, cobalt-chromium alloys are generally processed through the casting method. Although their initial use started with dental implants, they have expanded their area of use in the body through static and dynamic tests, proving their versatility (Kırkık, Karabulut, Öztürk, Taş, 2019). These alloys possess several properties that make them preferred materials for in-body implantation products, such as:

- High strength,
- Heat resistance,
- Resistance to wear and discoloration,
- Good biocompatibility,
- High elastic modulus (Çetiner, et al. 2015).

Cobalt-chromium alloys with these specified properties are fundamentally classified into two types. One of them is the Co-Cr-Mo alloy, which is created with the addition of molybdenum (Mo) to enhance mechanical properties. This alloy, which has been used in dentistry for a long time, becomes hard and durable due to the similar atomic sizes of the added elements. The main features of the Co-Cr-Mo alloy include brightness, high hardness, and high wear resistance. Typically processed through the casting method, this alloy is frequently used in cases of tooth loss, bridge applications, and artificial joints.

The other alloy is the Co-Cr-Ni-Mo alloy, which is processed by hot rolling. This alloy is used as a prosthetic stem material in areas with heavy loads and in joints. Co-Cr-Ni-Mo alloys have mechanical strength, resistance to corrosion, and low cost among their properties, making them suitable for various applications (Şap, et al. ,2019).

ASTM has classified alloys created by adding nickel and molybdenum into four groups according to biomedical applications. These are:

- ASTM F75 Cobalt-28 Chromium-6 Molybdenum Casting Alloy
- ASTM F90 Wrought Cobalt-Chromium-15T Tungsten-10 Nickel Alloy
- ASTM F562, Wrought Cobalt-35 Nickel-20 Chromium-10 Molybdenum Alloy
- ASTM F563 Wrought Cobalt-Nickel-Chromium-Molybdenum-Tungsten-Iron

The mechanical properties of the a fore mentioned alloys are listed in Table-2.

**Table 2.** Mechanical properties of cobalt-chromium alloys.

Mechanical Properties	CoCrMo	CoCrWNi	CoNiCrMo	
			Tempered	Cold Pounded and Aged
Tensile Strenght (MPa)	55	60	8 93-1000	1 793 (min)
Yield Strenght (MPa)	50	10	3 40-655	1 585
Extension(%)		0	1 0	8
Cross-Section Contraction (%)		---	5.5	3 5
Fatigue Strenght (MPa)	10	---	---	--

When the applications and mechanical properties of cobalt-chromium alloys are examined in biomedical applications, the advantages can be listed as follows:



- **High Hardness:** These alloys exhibit high hardness, enhancing durability and wear resistance.
- **Good Elongation Value:** Cobalt-chromium alloys have a favorable elongation value, providing advantages in terms of malleability and workability.
- **Tensile Strength:** These alloys demonstrate tensile strength and resistance against deformation, contributing to their mechanical robustness.
- **Economic Affordability:** Cobalt-chromium alloys present an economical option, being cost-effective.

These features support the preference for cobalt-chromium alloys in various biomedical applications.

## **2.2. Stainless Steel**

In engineering applications, steels, which are still used as primary metals, have also become preferred materials in biomedical applications. While steel consists primarily of iron and carbon, it may also contain trace amounts of silicon, manganese, sulfur, and phosphorus. Although steel is formed by alloying carbon and iron, the term alloy steel indicates that elements other than carbon are present in the metal. Steels in this group are more expensive and harder to process compared to carbon steel, but they exhibit higher corrosion and heat treatment resistance (Santos,2017). The steels used in implant applications are stainless steels, which are classified based on their microstructures as martensitic, ferritic, austenitic, and duplex. Except for duplex stainless steels, which belong to the duplex class, other stainless steels are used in medical applications.

### **2.3.1. Stainless Steel and Their Properties**

The first biomaterial manufactured as stainless steel is the 18/8 Cr/Ni stainless steel implant. These materials are made from vanadium steel due to their strength and corrosion resistance. However, the corrosion resistance has not been sufficient for long-term use as an implant. Therefore, the corrosion resistance has been improved by increasing the molybdenum content in the alloy. This alloy is known as 316 stainless steel. Later, the carbon content in 316 stainless steel, which is initially 0.08%, was reduced to 0.03% to obtain 316L stainless steel with better corrosion resistance (Mert,

Gürün, Karağaç, Uluer, 2013). The letter "L" is added to indicate the low carbon content.

Although chromium is not an active element, it forms an active and protective chromium oxide layer on the material surfaces. The chromium oxide passive layer formed on the surface enhances the usability of the steel by promoting passivation. Combining mechanical strength and corrosion resistance properties, 316L steel is commonly used in femoral shafts, fracture plates, and hip nails (Cömert, 2005).

The required corrosion resistance for use in biomedical applications is achieved in stainless steels through chromium. The chromium content must be a minimum of 11%.

Among the stainless steels used in medical applications, 316L is preferred more than 316. Stainless steels have a higher modulus of elasticity than titanium alloys, making them more rigid.

Stainless steels used as biomaterials are classified by ASTM as:

- F138 316LVM - Wrought 18 Chromium-14 Nickel-2.5 Molybdenum Stainless Steel
- F139 Wrought 18 Chromium-14 Nickel-2.5 Molybdenum Stainless
- F621 Stainless Steel
- F745 18 Chromium-12.5 Nickel-2.5 Molybdenum Stainless Steel
- F1350 Wrought 18 Chromium-14 Nickel-2.5 Molybdenum Stainless Steel
- F1586 Wrought Nitrogen Strengthened-21 Chromium-10 Nickel-3 Manganese-2.5 Molybdenum Stainless Steel (Santos,2017).

Austenitic stainless steels are the main steels used in implant applications. According to ASTM F139, these are divided into two grades. The carbon content determines these grades, with the second grade having lower carbon content, meaning it has better corrosion resistance (Sezer, Evis, Kayhan, Tahmasebifar, Koç,2018).

The mechanical properties of some stainless steels used in medical applications, based on the quantities of elements present, are listed in Table-3 (Özkan, et al. 2016).

**Table 3.** Mechanical properties of stainless steel.

Mechanical Properties	18Cr-8Ni Stainless Steel (Tempered)	18Cr-8Ni very low carbon Stainless Steel (Tempered)	316 Stainless Steel	
			Tempered	Cold Pounded
Yield Stress (N/m <sup>2</sup> )	2,0-2,3*10 <sup>8</sup>	2,0-2,5*10 <sup>8</sup>	2,4-3,0*10 <sup>8</sup>	7,0-8,0*10 <sup>8</sup>
Tensile Stress (N/m <sup>2</sup> )	5,4-7,0*10 <sup>8</sup>	5,4-6,2*10 <sup>8</sup>	7,0-10,0*10 <sup>8</sup>	10,0*10 <sup>8</sup>
Extension(%)	50-65	55-60	5-55	7-10
Modulus of Elasticity (N/m <sup>2</sup> )	2,0*10 <sup>11</sup>	2,0*10 <sup>11</sup>	2,0*10 <sup>11</sup>	2,0*10 <sup>11</sup>
Fatigue Limit (N/m <sup>2</sup> )	2,3-2,5*10 <sup>8</sup>	--	2,6-2,8*10 <sup>8</sup>	30*10 <sup>8</sup>
Hardness (V.S.)	175-200	170-200	70-200	300-350

Similar to other metallic biomaterials, the material's mechanical properties and biocompatibility should be considered when choosing stainless steels for use. While not suitable for long-term use, the advantages can be listed as follows:

- Low cost
- Easy accessibility
- High rigidity
- Ease of production
- Reasonable biocompatibility

## **2.3. Magnesium Alloys**

Materials such as titanium and its alloys, Co-Cr alloys, and stainless steels are used in medical implants due to their satisfactory characteristics. However, they may exhibit unfavorable characteristics over prolonged usage, such as wear or the release of metal particles. Therefore, researchers have been drawn towards magnesium-based biomaterials to meet the need for a material that possesses similar properties to other metallic alloys and is biodegradable. This requirement has steered them towards magnesium-based biomaterials (Saris, Mervaala, Karppanen, Khawaja, Lewenstam, 2000).

### **2.4.1. Magnesium Alloys and Their Properties**

Discovered by Sir Humphrey in 1808 and utilized as an implant material in clinical applications such as dental wires, expanders, and fractured bone tips by the late 19th century, magnesium is distinct from other biomaterials due to its mechanical and physical compatibility with human bones. Its density and elastic modulus closely match those of bone, and magnesium is a vital metal for metabolism found in the natural structure of bones (Kebabci, 2022).

Magnesium and its alloys, particularly employed as biodegradable materials, are preferred in biomaterial applications due to their high strength compared to other biomaterials and low density. Magnesium alloys are emerging as a promising biomaterial for next-generation implants because of its favorable biological properties, superior mechanical characteristics, and elastic modulus close to bone tissue (Mert, et al. 2013).

In addition to orthopedic implants, magnesium is also used in vascular stents, typically alloyed with other elements rather than in its pure form. Alloyed magnesium exhibits stronger mechanical properties and corrosion resistance compared to its pure form, leading to the selection of alloyed magnesium in clinical studies (Guo, Co, Lu, Liu, Xu, 2011).

The WE43 alloy is the first biodegradable magnesium alloy developed for vascular stents. Other alloys such as AZ31, AZ91, and LAE442 have been studied in clinical trials, and no potential adverse effects on the skin have been observed (Radha, Sreekanth, 2017). However, the primary development focus on non-medical applications of these alloys has brought

about some challenges. For example, the release of Al ions from the AZ91 alloy can lead to phosphate deficiency in the body.

Despite these challenges, the advantages of magnesium and its alloys include:

- Magnesium being an essential element for the body with good biological behavior.
- Higher mechanical properties compared to other biodegradable materials.
- Closer elastic modulus to bone tissue compared to other biomaterials.
- Closer density to bone tissue compared to other biomaterials.

Despite these advantages, the effects of magnesium and its alloys are not yet fully understood, and ongoing research aims to address these uncertainties. While pure magnesium may not provide sufficient mechanical properties, alloys may introduce harmful effects of other elements released into the body.

### 2.4. Comparison of Biometals

Each metallic biomaterial, with its distinct physical, chemical, and biological properties, possesses advantages and shortcomings compared to others. As indicated in Table-4, metallic biomaterials with these specified features should be selected based on the requirements and the intended region of use within the body (Radha, et al 2017).

**Table 4.** Mechanical properties of stainless steel

Materials	Using Area	Advantages	Shortcomings
Titanium and Alloys	<ul style="list-style-type: none"> <li>• Fracture fixation plates</li> <li>• Nails</li> <li>• Screws</li> <li>• Hip stems</li> <li>• Cables</li> <li>• Arthroplasty Products</li> <li>• Dental Implants and Prosthesis Systems</li> </ul>	<ul style="list-style-type: none"> <li>• Excellent corrosion resistance</li> <li>• Light Weight</li> <li>• Biocompatibility</li> <li>• Lightweight</li> <li>• MR compatible</li> </ul>	<ul style="list-style-type: none"> <li>• Poor abrasion resistance</li> <li>• Poor bending ductility</li> <li>• Expensive</li> </ul>
Cobalt-Chromium and Alloys	<ul style="list-style-type: none"> <li>• Total hip replacement</li> <li>• Stem</li> </ul>	<ul style="list-style-type: none"> <li>• Superior corrosion resistance</li> <li>• High strength</li> </ul>	<ul style="list-style-type: none"> <li>• Expensive</li> <li>• Difficult to process</li> </ul>

	<ul style="list-style-type: none"> <li>• Knee and hip joints</li> </ul>	<ul style="list-style-type: none"> <li>• Long-term biocompatibility</li> </ul>	<ul style="list-style-type: none"> <li>• High Modulus</li> <li>• Biological toxicity due to ion release</li> </ul>
Stainless Steel	<ul style="list-style-type: none"> <li>• Bone plaques</li> <li>• Bone screws</li> <li>• Cables</li> </ul>	<ul style="list-style-type: none"> <li>• Easily accessible</li> <li>• Low cost</li> <li>• Acceptable biocompatibility</li> <li>• Acceptable durability</li> <li>• Ease of production</li> </ul>	<ul style="list-style-type: none"> <li>• Poor corrosion resistance</li> <li>• Poor abrasion resistance</li> <li>• Allergic reaction in surrounding tissue</li> </ul>
Magnesium and Alloys	<ul style="list-style-type: none"> <li>• Bone plates and screws</li> <li>• Cardiovascular stents</li> <li>• Sewing and staples</li> </ul>	<ul style="list-style-type: none"> <li>• Biocompatibility</li> <li>• Biodegradable</li> <li>• Similar density as bone</li> </ul>	<ul style="list-style-type: none"> <li>• Hydrogen evolution during decay</li> <li>• Low resistance to corrosion</li> <li>• Oscillations in its alloys</li> </ul>

### 3. CONCLUSION

Metallic biomaterials, which have been used since ancient times, have evolved over the years. Metallic biomaterials used in various fields such as orthopedics, cardiovascular, dentistry, etc., are categorized into titanium and alloys, cobalt-chromium alloys, stainless steels, and magnesium alloys. Although each has its own advantages and shortcomings, titanium and its alloys are currently the most commonly used metallic biomaterials. Despite being expensive, its high biocompatibility and good biomechanical properties make this alloy more prominent compared to others. Additionally, cobalt-chromium and stainless steels also share similar applications with titanium. These two biomaterials, with reasonable levels of biocompatibility and biomechanical properties, are widely used after titanium and its alloys. Another biomaterial, magnesium and its alloys, has unique biodegradability and density properties close to bone, but its effects are not yet fully understood thus limiting its use. When literature is examined, it is evident that research is still ongoing, and there is a need to address the requirement for a biomaterial with properties closest to the human body.

## REFERENCES

- Al Jabbari, Y. S. (2014). Physico-mechanical properties and prosthodontic applications of CoCr dental alloys: a review of the literature. *The journal of advanced prosthodontics*, 6(2), 138-145.
- Aygül, A. G. E., Yalçinkaya, Ö. Ü. S., & Şahin, Y. Biyomedikal Uygulamalarda Kullanılan Co-Cr-W Ve Co-Cr-Mo Metal Alaşımlarının Eklemeli İmalat Yöntemi İle Üretilmesi. *Mühendislik Ve Multidisipliner Yaklaşımlar, [Cobalt-Chromium-And Cobalt-Chromium-Molybdenum Metal Alloys Production Using Additive Manufacturing in Biomedical Applications: Engineering and Multidisciplinary Approaches]* 30.
- Cömert, I. (2005). Biyomalzemelerin Gelişimine Toz Metalurjisinin Etkisi [The Effect of Powder Metallurgy on the Development of Biomaterials].
- Çelik, Y. H., & Kiliçkap, E. (2018). Titanyum Alaşımlarından Ti-6al-4v'nın İşlenmesinde Karşılaşılan Zorluklar: Derleme.[Difficulties Encountered in the Processing of Ti-6al-4v from Titanium Alloys:Review] *Gazi University Journal Of Science Part C: Design And Technology*, 6(1), 163-175.
- Çetiner, D., Tazegül, O., Erdem, A. T. A. R., & Çimenoglu, H. (2014). Biyomedikal Kobalt-Krom Alaşımı Üzerinde Oluşturulan Tio2 Tabakasının Karakterizasyonun Ve Biyoaktivitesinin İncelenmesi. [Investigation of the Characterization and Bioactivity of the Tio2 Layer Formed on a Biomedical Cobalt-Chromium Alloy] *Mühendislik Bilimleri Ve Tasarım Dergisi*, 2(3), 171-174
- de Viteri, V. S., & Fuentes, E. (2013). Titanium And Titanium Alloys As Biomaterials. *Tribology-Fundamentals And Advancements*, 1(5), 154-181
- Guo, M., Cao, L., Lu, P., Liu, Y., & Xu, X. (2011). Anticorrosion And Cytocompatibility Behavior Of MAO/PLLA Modified Magnesium Alloy WE42. *Journal Of Materials Science: Materials In Medicine*, 22, 1735-1740
- Gür, A. K., & Taşkin, M. (2004). Metalik Biyomalzemeler Ve Biyoyum. [Metallic Biomaterials And Biomaterials] *Fırat Üniversitesi Doğu Araştırmaları Dergisi*, 2(2), 106-113.
- Güven, Ş. (2014). Biyoyumluluk Ve Biyomalzemelerin Seçimi [Biocompatibility And Selection of Biomaterials]. *Mühendislik Bilimleri Ve Tasarım Dergisi*, 2(3), 303-311.

- Hürmüzlü, M. K., & Mollaoğlu, N. (2023). Dental İmplant Çeşitleri Ve Biyomateriyaller [Types of Dental Implants And Biomaterials]. *ADO Klinik Bilimler Dergisi*, 12(1), 142-149
- Kebapci, T. N. (2022). Biyoçözünür Magnezyum Alaşımının Farklı Isıtma Hızları Ve İnerit Gaz Ortamlarındaki Oksidasyonunun İncelenmesi [Investigation of the Oxidation of Biodegradable Magnesium Alloys at Different Heating Rates And Inert Gas Environments] (Doctoral Dissertation).
- Kirkik, D., Karabulut, B., Öztürk, K., & Taş, S. K. (2019). Dental Uygulamalarda Kullanılan Biyomalzemeler [Biomaterials Used in Dental Applications]. *Nevşehir Bilim Ve Teknoloji Dergisi*, 8(2), 145-153.
- Mert, F. A. R. U. K., Gürün, H. A. K. A. N., Karaağaç, İ. B. R. A. H. İ. M., & Uluer, O. N. U. R. A. L. P. (2013). Kemik Tedavilerinde Kullanılan Biyobozunur İmplant Malzemeler[Biodegradable Implant Materials Used in Bone Treatments], 1. *Uluslararası Plastik Ve Kauçuk Teknolojileri Sempozyumu Ve Sergisi, Ankara*, 71-77.
- Narushima, T., Ueda, K., & Alfirano. (2015). Co-Cr Alloys As Effective Metallic Biomaterials. *Advances In Metallic Biomaterials: Tissues, Materials And Biological Reactions*, 157-178.
- Özkan, A., Şişik, N., & Öztürk, U. (2016). Kompozit Malzemelerin Ağız, Yüz, Çene Cerrahisinde Kullanımı Ve Malzeme Uygunluklarının Belirlenmesi [The Use of Composite Materials in Oral, Facial, Maxillofacial Surgery and Determination of Material Suitability]. *Düzce Üniversitesi Bilim Ve Teknoloji Dergisi*, 4(1), 227-242.
- Pasinli, A. (2004). Biyomedikal Uygulamalarda Kullanılan Biyomalzemeler [Biomaterials Used in Biomedical Applications]. *Makine Teknolojileri Elektronik Dergisi*, 4(4), 25-34.



- Perihan, O. Y. A. R. (2015). Titanium Ve Özellikleri [Titanium And Its Properties]. *Atatürk Üniversitesi Diş Hekimliği Fakültesi Dergisi*, 25, 151-159
- Pilliar, R. M. (2021). *Metallic Biomaterials*. *Biomedical Materials*, 1-47.
- Radha, R., & Sreekanth, D. (2017). Insight Of Magnesium Alloys And Composites For Orthopedic Implant Applications—A Review. *Journal Of Magnesium And Alloys*, 5(3), 286-312.
- Santos, G. (2017). The Importance Of Metallic Materials As Biomaterials. *Adv Tissue Eng Regen Med Open Access*, 3(1), 300-302
- Saris, N. E. L., Mervaala, E., Karppanen, H., Khawaja, J. A., & Lewenstam, A. (2000). Magnesium: An Update On Physiological, Clinical And Analytical Aspects. *Clinica Chimica Acta*, 294(1-2), 1-26.
- Sarraf, M., Rezvani Ghomi, E., Alipour, S., Ramakrishna, S., & Liana Sukiman, N. (2021). A State-Of-The-Art Review Of The Fabrication And Characteristics Of Titanium And Its Alloys For Biomedical Applications. *Bio-Design And Manufacturing*, 1-25.
- Sezer, N., Evis, Z., Kayhan, S. M., Tahmasebifar, A., & Koç, M. (2018). Review Of Magnesium-Based Biomaterials And Their Applications. *Journal Of Magnesium And Alloys*, 6(1), 23-43
- Subaşı, M., & Karataş, Ç. (2012). Titanium Ve Titanium Alaşımlarından Yapılan İmplantlar Üzerine İnceleme [Investigation on Implants Made Of Titanium And Titanium Alloys]. *Politeknik Dergisi*, 15(2), 87-103.
- Şap, S., Şap, E., & Kırık, İ. T. Alaşımlarının Biyomalzeme Olarak Kullanılması [The Use of Alloys as Biomaterials]. İii Uluslararası Battalgazi Bilimsel Çalışmalar Kongresi; 2019.



## **CHAPTER 5**

### **EVALUATION OF PHYTOREMEDIATION POTENTIAL AND YIELD OF *HELIANTHUS ANNUUS* UNDER SEWAGE SLUDGE APPLICATION**

Elham MOHAMMADIAN<sup>1</sup>

Assoc. Prof. Maryam VARAVIPOUR<sup>2</sup>

---

<sup>1</sup> PhD Scholar, Water Engineering Department, Faculty of Agricultural Technology (Aburayhan), University of Tehran, Tehran, Iran

<sup>2</sup> Assoc. Prof., Dept. of Water Engineering, Faculty of Agricultural Technology (Aburayhan), University of Tehran, Tehran, Iran



## 1. INTRODUCTION

Considering the growing trend of the world's population on the one hand and the gradual increase in the amount of environmental pollution and the subsequent destruction of an important part of agricultural lands, the basic and serious challenges of the world in the next decade on the important issue of food security from quantitative aspects and its quality will be (Amoei et al., 2012). The main source of heavy metals in the soil is the consumption of urban and industrial wastewater, chemical fertilizers, sludge from sewage treatment plants and metal mining mines (Hashemimajd, 2010). Organic fertilizers, such as sewage sludge, due to being rich in nutrients needed by plants and organic materials, increase plant performance in most cases. Researches have shown that the application of appropriate amounts of sewage sludge in the soil improves the physical conditions of the soil and provides significant amounts of plant nutrients and increases the quantity and quality of the product. While its excessive consumption is harmful and reduces the yield and quality of agricultural products (Fresques et al., 1990). Nevertheless, wastewater contains significant amounts of heavy metals, which can be a serious environmental threat to the chemical quality of soil and agricultural products, as well as health (Balkhair et al., 2016). Contamination of soil with heavy metals causes them to enter the food chain through absorption by plants. The most important effect of heavy metals in the human body is their non-metabolism, and for this reason, after entering the body, they are not excreted from the body and accumulate in the body tissues, which causes many diseases in the human body. The body suffers from neurological disorders, types of cancers, infertility, memory loss, osteoporosis, and similar cases (Sadat Taghavirad et al., 2014). A long-term field experiment with corn-wheat rotation to determine the accumulation of heavy metals with different amounts of sewage sludge showed that with an increase of 1 ton/ha.yr of applied sludge, the content of mercury, zinc, copper, lead and cadmium in the soil increased (Yang et al., 2018). Hatamian et al., (2020), investigated the accumulation of lead and cadmium in the soil and crops of wheat (using treated wastewater) and barley (combination of untreated wastewater and well water) and observed that the concentration of lead and cadmium in wastewater treatment Untreated is more than treated wastewater. The accumulation of heavy metals including copper, iron, zinc, cadmium and manganese in different organs of corn, barley, okra and parsley under irrigation with treated wastewater showed that the accumulation of various metals in the roots was more than other organs (Farmani Fard et al., 2016).

There are several important methods such as soil washing and chemical methods to remove heavy metals from contaminated soil, which are not economically viable and also have adverse effects on biological activities. One of the methods of removing toxic pollutants from sewage sludge is the phytoremediation method, which has less environmental effects. Phytoremediation is a type of technology based on the use of plants to remove pollutants from the soil at a low cost, which is compatible with the environment and is considered one of the methods of in-situ remediation and restores the place, protects biological activity, Physical structure and chemical properties of soil (Clemente et al., 2006). Many ornamental plants have the ability to extract toxic metals from the soil and are able to store high amounts of metals in their organs and at the same time continue to survive without causing toxic symptoms. On the other hand, these plants do not enter the human food chain and therefore have no health problems for humans (Liu et al., 2008). In a research, sewage sludge and biochar sludge were used for tomato production and it was observed that the highest plant dry weight, fruit number and yield were related to sewage sludge treatment (Hossain et al., 2015). Investigating the effect of irrigation with contaminated water on the accumulation of copper, iron, zinc, cadmium and manganese in two separate experiments on wheat and parsley revealed that in wheat and parsley that were irrigated with contaminated water, the accumulation of heavy metals was more than the control and its accumulation in the roots was more (Mirzaei Takhtagahi et al., 2016). Singh and Agrawal (2010) studied the effect of sewage sludge on rice and found that sewage sludge increased the concentration of cadmium in the roots, stems, leaves and grains of rice. The study of the effects of heavy metals in the pollution of urban environments was carried out with the help of simulating the soil and contaminating it with the help of heavy metals, and the role of the clover plant in the phytoremediation of polluted soils showed the values of the root bioaccumulation factor in the clover plant for heavy metals zinc, Lead, copper and cadmium were equal to 4.242, 1.544, 1.071 and 0.604 (Ali et al., 2012). The results of phytoremediation of the ornamental plant Ahar<sup>3</sup> in copper-contaminated soils showed that at low levels of the heavy metal copper in polluted areas, this plant can perform phytoremediation of copper metal (Afroosheh and Karami, 2015). Research results on the phytoremediation potential of sour tea in cleaning chromium pollution in greenhouse conditions

---

<sup>3</sup> *Zinnia elegans*

showed that the most storage of chromium is in the root of sour tea, which indicates that the transfer of this element from the root to the shoot is limited (Fatimenik, 2017).

The ornamental sunflower with the scientific name *Helianthus annuus* belongs to the *Compositae* family. Research results show that the sunflower family is one of the most important plants for phytoremediation of soils contaminated with heavy metals (Prasad, 2007). According to the conducted researches, investigating the application of sewage sludge in agricultural lands and its effect on the growth and performance of cultivated plants, as well as investigating the amount of heavy metals in sewage sludge and cultivated plants, is considered a necessary case. For this purpose, this research was conducted with the aim of determining the effect of sewage sludge on the yield of ornamental sunflower plant, the concentration of heavy metals in the soil and the plant, and also determining the plant's ability to purify heavy metals (lead, nickel and cadmium) present in the soil by this plant.

## 2. Materials and methods

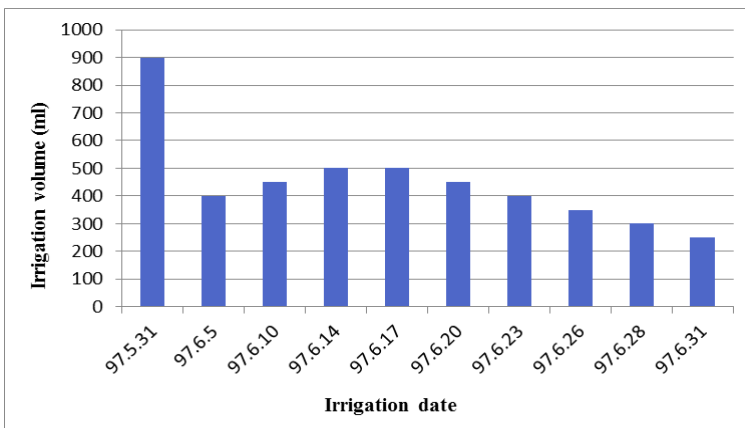
This research was carried out in the research greenhouse of Aburaihan campus of Tehran University in 2017-2018. This research was done in pots in the form of a completely randomized block design with three application levels of 0, 10 and 20% by weight of sewage sludge soil with three replications. The used soil was taken from the depth of 0-30 cm of the research farm of the Faculty of Agriculture and transferred to the research site. The sewage sludge used from the sewage treatment plant in south of Tehran was anaerobically digested. Table (1) shows some physical and chemical characteristics of soil and sewage sludge used. A comparison of the amounts of heavy metals (lead, nickel and cadmium) in the tested sludge with the standards of the American Environmental Protection Agency (USEPA, 1993) shows that the concentration of these elements in this sewage sludge is within the permissible range and has a low pollution potential.

**Table 1.** Some physical and chemical properties of soil and sewage sludge used

Property	Unit	Soil	Sewage sludge	Standard allowable limit (USEPA 1993)
Soil Texture	-	Sandy Loam	-	-
pH	-	7.7	6.45	-
EC	dS/m	0.80	16.2	-
CEC	cmol+/kg	20.1	-	-
OM	%	0.45	40.47	-
N total	%	0.172	3.69	-
K	mg/kg	99.86	328	-

Pb	mg/kg	4.6	61.35	300
Ni	mg/kg	2.3	65.7	420
Cd	mg/kg	0.409	1.1	39

The number of vases according to the number of treatments and repetitions was equal to 9 vases. At the end of July, ornamental sunflower seeds were planted in glass pots. In this way, six seeds were planted in the pots. After the 15th day of planting the seeds, the seedlings were thinned and in each pot three plants that were more resistant than the rest were kept so that there was enough space for the plant to grow and a week later each of the seedlings they were transferred to a bigger pot. In this study, plastic pots with a height of 30 cm and a diameter of 20 cm with an approximate capacity of 3 kg of soil were used. In order to prepare the treatments, the air-dried soil samples were passed through a 6 mm sieve and the sewage sludge was passed through a 1 mm sieve after being pounded, and then it was mixed with soil at zero, 10 and 20% by weight. Before filling the pots with soil treatments, some coarse sand was poured in the bottom of each pot as drainage and the pots were filled with the prepared treatments. During the growth of the plants in the greenhouse, weeding was done by hand and no other fertilizer was used except the added sludge. The pots were irrigated with city water and approximately once every four to five days up to the soil's agricultural capacity, which was done by weighing the pots (Figure 1).



**Figure. 1.** Volume and date of irrigation

Harvesting of ornamental sunflowers was done 60 days after planting and after flowering. For the harvesting operation, the aerial part was first separated from the collar. Observing and measuring the root system in a vegetable is very time-consuming and difficult. Especially, any action for



such studies requires disturbing the natural condition of the roots and causes the results of the studies to be inconsistent with reality. Although many methods have been proposed to study the roots, no method can be found to be complete enough to answer all relevant questions. There are five main methods for sampling, which are: soil drilling method, monolith method, using sampling drills, soil profile method and the method of using intact samples, which is used in this research. In this way, the soil of each pot along with the roots in it was removed from the pot and placed inside the sieve and inside the water container and the sieve was gently shaken until the soil particles were completely separated. The parameters of stem diameter and height and flower diameter were measured for all treatments. After harvesting, the plant samples were first washed with normal water and then with distilled water. The roots and aerial parts of each plant were weighed separately and placed in an oven at 75 °C for 48 hours. To determine the wet and dry yield of the plant, the wet and dry weight of the shoots and roots were measured. Dried plant samples were powdered by an electric mill and placed in plastic containers that were previously washed with dilute acid to be used in the next steps .

In order to measure the concentration of heavy metals in the plant, extracting from the plant was done by dry ashing method and extracting from soil with DTPA. The concentration of heavy metals lead, nickel and cadmium in the extracts of soil, root and shoot of the plant was measured by Perkin Elmer 1100B atomic absorption device. Transfer factor (TF) or the rate of transfer of heavy metals from roots to aerial organs was calculated from the ratio of metal concentration in aerial organs to metal concentration in roots, and root bioconcentration factor (BCF) or rate of transfer of heavy metals from soil to plant was calculated from the ratio of metal concentration. In the roots, the total metal concentration in the soil was obtained.

At the end of the experiment, the studied parameters were statistically analyzed using SAS software. After the significance of the parameters was determined, the averages were compared using Duncan's test at the 5% probability level.

### **3. RESULTS AND DISCUSSION**

#### **3.1. The amount of heavy metals in the soil**

Table (2) shows the results of analysis of variance and table (3) shows the comparison of the average effects of sewage sludge application on the

amount of heavy metals in the soil at the end of cultivation. The treatments include sewage sludge added to 0% by weight of soil (S0), 10% by weight of soil (S10) and 20% by weight of soil (S20).

**Table 2.** Analysis of variance of the effects of wastewater sludge application on the concentration of heavy metals in the soil

Sources of changes	Degrees of freedom	average of squares (SM)		
		Pb mg/kg	Ni mg/kg	Cd mg/kg
Repeat	2	0.05 <sup>ns</sup>	0.0067 <sup>ns</sup>	0.00019 <sup>ns</sup>
Treatment	2	3.58 <sup>**</sup>	0.484 <sup>**</sup>	0.0086 <sup>**</sup>
Error	4	0.022	0.0147	0.00013
Coefficient of variation		8.43	15.54	9.99

ns : no significant difference, \* : significant difference at 5% level, \*\* : significant difference at 1% level

**Table 3.** Results of comparing the mean effects of wastewater sludge application on heavy metal concentrations in soil

Treatment	Pb mg/kg	Ni mg/kg	Cd mg/kg
S0	0.66 <sup>c</sup>	0.38 <sup>c</sup>	0.055 <sup>b</sup>
S10	1.76 <sup>b</sup>	0.78 <sup>b</sup>	0.14 <sup>a</sup>
S20	2.84 <sup>a</sup>	1.18 <sup>a</sup>	0.16 <sup>a</sup>
Permissible range in the soil (SEPA, 1995) <sup>4</sup>	350	60	0.6

In each column, the averages with at least one common letter are not significantly different at the 5% probability level with Duncan's test .

### 3.1.1. Lead

Table (2) shows the results of variance analysis of the effects of sewage sludge application on soil lead content at the end of cultivation and after harvesting flowers. According to this table, the use of sewage sludge caused a significant increase in the amount of lead in the soil at the level of 1%. The lowest amount of soil lead was in the control treatment and the highest was in the S20 treatment, so that the soil lead decreased from 0.66 mg kg<sup>-1</sup> in the control treatment to 1.76 and 2.84 mg kg<sup>-1</sup> in the S10 treatment. And S20 increased. The amount of lead in the soil was also lower than the standard limit of SEPA, 1995). Lead has the highest amount among the investigated metals. The mobility of lead in soil is lower than other elements, and this element is more stabilized on the soil surface due to the high amount of organic matter and clay minerals (Singh and Agrawal, 2010). Yang et al.,

<sup>4</sup>State Environmental Protection Administration China

(2018), conducted a long-term field experiment with corn-wheat rotation to investigate the accumulation of heavy metals in a calcareous soil with different amounts of sewage sludge amendment. With the increase of 1 ton of applied sludge per hectare per year in the soil, the content of mercury, zinc, copper, lead and cadmium increased, which is consistent with the results of the present study.

### **3.1.2. Nickel**

The variance analysis table (Table 2) shows that with the increase in the level of sewage sludge, the amount of absorbable nickel in the soil increased significantly at the 1% probability level. According to the comparison of the average data in table (3), with the increase of sewage sludge in all treatments receiving sludge, the amount of nickel in the soil has increased significantly (at the level of 5%) and the lowest amount of soil nickel in the control treatment with The value of mg kg<sup>-1</sup> was 0.38 and the highest value was in S20 treatment with the value of 1.18 mg kg<sup>-1</sup>. The amount of nickel in the soil was less than the standard limit declared by SEPA, 1995). Yang et al., (2018), conducted a long-term field experiment with corn-wheat rotation to investigate the accumulation of heavy metals in a calcareous soil with different amounts of sewage sludge amendment. With the increase of 1 ton of applied sludge per hectare per year in the soil, the content of mercury, zinc, copper, lead and cadmium increased.

### **3-1-3- Cadmium**

The results of the variance analysis table (Table 2) showed that the application of sewage sludge caused a significant increase in soil absorbable cadmium at the level of 1%. Comparing the averages using Duncan's method in table (3), it shows that the consumption of sewage sludge increased soil cadmium from 0.055 mg kg<sup>-1</sup> in the control treatment to 0.16 mg kg<sup>-1</sup> in the S20 treatment, but No significant difference was observed between S10 and S20 treatments. The amount of cadmium measured in the soil was also lower than the standard limit of SEPA, 1995). Wang Ru and Su (2004), found that the concentration of available cadmium in soils that received sewage sludge increased significantly, which is consistent with the results of the present study.

### 3-2- Plant growth and performance factors

Table (4) shows the results of analysis of variance and table (5) shows the comparison of the average effects of sewage sludge application on wet and dry weight (root and shoot), stem diameter and height, and flower diameter after harvesting the flowers.

**Table 4.** Analysis of variance of the effects of wastewater sludge application on plant growth and yield

Sources of changes	Degrees of freedom	average of squares (SM)						
		Root wet weight	Root dry weight	Wet weight of aerial parts	Dry weight of aerial parts	Stem diameter	Stem Height	Flower diameter
		g	g	g	g	Cm	cm	cm
Repeat	2	2.78 <sup>ns</sup>	0.001 <sup>ns</sup>	35.26 <sup>ns</sup>	1.32 <sup>ns</sup>	0.0055 <sup>ns</sup>	0.52 <sup>ns</sup>	0.122 <sup>ns</sup>
Treatment	2	22.08 <sup>**</sup>	1.478 <sup>*</sup>	218.90 <sup>*</sup>	17.10 <sup>*</sup>	0.063 <sup>**</sup>	7.24 <sup>**</sup>	0.69 <sup>**</sup>
Error	4	0.954	0.038	16.14	1.63	0.001	0.096	0.026
Coefficient of variation		10.18	14.77	9.78	19.58	4.87	1.72	2.31

ns : no significant difference, \* : significant difference at 5% level, \*\* : significant difference at 1% level

**Table 5** Results of comparing the mean effects of wastewater sludge application on plant growth and yield

Treatment	Root wet weight	Root dry weight	Wet weight of aerial parts	Dry weight of aerial parts	Stem diameter	Stem Height	Flower diameter
	g	g	g	g	Cm	cm	cm
S0	6.67 <sup>b</sup>	0.57 <sup>c</sup>	31.77 <sup>b</sup>	3.96 <sup>b</sup>	0.50 <sup>b</sup>	16.33 <sup>c</sup>	6.5 <sup>b</sup>
S10	10.08 <sup>a</sup>	1.42 <sup>b</sup>	42.87 <sup>a</sup>	6.89 <sup>a</sup>	0.71 <sup>a</sup>	18.3 <sup>b</sup>	7.15 <sup>a</sup>
S20	12.03 <sup>a</sup>	1.97 <sup>a</sup>	48.56 <sup>a</sup>	8.69 <sup>a</sup>	0.78 <sup>a</sup>	19.4 <sup>a</sup>	7.44 <sup>a</sup>

In each column, the averages with at least one common letter are not significantly different at the 5% probability level with Duncan's test.

#### 3.2.1. Wet and dry weight of roots

The results of table (4) show that with the increase in the level of sewage sludge, the fresh and dry weight of the root increased significantly at the probability level of 1%. Comparison of averages using Duncan's method (Table 5) also shows that root wet weight increased with increasing sewage

sludge in all treatments receiving sludge, but no significant difference was observed between treatments S10 and S20. The dry weight of the roots also increased significantly (at the level of 5%) with the increase of sewage sludge in both treatments compared to the control treatment. The highest amount of root dry weight was related to S20 treatment with g value of 1.97 and the lowest value was in the control treatment with g value of 0.57. Therefore, the addition of sewage sludge to the soil has caused an increase in organic carbon and, subsequently, an improvement in the physical properties of the soil, which has a direct effect on the growth and development of the roots. Morera et al., (2002), grew sunflower plants in soils treated with sludge and observed that the addition of sewage sludge significantly increased the average dry weight of sunflower compared to the control soil, which is in agreement with the results of the present study. Correspond.

### **3.2.2. Wet and dry weight of aerial parts**

The use of sewage sludge caused a significant increase in fresh and dry weight of aerial parts at the level of 5% (Table 4). Comparing the averages using Duncan's method in table (5), it shows that the consumption of sewage sludge increases the fresh weight of the shoot from 31.77 g in the control treatment to 48.56 g in the S20 treatment and the dry weight of the shoot increases from 3.96 g in the control treatment was 8.69 g in the S20 treatment, but no significant difference was observed between the S10 and S20 treatments. This increase in yield is due to the high consumption of nutrients such as nitrogen, potassium and phosphorus and low consumption nutrients of iron, manganese and zinc in sewage sludge. Urbaniak et al., (2017), reported that the consumption of sewage sludge in willow plants increased the willow biomass, which is consistent with the findings of this study.

### **3.2.3. The height and diameter of the stem**

The application of sewage sludge increased the height and diameter of the stem at the 1% probability level (Table 4). The lowest stem height and diameter was in the control treatment and the highest in the S20 treatment, so that the stem height was from 16.33 cm in the control treatment to 19.40 cm in the S20 treatment and the stem diameter was from 0.50 cm in the treatment. The control reached 0.78 cm in S20 treatment. But no significant difference in stem diameter was observed between S10 and S20 treatments (Table 5). The increase in the height and diameter of the stem is due to the increase in the

high-use and low-use food elements that can be absorbed by the plant. These results are consistent with the research of Abbasi et al., (2013) who, in a greenhouse study, grew rice plants in a calcareous soil and reported that the height of the stem increased with the consumption of sewage sludge.

### 3.2.4. Flower diameter

The results of analysis of variance in table (4) show that the use of sewage sludge caused a significant increase in the diameter of mud at the level of 1%. The comparison of the averages in table (5) also shows that the flower diameter has increased significantly (at the level of 5%) with the increase of sewage sludge in both treatments compared to the control treatment, but there is a significant difference between the treatments. S10 and S20 were not observed. The maximum and minimum flower diameter of the S20 treatment is equal to 7.44 cm and the control treatment is equal to 6.5 cm. This increase is due to the high amount of nutrients such as nitrogen, potassium and phosphorus in sewage sludge.

### 3-3- Amount of heavy metals in the plant

Table (6) shows the results of analysis of variance and table (7) shows the comparison of the average effects of sewage sludge application on the amount of heavy metals in plants (roots and shoots) at the end of cultivation and after harvesting flowers.

**Table 6.** Analysis of variance of the effects of sewage sludge on plant heavy metal concentrations

Sources of changes	Degrees of freedom	average of squares (SM)					
		Pb (mg/kg)		Ni (mg/kg)		Cd (mg/kg)	
		Aerial parts	Root	Aerial parts	Root	Aerial parts	Root
Repeat	2	0.115 <sup>ns</sup>	0.286 <sup>ns</sup>	0.064 <sup>ns</sup>	0.22 <sup>ns</sup>	0.0005 <sup>ns</sup>	0.0005 <sup>ns</sup>
Treatment	2	10.06 <sup>**</sup>	40.14 <sup>**</sup>	2.01 <sup>**</sup>	5.36 <sup>**</sup>	0.064 <sup>**</sup>	0.158 <sup>**</sup>
Error	4	0.024	0.151	0.0048	0.043	0.0009	0.001
Coefficient of variation		6.27	6.91	5.78	8.72	12.75	7.60

ns : no significant difference, \* : significant difference at 5% level, \*\* : significant difference at 1% level

### 3.3.1. Lead

The variance analysis table (Table 6) shows that with the increase in the level of sewage sludge, the amount of lead in the shoot and root significantly increased at the 1% probability level. According to the comparison of the average data in table (7), with the application of sewage sludge, the amount of lead (aerial organ and root) increased significantly compared to the control treatment, and the lowest amount of lead was in the control treatment and the highest in the S20 treatment. The accumulation of lead metal for all treatments was more in the roots than in the shoots, so that the highest amount of lead metal in the roots and shoots of the S20 treatment was equal to 9.09 mg kg<sup>-1</sup> and 4.35 mg kg<sup>-1</sup>, respectively. The amount of lead measured in the plant (aerial organ and root) was within the permissible standard range (SEPA, 2005). Nisi et al., 2014, investigated the phytoremediation of heavy metals by the sunflower plant, and the results showed that the sunflower plant used to remove heavy metals had the highest absorption of lead and cadmium through the roots of the plant, which is consistent with the results of the present study.

**Table 7.** Results of comparing the mean effects of wastewater sludge application on plant heavy metal concentrations

Treatment	Pb (mg/kg)		Ni (mg/kg)		Cd (mg/kg)	
	Aerial parts	Root	Aerial parts	Root	Aerial parts	Root
S0	0.69 <sup>c</sup>	1.80 <sup>c</sup>	0.41 <sup>c</sup>	0.99 <sup>c</sup>	0.073 <sup>c</sup>	0.161 <sup>c</sup>
S10	2.44 <sup>b</sup>	5.98 <sup>b</sup>	1.15 <sup>b</sup>	2.51 <sup>b</sup>	0.253 <sup>b</sup>	0.493 <sup>b</sup>
S20	4.35 <sup>a</sup>	9.09 <sup>a</sup>	2.04 <sup>a</sup>	3.65 <sup>a</sup>	0.364 <sup>a</sup>	0.598 <sup>a</sup>
Permissible range in the plant (SEPA, 2005) <sup>5</sup>	9.0		10		0.2	

In each column, the averages with at least one common letter are not significantly different at the 5% probability level with Duncan's test.

### 3.3.2. Nickel

Table (6) shows the results of variance analysis of the effects of sewage sludge application on plant nickel content at the end of cultivation and after harvesting flowers. According to this table, the use of sewage sludge caused a significant increase in the amount of nickel in shoots and roots at the

<sup>5</sup>State Environmental Protection Administration China

level of 1%. The lowest amount of nickel (aerial organ and root) was in the control treatment and the highest was in the S20 treatment, so that the nickel in the aerial organ increased from 0.41 mg kg<sup>-1</sup> in the control treatment to 2.04 mg kg<sup>-1</sup> in the treatment S20 and root nickel (mg/kg) reached from 0.99 mg kg<sup>-1</sup> in the control treatment to 3.65 mg kg<sup>-1</sup> in the S20 treatment. Ni metal accumulation was higher in plant roots than in shoots for all treatments (Table 7). The amount of nickel in the shoots and roots was lower than the permitted standard limit (SEPA, 2005). Guoqing et al., (2019), conducted a two-year experiment to determine the effect of sewage sludge application on the distribution of heavy elements in poplar and concluded that sewage sludge affected the accumulation of nickel and lead in the aerial parts of poplar, which was consistent with the results. The present research is consistent.

### **3.3.3. Cadmium**

The variance analysis table (Table 6) indicates that the application of sewage sludge caused a significant increase in cadmium in shoots and roots at the level of 1%. Comparison of the averages by Duncan's method in table (7) shows that the consumption of sewage sludge increases the cadmium of aerial organs from 0.073 mg kg<sup>-1</sup> in the control treatment to 0.364 mg kg<sup>-1</sup> in the S20 treatment and increases The root cadmium increased from 0.161 mg kg<sup>-1</sup> in the control treatment to 0.1598 mg kg<sup>-1</sup> in the S20 treatment, and the accumulation of cadmium metal was more in the plant roots than in the aerial parts for all treatments. By comparing the amount of cadmium in roots and shoots after applying the treatments with the standard limit (SEPA, 2005), it can be seen that the amount of cadmium has reached the level of plant toxicity. Nisi et al., 2014, investigated the phytoremediation of heavy metals by the sunflower plant, and the results showed that the sunflower plant had the most absorption of lead and cadmium through the plant roots, which is consistent with the results of the present study.

### **3.4. Transfer factor and bioConcentration of heavy metals**

Plants are divided into three categories in terms of absorption and transport of heavy metals. The first group are plants that store heavy metals in their tissues and the effects of metal toxicity in these plants are yellowing, shriveling and premature aging of the leaves, which are called indicator plants and have TF and BCF equal to one (Olowoyo et al., 2010). The second category are plants that effectively prevent the entry of metal into their aerial parts by using the plant stabilization mechanism, and are known as avoidant



plants, and in them, TF is smaller than one and BCF is larger than one. (Mcfaralane et al., 2007). The third group are plants that have the ability to absorb and accumulate metal in low to high pollution by using the absorption plant mechanism, and they are called accumulating plants and have TF and BCF greater than one (Memon et al. , 2001).

The transfer factor and root bioaccumulation for heavy metals (lead, nickel and cadmium) in different sewage sludge treatments for ornamental sunflower plants are presented in Table (8).

**Table 8.** Translocation factor and bioConcentration factor for heavy metals in different treatments

Treatment	Pb		Ni		Cd	
	TF	BCF	TF	BCF	TF	BCF
S0	0.39	2.72	0.42	2.91	0.45	2.99
S10	0.41	3.41	0.47	3.21	0.51	3.66
S20	0.48	3.21	0.57	3.10	0.61	3.83

As can be seen, with the increase of sewage sludge, the amount of transfer factor from roots to shoots in all metals has increased compared to the control treatment, and the S20 treatment has a larger TF than the S10 treatment for all three metals. The amount of root bioaccumulation factor of metals increased with the addition of sewage sludge compared to the control treatment, but the increase between the S10 and S20 treatments did not have a regular trend, so that the S10 treatment had more BCF than the S20 treatment for lead and nickel metals. Cadmium metal, the bioaccumulation factor of S20 treatment is more.

According to table (8), the bioaccumulation factor from the soil to the roots of the three investigated heavy metals is greater than one, which indicates that the amount of heavy metals in the plant roots is more than in the soil and indicates These metals are absorbed from the soil. The trend of increasing the bioaccumulation factor from the soil to the roots of the mentioned metals was opposite: cadmium > lead > nickel. The high level of this factor in cadmium metal is due to the fact that cadmium is one of the elements that joins the soluble part of organic matter (fulvic acid) and moves easily in the soil and is absorbed by the plant.

The transfer factor from the root to the shoot in the studied heavy metals is less than one, which indicates that the amount of heavy metals in the

root is more than the shoot and these metals stop in the root area. The trend of increasing transfer factor from root to shoot among the examined metals was opposite: cadmium > nickel > lead. The low level of the transfer factor in lead metal is due to the less movement of lead in the plant and its greater accumulation in the root.

Ndeda et al., (2014) by examining the bioaccumulation factor and transfer factor of heavy metals, reported that cadmium has the highest bioaccumulation factor among heavy metals, and among other metals, it is in the order of copper > lead > nickel. Also, lead had the lowest amount of transfer factor among other heavy metals. The result of this review is consistent with the results of this research.

Therefore, according to the bioaccumulation factor above one and the transfer factor less than one, it can be said that the ornamental sunflower plant is an avoidant plant in terms of absorption and transfer of heavy metals, lead, nickel and cadmium.

#### **4. CONCLUSION**

This research was conducted in order to investigate the effect of sewage sludge on the performance of the ornamental sunflower plant, the concentration of heavy metals in the soil and the plant, and also to investigate the plant's ability to purify the heavy metals (lead, nickel and cadmium) present in the soil by this plant. The most important results of this research are:

1- The application of sewage sludge caused a significant increase in the concentration of heavy metals (lead, nickel and cadmium) that can be absorbed by the soil compared to the control treatment. The increasing trend of the amount of heavy metals in the soil is lead > nickel > cadmium. The use of sludge in high amounts and in the long term can lead to the gradual accumulation of heavy metals in the soil and cause environmental problems.

2- Considering that the use of sewage sludge at the rate of 20% by weight of the soil in the measured traits (including fresh and dry weight of roots and shoots, diameter and height of the stem, diameter and number of flowers) was the best result, the use of sludge to The amount of 20% by weight of soil in greenhouse conditions is suggested to produce more yield of ornamental sunflower plant in similar soils and use in green spaces.

3- By calculating the bioaccumulation factor from the soil to the roots of heavy metals, it was seen that the amount of heavy metals in the roots is more than in the soil, indicating the absorption of these metals from the soil. The trend of increasing the bioaccumulation factor from the soil to the roots of metals was opposite: cadmium > lead > nickel.

4- Determining the transfer factor from roots to aerial organs in heavy metals showed that these metals were mostly concentrated in roots and a small part of them were transferred to aerial organs. The trend of increasing transfer factor from root to shoot among the studied metals was opposite: cadmium > nickel > lead.

5- According to the bioaccumulation factor above one and the transfer factor smaller than one for all three investigated metals, it can be concluded that the ornamental sunflower plant is an avoidant plant against the absorption and transfer of lead, nickel and cadmium heavy metals.

## REFERENCES

- Abbasi, M., Najafi, N., Asgharzadeh, N. and Avestan S. (2013). Effect of soil water conditions, sewage sludge, poultry manure and chemical fertilizers on growth characteristics and water use efficiency of rice plant in a calcareous soil. *J. Water Soil Know.* 23(1), 189-208 [In Persian].
- Afroosheh, M., and Karami Zare, F. (2016). Phytoremediation of *Zinnia elegans* ornamental plants under heavy metal stress conditions. Second National Conference on Sustainable Management of Soil Resources and Environment (Soil Quality, Health and Safety), Kerman, Department of Soil Science and Engineering, Shahid Bahonar University, Kerman. [In Persian].
- Ali, H., Naseer, M., Sajad, M. A. (2012). Phytoremediation of heavy metals by *Trifolium alexandrinum*. *Int. J. Environ. Sci.* 2 (3):1459–1469.
- Amoei, A., Mahvi, A., Nedafi, K., Fahimi, H., Mesdaghinia, A. R., and Naseri, S. (2012). Investigation of optimal operating conditions in phytoremediation of lead and cadmium contaminated soils by native plants of Iran. *Scientific Journal of Kurdistan University of Medical Sciences*, 17 (4), pp. 102-93 [In Persian].
- Balkhair, K. S., and Ashraf, M. A. (2016). Field accumulation risks of heavy metals in soil and vegetable crop irrigated with sewage water in western region of Saudi Arabia. *Saudi J Biol Sci.* 23(1): 32-44.
- Clemente, R., Concepción, A., and Pilar Bernal, M. (2006). A remediation strategy based on active phytoremediation followed by natural attenuation in a soil contaminated by pyrite waste. *Environmental Pollution* 143. 3: 397-406.
- Farmani Fard, M., Qamarnia, H., Pirsaeheb, M. and Fattahi, N. (2016). Study of heavy metal accumulation in different crops under the influence of irrigation with treated Kermanshah municipal wastewater, *Journal of Water and Irrigation Management*, 6 (2), pp. 365-347 [In Persian].
- Fatimenik, F. (2017). Investigation of Chromium Phytoremediation Potential by *Hibiscus sabdariffa* L. in Greenhouse Conditions, First National Conference on the Role of Medicinal Plants in Resistance Economics, Payame Noor University, Fereidounshahr.
- Fresques, P. R., Francis, R. E., and Dannis, G. L. (1990). Sewage sludge effect on soil and plant quality in a degraded semi-arid grassland. *J. Environ. Qual.* 19: 324-329.

- Guoqing, X., Xiuqin, C., Liping, B., Hongtao, Q., and Haibo, L. (2019). Absorption, accumulation and distribution of metals and nutrient elements in poplars planted in land amended with composted sewage sludge: A field trial. *Ecotoxicology and environmental safety*, 182, p.109360.
- Hashemimajd, K. (2010). Production of compost and vermicompost from organic waste. Ayizh Publication, 192 p.
- Hatamian, L., Rafati, M. and Farsad, F. (2020). The effect of wastewater irrigation on the accumulation of lead and cadmium in soil and wheat and barley grains. *Journal of Water and Irrigation Management*, 9 (2), pp. 332-321 [In Persian].
- Hossain, M. K., Strezov, V., and Nelson, P. F. (2015). Comparative assessment of the effect of wastewater sludge biochar on growth, yield and metal bioaccumulation of cherry tomato. *Pedosphere*, 25(5): 680-685.
- Liu, J. N., Zhou, Q. X., Sun, T., and Wang M. L. (2008). Growth response of three ornamental plants to Cd and Cd-Pb stress and their metal accumulation characteristics. *Journal of Hazardous materials*. 151: 261-267.
- Memon, A., Aktoprakligil, D., Ozdemir, A. and Vertii, A. (2001). Heavy metal accumulation and detoxification mechanisms in plants. *Turkish Journal of Botany*. 25: 111-121.
- Mirzaei Takhtagahi, H., Qamarnia, H., Pirsaeheb, M. and Fattahi, N. (2016). The effect of irrigation with polluted water on the accumulation of heavy metals in wheat and parsley, *Journal of Water and Irrigation Management*, 6 (2), pp. 330-315 [In Persian].
- Morera, M. T., Echeveria, J., and Garrido, J. (2002). Bioavailability of heavy metals in soil amended with sewage sludge. *Can. J. Soil Sci.* 82: 433-438.
- Mcfaralane, G. R., Koller, C. E. and Blomberg, S. P. (2007). Accumulation and partitioning of heavy metals in mangroves: A synthesis of field-based studies. *Chemosphere*. 69: 1454-1464.
- Ndeda, L. A. and Manohar, S. (2014). Bio Concentration Factor and Translocation Ability of Heavy Metals within Different Habitats of Hydrophytes in Nairobi Dam, Kenya. *Journal of Environmental Science, Toxicology and Food Technology*. 8(5): 42-45.

- Nisi, A., Vosoughi, M., Mohammadi, B., Mohammadi, M., Naeem Abadi, A., and Hashemzadeh, B. (2014). Phytoremediation of heavy metals by sunflower. *A Review Study*, 2 (2), pp. 55-65.
- Olowoyo, J. O., Heerden, E., Fischer, J. L. and Baker, C. (2010). Trace metals in soil and leaves of *Jacaranda mimosifolia* in Tshwane area, South Africa. *Atmospheric Environment*. 44: 1826-1830.
- Prasad. M. N. V. (2007). Sunflower (*Helianthus annuus* L.): A potential crop for environmental industry. *Helia*.vol. 30, br. 46, str. 167-174.
- Sadat Taghavi-rad, S., Davar, H., and Mohammadi, M. J. (2014). The a study on concentration of BETX vapors during winter in the department of ports and shipping located in one of the southern cities of Iran. *Int J Cur Life Sci.*; 4(9): 5416-5420.
- SEPA. (1995). "Environmental Quality Standards for Soils." State Environmental Protection Administration, China. GB 15618.
- SEPA. (2005). "The limits of pollutants in food." China: State Environmental Protection Administration. GB 2762- 2005.
- Singh, R. P., and Agrawal, M. (2010). Variations in heavy metal accumulation, growth and yield of rice plants grown at different sewage sludge amendment rates. *Ecotoxicology and Environmental Safety*, 73: 632-641.
- Sipos, P., Nemeth, T., and Mohai, I. (2005). "Distribution and possible immobilization of lead in a forest soil (Luvisol) profi le." *Environ. Geochem. Health* 27:1-10.
- U.S. Environmental Protection Agency. (1993). Clean water act. Section 503, Vol. 58, No. 32, USEPA, Washington ,DC.
- Urbaniak, M., Wyrwicka, A., Tołoczko, W., Serwecińska, L. and Zieliński, M. (2017). The effect of sewage sludge application on soil properties and willow (*Salix* sp.) cultivation. *Science of the Total Environment*, 586, pp.66-75.
- Wang Ru, S. J., and Su, D. (2004). Characteristics of Cd uptake and accumulation in two Cd accumulator oilseed rape species. *J. Environ. Sci.* 16: 594-598.
- Yang, G. H., Zhu, G. Y., Li, H. L., Han, X. M. and Li, J. M. (2018). Accumulation and bioavailability of heavy metals in a soil-wheat/maize system with long-term sewage sludge amendments. *Journal of Integrative Agriculture*, 17(8), pp.1861-187.

## **CHAPTER 6**

### **FLOW CHARACTERISTICS OVER BIO-INSPIRED CORRUGATED AIRFOIL AT LOW REYNOLDS NUMBER**

Assist. Prof. Dr. Hacımurat DEMİR<sup>1</sup>

Batuhan KAYA<sup>2</sup>

---

<sup>1</sup> Aksaray University, Turkey hmdemir@aksaray.edu.tr, ORCID NO: 0000-0002-4819-2633

<sup>2</sup> Aksaray University, Turkey batu5683@gmail.com, ORCID NO: 0009-0007-7398-5364





## 1. INTRODUCTION

A corrugated airfoil is a term commonly used to describe thin airfoils that are perpendicular to the free stream [1]. This type of airfoil is commonly found in insect wings, serving as a good subject for studying aerodynamics at low Reynolds numbers owing to the small dimensions of insects that can fly at relatively low speeds. Insects capable of gliding, such as the dragonfly, serve as a natural model for improving aerodynamic flight efficiency without flapping. Multiple studies have demonstrated the superior aerodynamic performance of corrugated airfoil designs in terms of range and endurance [2]. Recently, scientists have focused on low Reynolds aerodynamics as a result of advances in micro-aircraft, unmanned aircraft, and wind turbines. [3-11] In particular, there has been a rise in the quantity of research concentrating on flow around corrugated airfoils. Gao et al. [12] conducted a simulation of the airflow around a corrugated airfoil at a Reynolds number of 55,000 and then compared their findings with the experimental data obtained by Murphy and Hu [13]. It was determined that at this Reynolds number, the flow exhibits turbulent behavior, and the dissipation of three-dimensional vorticity cannot be ignored. Additionally, Murphy and Hu [14] conducted a study on the aerodynamic capabilities of bio-inspired corrugated airfoils in comparison to a smooth-surfaced airfoil and a flat plate, with the aim of investigating the potential applications of such bio-inspired corrugated airfoils for MAV. The results indicated that the corrugated airfoil outperformed the smooth-surfaced airfoil and flat plate, exhibiting higher lift and a greater ability to inhibit large-scale flow separation. Furthermore, it was observed that the corrugated airfoil was almost insensitive to Re numbers in terms of aerodynamic performance. In addition to this, Hord and Lian [15] investigated the complicated vortex formations that occurred in the valleys of the corrugated airfoil using CFD at  $Re=1000$ . They conducted comparisons between experimental results at various Re numbers and models of a flat plate. In contrast to the investigations conducted at high Re numbers, their research demonstrated that at low Re numbers, the presence of corrugation did not yield any aerodynamic advantage when compared to a flat plate. Conversely, the corrugated airfoil produced a greater amount of drag compared to the flat plate. The structural research revealed that the presence of wing corrugation enhanced the wing structure's ability to withstand bending forces. The researchers determined that the corrugated wing offered the advantage of maintaining the same level of resistance to bending forces while being significantly thinner and lighter.

New et al. [16] performed an experimental study about aerodynamic flow separation control using bio-inspired corrugated wings. They made comparisons between a technical NACA0010 and simplified dragonfly wing-based corrugated aerofoils at  $Re=14,000$  conditions. Particle streak photography flow visualizations demonstrated that, when subjected to static test conditions, the corrugated aerofoil effectively minimized flow separations and consequent wake development, in contrast to the technical aerofoil. This was accomplished by attracting the free-stream fluid towards the surface of the aerofoil through the vortices that were captured and the recirculating area that developed above the corrugated aerofoil. Additionally, New et al. [17] conducted an experimental investigation of the impact of surface features on aerofoil flow separation control at  $Re=14,000$ . The results revealed that the corrugated B aerofoil exhibited superior flow separation control behavior in comparison to the corrugated A and NACA0010 aerofoils, producing notably smaller flow separation bubbles. This may result from the formation of a large-scale recirculating region at its saddle location. The results showed that a larger recirculation area was more effective in mitigating flow separation behavior compared to using multiple smaller recirculation areas. In addition, the presence of a trailing-edge hump facilitated flow reattachment and reduced the size of the flow separation bubble.

Ren et al. [18] conducted a study to examine the impact of dragonfly wing structure on dynamic performances using both experimental and numerical methods. They stated that the corrugations on the dragonfly wings, both in the direction of the wing's span and chord, could autonomously adjust the shapes of the wings and so influence the airflow surrounding the wings of the insect. Sridhar and Dwivedi [19] conducted a numerical analysis to examine the effect of peak shape in a bio-inspired corrugated wing at a Reynolds number of  $3.5 \times 10^4$  using ANSYS Fluent with the  $k-\epsilon$  turbulence model. The aerodynamic and flow parameters exhibited that the curved peak corrugation model gave better performances than the triangular corrugation. The study revealed that the leading-edge vortices were trapped in identical locations in the first valley for both models. Nevertheless, no trailing edge vortices were observed in either model for angles of attack tested up to 12 degrees. Biradar et al. [20] investigated the effect of attack angle on lift and drag of a bio-inspired corrugated airfoil numerically. The authors stated that a low flapping angle of the corrugated airfoil gave better results, as a low angle of attack provided an ideal lift-drag ratio. The rate of flow separation was

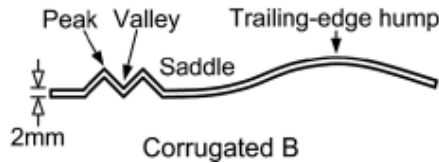
significantly greater at an angle of attack of  $15^\circ$  compared to other angles, and once the flow detached from the tip of the aerofoil, it did not reattach. In this particular instance, it was determined that an angle of  $5^\circ$  yielded the most favorable  $C_L/C_D$  ratio. Moreover, Shabbir et al. [21] carried out a CFD analysis investigating the effects of peak shape variations on the aerodynamic performance of a corrugated airfoil at Reynolds numbers of 125,000 and 58,000. The study revealed significant alterations in the airfoil's aerodynamic performance due to changes in peak shape, affecting both  $C_L$  and  $C_D$  values and the response to Re changes. A rise of 5% in peak height led to powerful vortices in the forward valley, but the vortex in the aft valley spilled over to the downstream valley, leading to a rise in  $C_D$ .

The objective of this study is to numerically investigate the aerodynamic flow characteristics of bio-inspired corrugated airfoils at a constant Reynolds number of  $1.4 \times 10^4$  with changing angles of attack utilizing the ANSYS Workbench. Furthermore, the rounding effects of the first and second peaks of the corrugated airfoil were also assessed via numerical simulations.

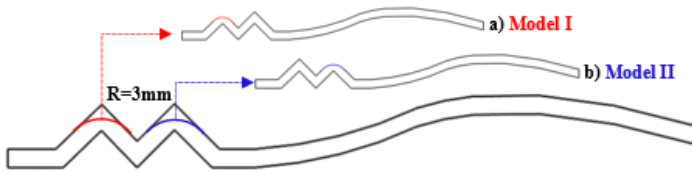
## **2. MATERIAL AND METHOD**

### **2.1. Numerical Method**

To study the flow behaviors on the airfoil, the cross-section of the dragonfly airfoil previously studied by New et al. [17] was considered, as shown in Figure 1. The corrugated B airfoil had a chord of  $c=75$  mm and a thickness of 2 mm. In this work, the Reynolds Averaged Navier-Stokes Equations were solved using a  $k-\omega$  STT turbulence model using the ANSYS Workbench to conduct 2-D, steady-state numerical simulations at a constant Reynolds number of  $1.4 \times 10^4$ . SOLIDWORKS was utilized to generate the geometries of the airfoils. The design indicated in Figure 2 has a chord length of 75 mm, using the corrugated B dragonfly airfoil. Figure 2 depicts a schematic representation of the bio-inspired corrugated B airfoils that have been created by filleting the geometries of the first peak (Model I) and the second peak (Model II) to a radius of 3 mm.

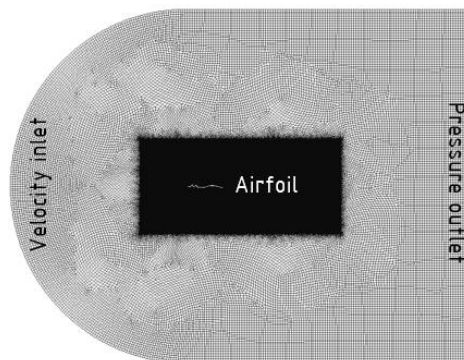


**Figure 1.** Schematic view of corrugated B airfoil [17]



**Figure 2.** Schematic view of a) first peak rounded (Model I) and b) second peak rounded (Model II) corrugated B airfoils

As seen in Figure 3, the flow domain was constructed as a half-circular arc and a rectangular block in the upstream and downstream directions, respectively. A rectangular region of influence was created around the airfoil to accurately capture the complex flow patterns. Additionally, the leading edge of the airfoil was settled at a distance of  $5C$ , while the domain was enlarged up to  $7C$  from the trailing edge. For pressure-velocity coupling, COUPLED algorithm was utilized. Additionally, the least squares cell-based method was selected for gradient and for all other parameters second-order upwind method was utilized. The convergence of the computations was obtained when the residuals were lower than  $10^{-6}$ .



**Figure 3.** The computational grid, domain and boundary conditions

## 2.2. Model Validation

To verify the accuracy of the numerical simulation, a comparison was made between the outcomes of the current study and the results of the experimental investigation performed by New et al. [17]. Figure 4 illustrated that when the angle of attack was raised, there was a clear increase in the size of the areas where the flow separated above the upper surfaces of all airfoils. The flow patterns around the airfoil exhibited significant concurrence with previous experimental study [17], whereby the flow separation bubble gradually enlarged as the angle of attack increased. Moreover, when the angle of attack increased, the point of flow separation shifted towards the leading edge, as anticipated.

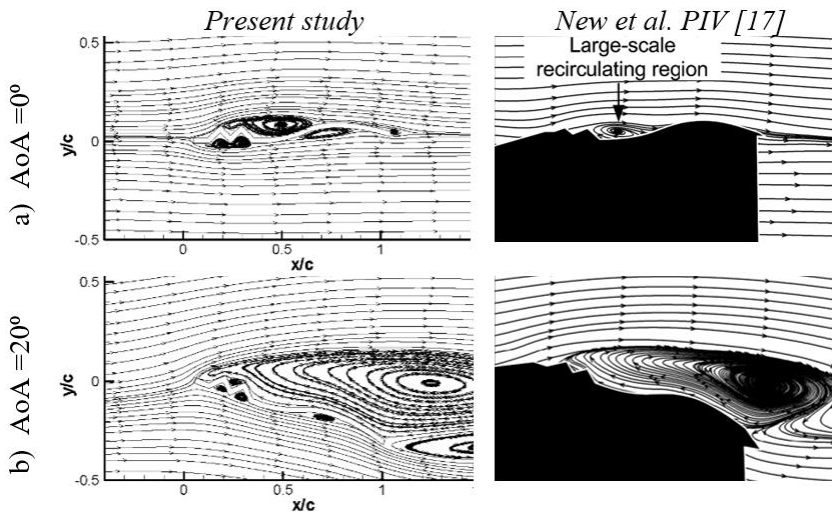


Figure 4. The streamline distributions of Corrugated B airfoil for validation

## 3. RESULTS

When the variation of the lift coefficient ( $C_L$ ) with the angle of attack given in Figure 5 was analyzed, it was seen that the corrugated B airfoil and the Model II airfoil were similar at low angles of attack ( $AoA=0^\circ$  and  $AoA=4^\circ$ ), while the Model I airfoil had a lower  $C_L$ . When the angle of attack increased from  $AoA=8^\circ$  to  $AoA=10^\circ$ , a decrease in the  $C_L$  of the corrugated B airfoil was observed. In the Model I airfoil, the maximum  $C_L$  value was reached at  $AoA=10^\circ$  and stall occurred after this angle of attack. In general, at low angles of attack and at angles of attack after  $AoA=8^\circ$ , the graph of the

change in the  $C_L$  coefficient of the corrugated B airfoil and the Model II airfoil with the angle of attack had similar characteristics. At high angles of attack, the  $C_L$  coefficient of all three airfoils changed at a similar rate with the angle of attack. Figure 6 illustrates the variation of the ratio of the lift coefficient ( $C_L$ ) to the drag coefficient ( $C_D$ ). It was clearly seen that the Model I airfoil had the highest  $C_L/C_D$  value at  $AoA=8^\circ$ . As mentioned before, except for the  $AoA=8^\circ$ , the corrugated B airfoil and the Model II airfoil showed similar characteristics at other values of  $AoA$ . While rounding the second peak of the wing did not contribute to the aerodynamic performance, rounding the first peak caused a positive change in the flow characteristics.

Figure 7 demonstrates the contours of velocity distribution around the airfoils at different angles of attack. For all airfoils, an increase in the velocity value was seen at the location where the airflow made contact with the airfoil at its first peak. Additionally, the velocity distribution value consistently exhibited greater values on the upper surface of all airfoils. As the angle of attack ( $AoA$ ) increased, the upper surface velocity zone expanded towards the trailing edge, and the stagnation point shifted aft on the lower surface. While the velocity contours for the corrugated B airfoil and the Model II wing had almost the same pattern, the Model I showed considerable differences. The contours of pressure coefficient ( $C_p$ ) around the airfoils for varying angles of attack were given in Figure 8. A low-pressure zone was seen on the top surface in all three models. This occurred due to a corrugated first peak, which caused an acceleration in the flow. As a result, a low-pressure zone was formed on the top surface, while a high-pressure region was formed on the lower surface. As the angle of attack increased, the low-pressure area on the upper wing surface (blue region) expanded, and at the same time, the high-pressure area on the lower surface (red area) also grew.

Figure 9 displays the comparison of streamline patterns around the airfoils with different angles of attack. At the lowest angle of attack,  $AoA=0^\circ$ , the flow separated from the first peak of the airfoil. The trapped vortex was observed in the valley of the Model I airfoil. In both the corrugated B and the Model II airfoils, the recirculation zone extended to the first peak. At  $AoA=8^\circ$ , flow separated from the leading-edge due to the relatively sharp corners. It was seen that separated flows were trapped within the valley between the sharp corrugations and the region upstream of the hump to form recirculating vortices. Additionally, trapped vortices were observed in all three airfoils. After recirculation at the saddle section, the flow was observed to reattach at

the hump section, but the trailing edge separation became more prominent. Trapped vortices formed in the valley section of both the corrugated B and the Model I airfoils. However, in the Model II airfoil, the recirculation region formed in the saddle section merged and mixed with the trapped vortex formed in the valley section. At  $AoA=10^\circ$  in all three airfoils, the vortices breaking off from the trailing edge merged with the vortex in the saddle section and extended to the first peak. At  $AoA=20^\circ$ , the flow was completely separated, and the flow pattern was the same on all airfoils. In addition, trapped vortices on the underside of the airfoil had been detected and had not been completely dissipated.

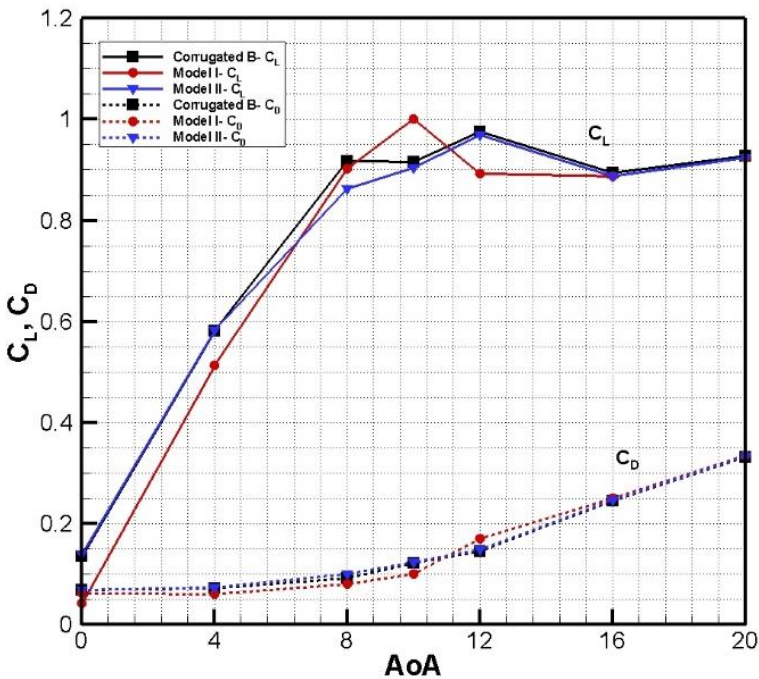
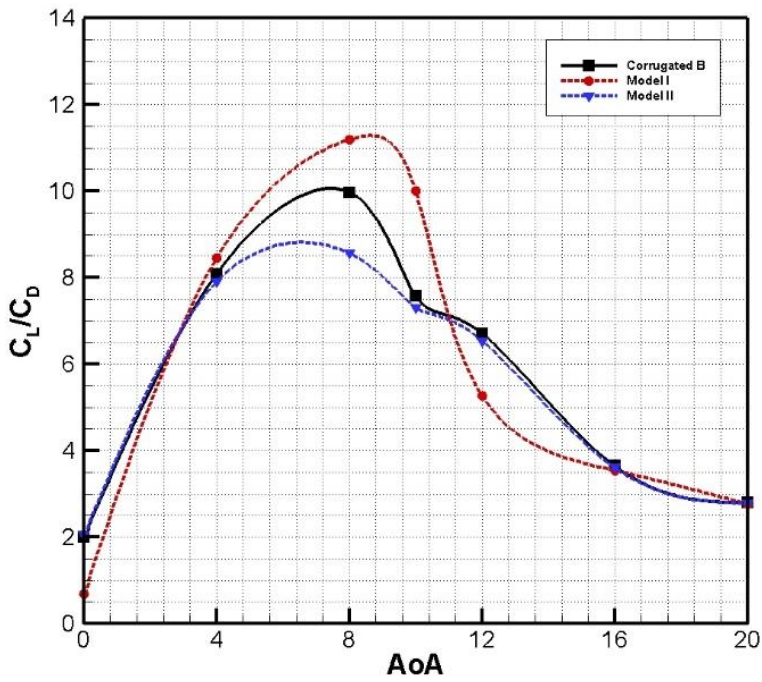
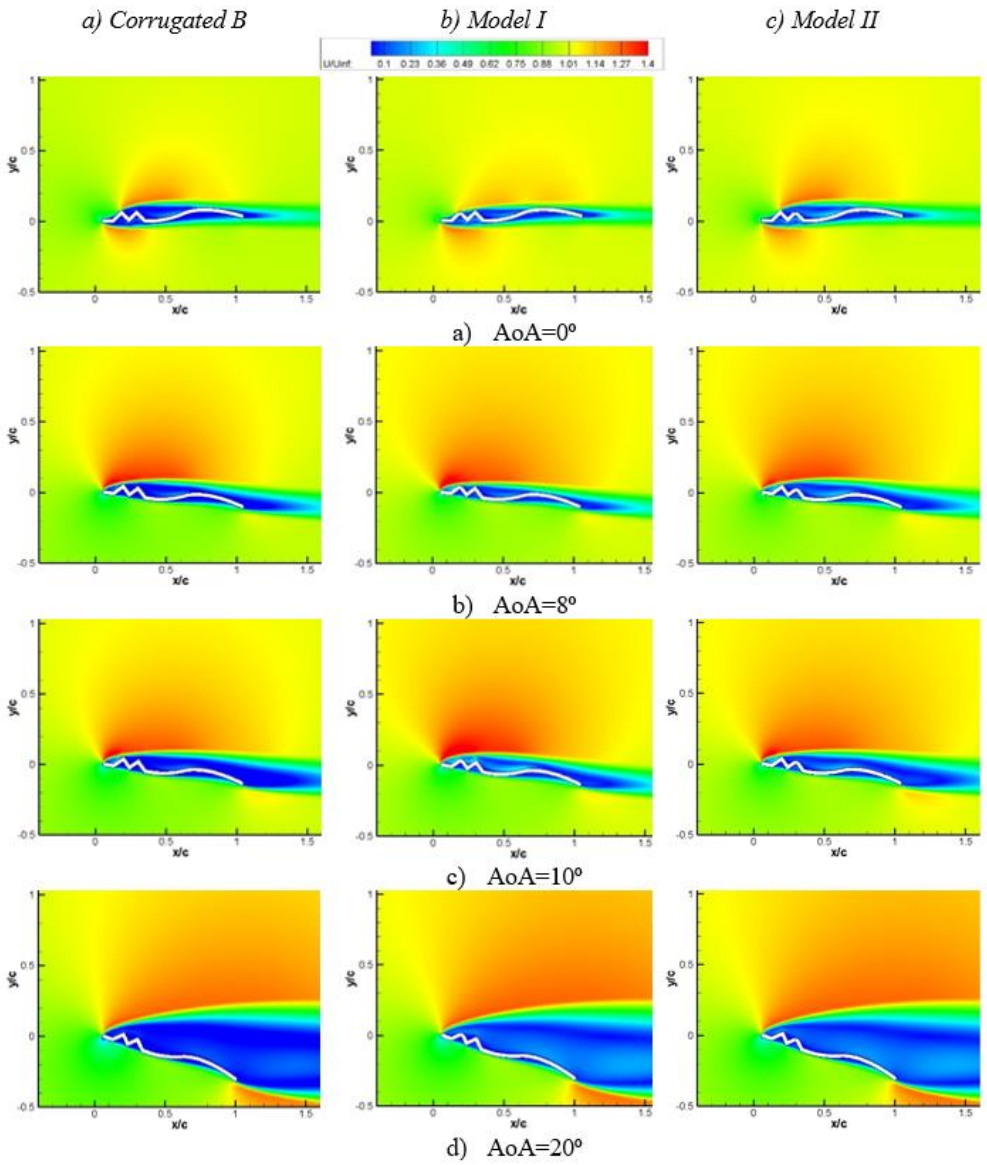


Figure 5. Aerodynamic force coefficients of airfoils

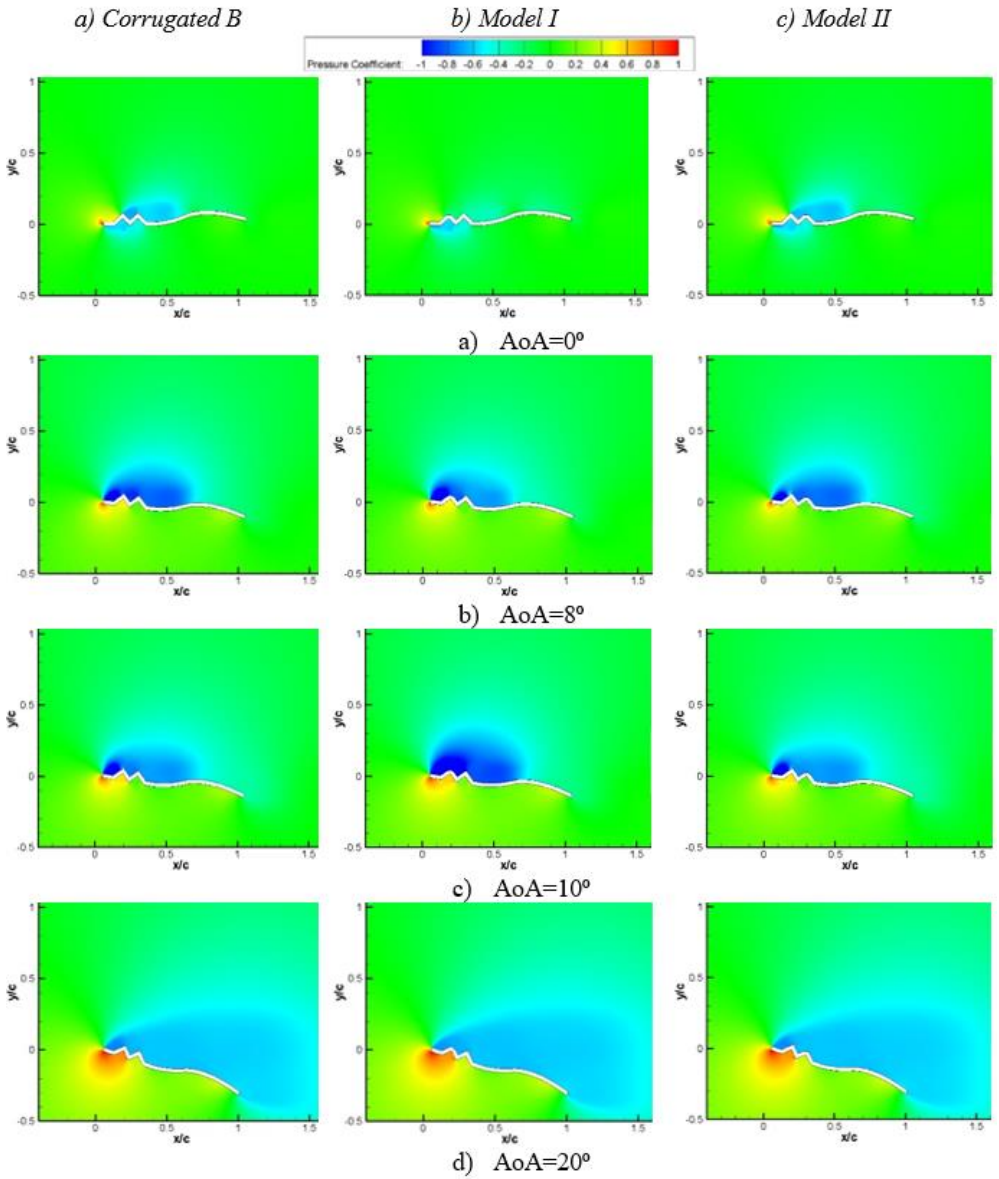


**Figure 6.** Variation of lift-drag ratio of different types of airfoils by changing the angle of attack

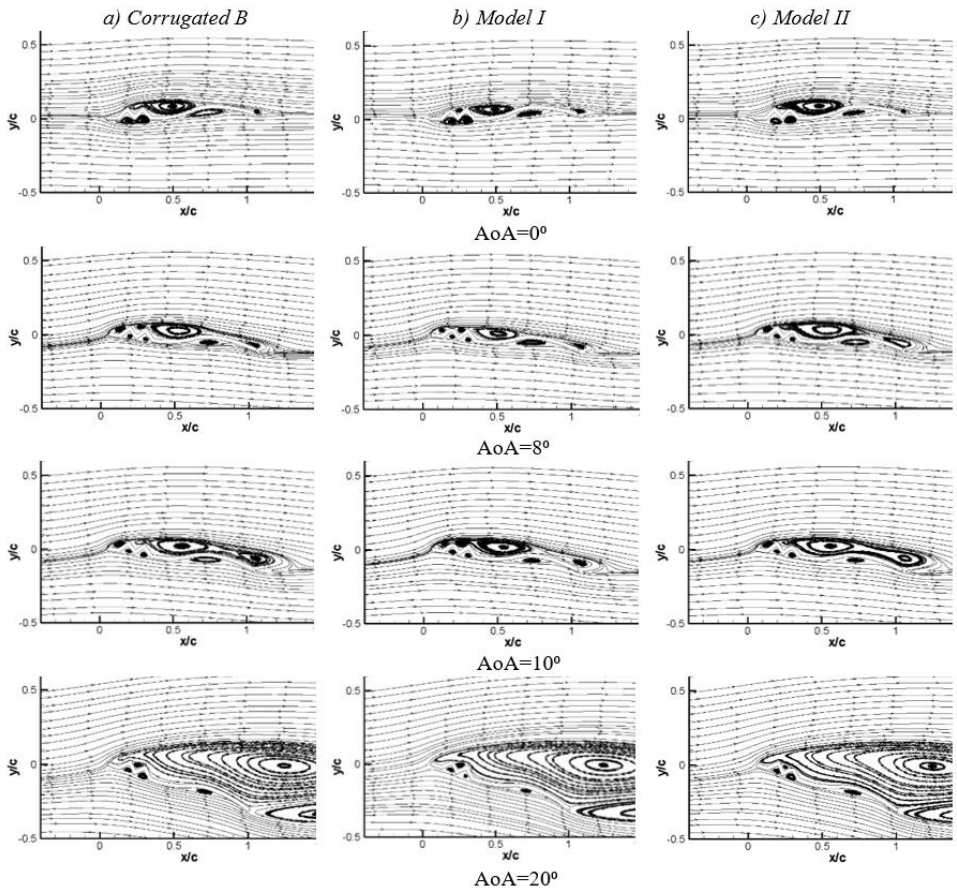




**Figure 7.** Normalized streamwise velocity contours for a) Corrugated B, b) Model I, c) Model II airfoils



**Figure 8.** The contours of pressure distribution around a) Corrugated B, b) Model I, c) Model II airfoils



**Figure 9.** Streamlines plot for a) corrugated B, b) Model I, c) Model II airfoils at various angles of attack

#### 4. CONCLUSION

In this study, the flow characteristics of bio-inspired corrugated airfoils were numerically investigated at a constant Reynolds number of  $1.4 \times 10^4$  using the  $k-\omega$  STT turbulence model. It was obtained that the corrugated B airfoil and the Model II airfoil were similar at  $AoA=0^\circ$  and  $AoA=4^\circ$ , while the Model I airfoil had a lower  $C_L$ . With an increase in the angle of attack from  $AoA=8^\circ$  to  $AoA=10^\circ$ , a decrease in the  $C_L$  of the corrugated B airfoil was noted. In general, at low angles of attack and at angles beyond  $AoA=8^\circ$ , the graph depicting the change in the  $C_L$  coefficient of the corrugated B airfoil and the Model II airfoil with the angle of attack exhibited similar characteristics. It was clearly seen that the Model I airfoil had the highest

$C_L/C_D$  value at  $AoA=8^\circ$ . As mentioned earlier, except for the  $AoA=8^\circ$ , the corrugated B airfoil and the Model II airfoil displayed similar characteristics at other  $AoA$  values. While rounding the second peak of the wing did not contribute to aerodynamic performance, rounding the first peak positively influenced flow characteristics.

By looking at the flow patterns around the airfoils revealed that the lowest angle of attack,  $AoA=0^\circ$ , the flow separated from the first airfoil peak. Furthermore, a trapped vortex became visible in the valley of the Model I airfoil. The recirculation zone in both the corrugated B airfoil and Model II airfoil extended up to the first peak. At  $AoA=8^\circ$  the flow started to separate from the leading edge due to the relatively sharp corners. Separated flows were observed to be trapped within the valley located between the sharp corrugations and the upstream region of the hump, which resulted in the formation of recirculating vortices. After recirculation in the saddle region, the flow was reattached in the hump region, but the trailing edge separation became more pronounced. In the valley section of both the corrugated B airfoil and the Model I airfoil, trapped vortices were apparent. At  $AoA=10^\circ$ , the trailing edge vortices merged with the saddle vortex and extended to the first peak in all three airfoils. At  $AoA=20^\circ$ , the flow became fully separated, and the flow pattern was consistent across all airfoils. In addition, the vortices were trapped at the bottom of the airfoil and were not completely dissipated.

## REFERENCES

- [1]-Sunada, S., Sakaguchi, A., & Kawachi, K. (1997). Airfoil Section Characteristics at a Low Reynolds Number. *Journal of Fluids Engineering*, 119(1), 129-135.
- [2]-Levy, D. E., & Seifert, A. (2010). Parameter study of simplified dragonfly airfoil geometry at Reynolds number of 6000. *Journal of theoretical biology*, 266(4), 691-702.
- [3]- Lissaman, P. B. S. (1983). Low-Reynolds-number airfoils. *Annual review of fluid mechanics*, 15(1), 223-239.
- [4]- Shyy, W., Lian, Y., Tang, J., Viieru, D., & Liu, H. (2008). *Aerodynamics of low Reynolds number flyers*.
- [5]- Pelletier, A., & Mueller, T. J. (2000). Low Reynolds number aerodynamics of low-aspect-ratio, thin/flat/cambered-plate wings. *Journal of aircraft*, 37(5), 825-832.
- [3]- Genç, M. S., Açikel, H. H., Demir, H., Özden, M., Çağdaş, M., & Isabekov, I. (2016). Effect of tip vortices on membrane vibration of flexible wings with different aspect ratios.
- [6]- Genç, M. S., Özden, M., Açikel, H. H., Demir, H., & Isabekov, I. (2016). Unsteady flow over flexible wings at different low Reynolds numbers. In *EPJ Web of Conferences* (Vol. 114, p. 02030). EDP Sciences.
- [7]- Demir, H., & Genç, M. S. (2017). An experimental investigation of laminar separation bubble formation on flexible membrane wing. *European Journal of Mechanics-B/Fluids*, 65, 326-338.
- [8]- Demir, H. (2018). *Investigation of Unsteady Aerodynamics of Flexible Wings at Low Reynolds Numbers* (Doctoral dissertation, PhD. Thesis. Turkey: Erciyes University).
- [9]- Genç, M. S., Demir, H., Özden, M., & Bodur, T. M. (2021). Experimental analysis of fluid-structure interaction in flexible wings at low Reynolds number flows. *Aircraft Engineering and Aerospace Technology*, 93(6), 1060-1075.
- [10]- Ilie, M., & Sullivan, G. (2023). Bio-inspired, low-Reynolds number, aerodynamics of flapping airfoils in tandem; computational studies using LES. In *AIAA SCITECH 2023 Forum* (p. 1026).
- [11]- Aydın, N., Caliskan, M. E., Sabirli, M. U., & Karagoz, I. (2023). An experimental study of the aerodynamic performance of a maple wing model at low Reynolds numbers. *Mechanics Research Communications*, 130, 104104.

- [12]- Gao, H., Hu, H., & Wang, Z. J. (2008, January). Computational study of unsteady flows around dragonfly and smooth airfoils at low Reynolds numbers. In *46th AIAA aerospace sciences meeting and exhibit* (p. 385).
- [13] Murphy, J., & Hu, H. (2009, January). An experimental investigation on a bio-inspired corrugated airfoil. In *47th AIAA aerospace sciences meeting including the new horizons forum and aerospace exposition* (p. 1087).
- [14] Murphy, J. T., & Hu, H. (2010). An experimental study of a bio-inspired corrugated airfoil for micro air vehicle applications. *Experiments in fluids*, 49, 531-546.
- [15] Hord, K., & Liang, Y. (2012). Numerical investigation of the aerodynamic and structural characteristics of a corrugated airfoil. *Journal of Aircraft*, 49(3), 749-757.
- [16] New, T. H., Chan, Y. X., Hoang, M. C., & Koh, G. C. Aerodynamic flow separation control using bio-inspired corrugated wings. Singapore Aerospace Technology and Engineering Conference 2012
- [17] New, T. H., Chan, Y. X., Koh, G. C., Hoang, M. C., & Shi, S. (2014). Effects of corrugated aerofoil surface features on flow-separation control. *AIAA journal*, 52(1), 206-211.
- [18] Ren, H., Wang, X., Li, X., & Chen, Y. (2013). Effects of dragonfly wing structure on the dynamic performances. *Journal of Bionic Engineering*, 10(1), 28-38.
- [19] Sridhar, V., & Dwivedi, Y. K. (2017, December). Effect of peak shape in bio inspired corrugated wing. In *International conference on advances in thermal systems, materials and design engineering (ATSMDE2017)*.
- [20]- Biradar, A., Chandraker, A., Madan, R., Sanyal, S., & Bhowmick, S. (2020). Effect of Attack Angle on Lift and Drag of a Bio-Inspired Corrugated Aerofoil. In *Innovative Product Design and Intelligent Manufacturing Systems: Select Proceedings of ICIPDIMS 2019* (pp. 261-268). Springer Singapore.2
- [21] Shabbir, Z., Shah, H. R., Mansoor, A., Ahmed, A., & Tayyab, S. M. (2020). Effects of Varying Peak Shape on Aerodynamic Performance of a Corrugated Airfoil. In *AIAA Scitech 2020 Forum* (p. 2220).

## CHAPTER 7

### PARAMETERS AFFECTING MICRO ARC OXIDATION PROCESS, BIOCOMPATIBILITY AND PARTICLE ADDITION

Kadir ÜNLÜSES<sup>1</sup>

Prof. Dr. MEHMET ŞİMŞİR<sup>2</sup>

Assoc. Prof. Dr. EBRU YABAŞ<sup>3</sup>

---

<sup>1</sup> Sivas Cumhuriyet University, Faculty of Engineering, Department of Metallurgical and Materials Engineering Sivas, Türkiye. kadirunluses@gmail.com, Orcid ID: 0009-0004-8170-193X

<sup>2</sup> Sivas Cumhuriyet University, Faculty of Engineering, Department of Metallurgical and Materials Engineering Sivas, Türkiye. msimsir@cumhuriyet.edu.tr Orcid ID: 0000-0002-8895-7821

<sup>3</sup> Advanced Technology Application and Research Center, Sivas Cumhuriyet University, Sivas, Türkiye. eyabas@cumhuriyet.edu.tr, Orcid ID: 0000-0001-7163-3057.





## INTRODUCTION

Micro Arc Oxidation (MAO) is used in many areas in the biomedical applications (medicine, dentistry), automotive, military, textile industry, maritime industry, aircraft and space sectors because it creates high temperature resistant coatings and shows high dielectric properties. Due to this feature, it is especially important in the space industry in the production of protective coatings of missiles and space shuttles. In addition, MAO technology is used in chemical applications because it is resistant not only to high temperatures but also to medium temperatures and strong acids and bases; In mechanical applications as a factor that increases wear resistance due to its high oxide hardness ( $> 1300 \text{ kg/mm}^2$ ) layer; It is a surface modification process that can be used in thermal and electrical-electronic applications (Sun et al., 2005, Günyüz, 2007, Mostofizadeh et al., 2011)

Compared to anodic oxidation, MAO technology is superior with its higher coating formation rate and thickness due to the ability to reach higher voltages. MAO technology is a superior process to the plasma spraying method with its high adhesion force that develops with the substrate material. When compared to the hard chrome plating method in terms of the electrolytes used, it is seen that the alkaline electrolytes used in the MAO process are not harmful to the environment. In short, the MAO process is seen as a technology that continues to develop, provides high tribological properties, and will replace many of the traditional coatings with its advanced surface treatment method (Lee et al., 2008, Morks et al., 2011, Malayoglu et al., 2011).

An ideal metallic biomaterial used in dentistry and orthopedic fields; It is required to have biocompatibility, relatively low density, contain little or no toxic metals in its structure, have high strength and long fatigue life, low elastic modulus (compared to cortical bone), plasticity at wide ambient temperatures and be perfect. Titanium and its alloys are shiny and have a high specific strength (strength/density) ratio. Titanium and its alloys are widely used in dental and orthopedic applications due to their excellent biocompatibility, mechanical properties, excellent corrosion resistance and ease of machinability (Rautray et al., 2011). Biocompatibility is the ability of a material to perform its function in the presence of the appropriate environment for a specific application. The materials used as implants are expected to be highly non-toxic and should not cause any inflammation or

allergic reactions in the human body (Geetha et al., 2009). The success of biomaterials depends mainly on the reaction of the living body towards the implant material. Due to the presence of a passive and stable thin oxide film ( $\text{TiO}_2$ ) formed on the surface of titanium, it is relatively inert, has high corrosion resistance and superior biocompatibility. Since the oxide layer on the titanium surface is homogeneous and dense, the titanium implant does not interact with tissues and also regenerates immediately if the passive layer is damaged (Liu, et al., 2004).

The surfaces of titanium and its alloys play an important role in implant integration in the living body. As a result of different surface modifications, the properties specified in the following items can be achieved.

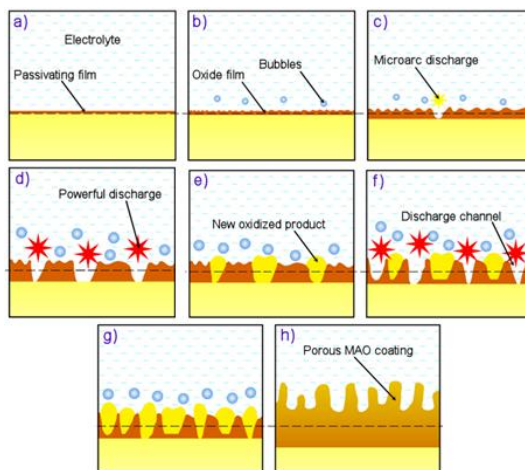
- Better mechanical fixation of the implant to the bone tissue (improvement of bone bonding with the implant)
- Improvement of bone permeability and inductivity
- Improving wear resistance
- Improving corrosion resistance
- Improvement of biocompatibility and bioactivity
- Shortening recovery time after implantation

In this article, the parameters of the micro arc oxidation process and biocompatibility are examined.

## **1. MAO PROCESS AND BASIC FEATURES**

The basic principle of MAO is explained in Figure 1. In the initial stage of the MAO process, as soon as the sample is exposed to the electrolyte, the voltage increases rapidly and linearly with time, and an anodic barrier film (Figure 1a), also called the passivating film, is initially formed on the surface of the sample. After a short time, with the increase of voltage, some small oxygen bubbles can be observed, and a porous insulating oxide layer is formed on the surface of the sample, which usually grows under dielectric breakdown conditions. In this stage, voltage and current flow follow Faraday's law, corresponding to the conventional anodization stage (Figure 1b). When the voltage applied on the sample exceeds the dielectric breakdown dielectric breakdown occurs, leading to the formation of spark discharges (Figure 1c). The current flow concentrates only on the fragmentation zones, and elements from the electrolyte and other elements from the sample enter the fragmentation regions by diffusion and electrophoresis at intense local high

temperatures, causing local formation and thickening of the porous oxide structure. The discharge sparks gradually grow larger, and the discharges of micro-arcs turn into strong arc discharges (Fig. 1d). Once the newly produced oxide coating (Fig. 1e) is capable of resisting current flow, other regions are vulnerable to breakage due to smaller resistance, and finally, the chemical reaction interface will move towards the entire surface. Deterioration of the coating occurs at a sensitive point in the growing oxide film. Meanwhile, the new porous structure oxide coating can also be formed and thickened by gas emission due to intense local high temperatures in the discharge regions. With the prolongation of oxidation time, large discharge channels with dense sparks and gas bubbles will appear on the surface, leading to the formation of larger pores or even a spongy interconnected microstructure (Figure 1f). The continuous formation and breakdown of the oxide coating (Figure 1g) causes the potential fluctuation. Both the dissolution of the base material and the gasification of the electrolyte enable the formation of a porous ceramic oxide coating (Figure 1h)



**Figure 1:** Schematic of the formation process of MAO porous coating. Initially, a passivating film (a) and a porous insulating oxide film (b) are formed. Then, under the influence of spark discharges (c) and strong arc discharges (d), the newly produced oxide coating (e) is formed and thickens. Finally, with the degradation and continuous formation of the (f) oxide layer on the large discharge channels (g), a ceramic porous layer is formed (h). (He et al., 2017).

By examining the physical and chemical foundations of MAO, Snizko concluded that the process consists of four different steps (Snizhko et al., 2004). These steps are given in Figure 2.

STAGE 1- The voltage increases rapidly and linearly over time until the breakdown voltage. Some small oxygen bubbles and an oxide layer can be observed on the sample surface, corresponding to the conventional anodizing step. STAGE 2- When the applied voltage exceeds a certain critical value, dielectric breakdown occurs, resulting in spark discharges. At this stage, current flow is concentrated only in the degradation regions, leading to localized thickening of the oxide coating. The newly formed coating can restore resistance to current flow while other areas where the resistance is small are more prone to breakage. At this stage, simultaneously with a high-pitched sound, the number of small white sparks are randomly distributed and move rapidly over the entire anode surface. STAGE 3- The continuous formation and disintegration of the oxide film causes the cell potential to fluctuate. Gasification of both valve metals and electrolyte allows direct formation of the ceramic oxide coating. Deterioration of the coating occurs at a sensitive point in the growing oxide film. With increasing processing time, the discharge sparks become larger and their color changes from white to orange or red. In this region, micro-arcs turn into strong arcs. STAGE 4- Intense sparking and gas release trigger the formation of large-sized pores and thermal cracking of the film. With the disappearance of sparks and gas bubbles, the voltage drops rapidly, indicating the end of the MAO process. MAO coating is a two-layer morphology: a barrier inner layer and a porous outer layer with numerous thin and ordered cavities (Li et al. 2014).



**Figure 2:** Steps of the MAO process (Snizhko et al., 2004).

## 2. PARAMETERS AFFECTING THE PROPERTIES OF MAO COATING

It was found that the properties of the MAO coating are depends on many parameters. However, some of these parameters have briefly explained below.

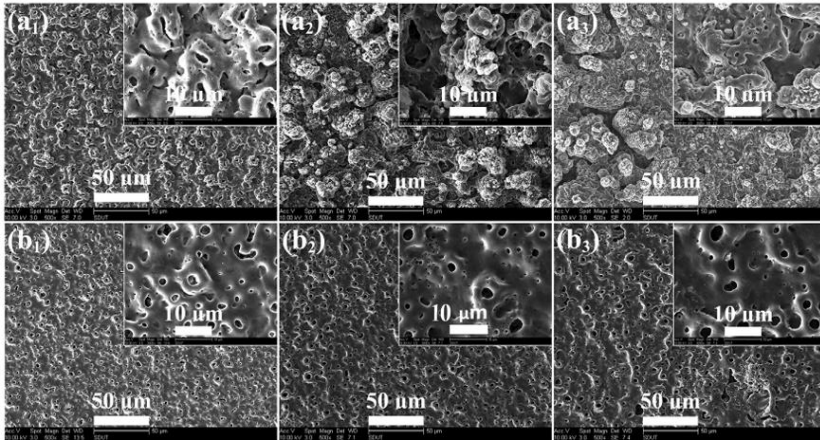
### 2.1. Type of electrolytic

The concentration and composition of electrolytes significantly affect the morphological properties, porosity, thickness, corrosion resistance and biocompatibility of MAO coatings. Therefore, it is imperative to choose the electrolyte composition and concentration correctly so that metal passivation can occur quickly and the spark voltage can be easily reached (Ellingsen, J. E., 1995) Generally, NaOH/KOH is used as the base in the electrolyte, and phosphate Surface characteristics and biological (Seyfoori et al., 2012), flüoride (Ellingsen, J. E., 1995) (Venkateswarlu et al., 2013) and silicate (Seyfoori et al., 2012) (Liang et al., 2007) are used as primary electrolyte additives in the MAO process.

Venkateswarlu et al., (2012) in their study methodically used 7 different electrolyte systems consisting of tri-sodium ortho phosphate ( $\text{Na}_3\text{PO}_4 \cdot 12\text{H}_2\text{O}$ -TSOP), sodium meta silicate ( $\text{Na}_2\text{SiO}_3 \cdot 9\text{H}_2\text{O}$ -SMS) and potassium hydroxide (KOH) in varying concentrations. Phase composition, surface morphology and coating thickness were examined. The coating process was carried out for 12 min at a constant current of 0.75 A, corresponding to a current density of approximately  $100 \text{ mA/cm}^2$  in the workpiece. As a result of the studies, the thickness of the oxide coatings developed on Ti-6Al-4V by the MAO process increased with the increase of the TSOP concentration in the electrolyte solution. When comparing electrolyte systems with the same TSOP and KOH content, the addition of the SMS additive contributes to a further increase in thickness and the conversion of anatase to the rutile phase.

Wang et al., (2020) applied micro arc oxidation process to Ti6Al4V alloy in two different electrolytes. The effects of electrolyte composition and applied positive voltage on the microstructure and corrosion resistance of the MAO coating were investigated. In this study, sodium silicate ( $\text{Na}_2\text{SiO}_3 \cdot 9\text{H}_2\text{O}$ ) and calcium glycerol phosphate ( $\text{C}_3\text{H}_7\text{CaO}_6\text{P}$ ) were used as the main ingredients of MAO electrolytes to modify Ti6Al4V alloys,

respectively. The effects of silicate and calcium phosphate on the microstructure and corrosion behavior of micro arc oxidized coatings on biomedical Ti6Al4V alloys were investigated. Two electrolytes were prepared from a solution containing ( $\text{NaPO}_3$ ),  $\text{NaF}$ ,  $\text{KOH}$  and  $\text{C}_3\text{H}_8\text{O}_3$ . Sodium silicate ( $\text{Na}_2\text{SiO}_3 \cdot 9\text{H}_2\text{O}$ ) and calcium glycerol phosphate ( $\text{C}_3\text{H}_7\text{CaO}_6\text{P}$ ) were added to these two electrolytes, respectively. The coating surface images are indicated in the Figure 3.



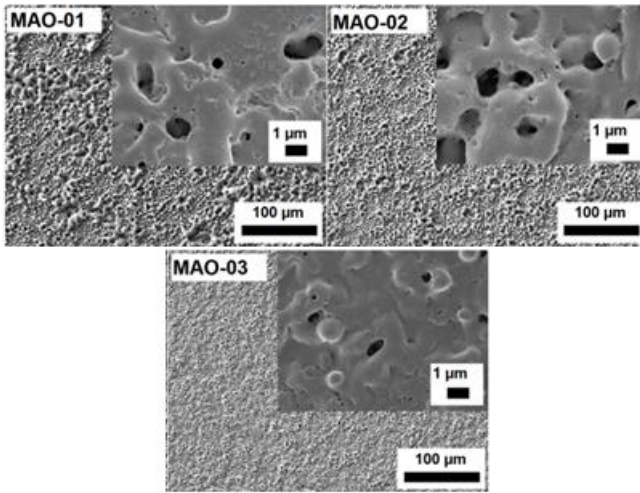
**Figure 3:** SEM images of samples coated with MAO (the samples corresponding to electrolyte solutions containing  $\text{Na}_2\text{SiO}_3 \cdot 9\text{H}_2\text{O}$  and  $\text{C}_3\text{H}_7\text{CaO}_6\text{P}$  were named A and B, respectively. The applied positive voltages for these three samples processed in electrolyte A and B were 400, 425 and 450 V, and The samples were named  $\text{A}_1/\text{B}_1$ ,  $\text{A}_2/\text{B}_2$  and  $\text{A}_3/\text{B}_3$ , respectively (Wang et al., 2020).

As a result of the studies, MAO coatings obtained from calcium phosphate electrolyte have a smooth surface, homogeneous micropores and stable roughness despite the positive voltage change. The roughness of coatings obtained from silicate electrolyte has changed greatly.

## 2.2. Applied voltage

One of the most important electrical parameters affecting the coating characteristics in MAO processes with Ti and its alloys is voltage.

Gabor et al.. (2021) applied MAO treatment to Ti6Al4V alloy using an alkaline electrolyte containing  $\text{Na}_2\text{SiO}_3 \cdot 9\text{H}_2\text{O}$  and  $\text{NaOH}$ . MAO operation was carried out with fixed duty cycle, constant frequency and variable voltage 350V (MAO-01), 400V (MAO-02), 450V (MAO-03) parameters. SEM images after MAO treatment are shown in the figure 4.



**Figure 4:** Surface morphologies of MAO coatings (Gabor et al., 2021).

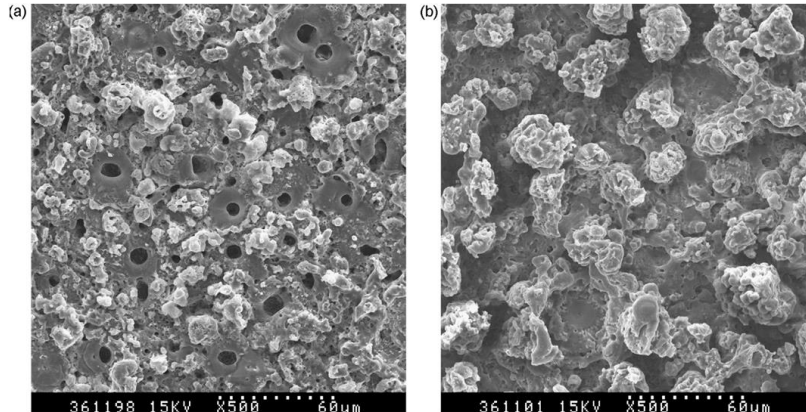
As a result of the studies, surface roughness and coating thickness increased with the increase in voltage value. At the same time, different voltage values also affect the morphology of the coating, ion distribution, the presence and size of pores, and wear resistance.

### 2.3. Duty cycle

Duty cycle (D) is defined as the ratio of on time to overall time (on time + off time). The higher the duty cycle, the longer the operating time in one cycle and the greater the energy discharged in a pulse (Dehnavi et al., 2013). Increase in duty cycle is equivalent to an increase in the duration of current/voltage applied during each cycle. Duty cycle has a similar effect to applied voltage on the properties of MAO coatings. There is a positive relationship between the duty cycle and the energy density of the sparks, released thermal energy and the amount of molten oxide. Increasing the duty cycle increases the porosity and slightly reduces the coating thickness (Tang et al., 2010). When the duty cycle is slower than 0.4, the thickness of the anodic coating is too thin to effectively protect the substrate. When the duty cycle is higher than 0.6, the porosity of the anodic coating is very high, corrosion resistance decreases. The same, lower variable duty cycle ratio has higher microhardness with a more uniform microhardness profile. However, the effect of duty cycle is evident at relatively low voltage.

Yao et al., (2007) showed that duty cycle plays an important role in coating properties and coating growth. MAO treatment was applied to

Ti6Al4V alloy in a solution containing  $\text{NaAlO}_2$  and  $\text{Na}_3\text{PO}_4$  and different duty cycles were selected. SEM images of the obtained samples are shown in the Figure 5.



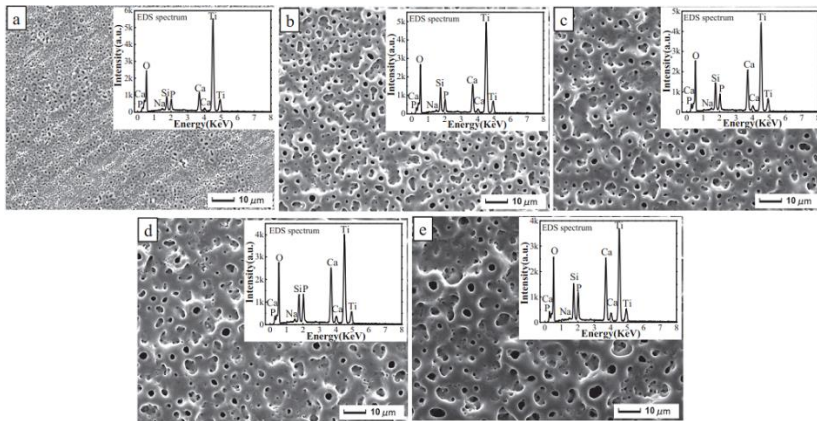
**Figure 5:** Surface SEM figures of coatings prepared under different duty ratios (a)D=10% and (b)D=45%. Yao et al., (2007)

As a result of the studies, as duty time increased, the coating thickness and roughness also increased. Changes in duty ratio led to a change in the mode of spark discharge, which further affected the structure and morphology of ceramic coatings. Ceramic coating increased the corrosion resistance of Ti-6Al-4V alloy. And the surface morphology and coating thickness determined that the corrosion resistance of coated samples prepared at D=45% was better than that of coated samples prepared at D=10%.

#### 2.4. Process time

The effect of processing time is also an important parameter affecting the characterization of MAO coatings deposited on Ti/Ti alloys. Xu et al., (2018) used a solution containing calcium acetate monohydrate ( $(\text{CH}_3\text{COO})_2\text{Ca}\cdot\text{H}_2\text{O}$ , AR), sodium silicate ( $\text{Na}_2\text{SiO}_3\cdot 9\text{H}_2\text{O}$ , AR) and sodium tripolyphosphate ( $\text{Na}_5\text{P}_3\text{O}_{10}$ , AR) as electrolyte. MAO process was carried out using pure Ti. Current density, frequency and duty cycle were kept constant and the processing time was set as 3, 6, 9, 12 and 15 minutes. SEM micrographs of MAO coatings on Ti prepared with different oxidation times are presented in Figure 5 (a–e).





**Figure 5:** Surface SEM images and EDS spectra of coatings prepared with different oxidation times: (a) 3 min; (b) 6 minutes; (c) 9 minutes; (d) 12 minutes; (e) 15 minutes. Xu et al., (2018)

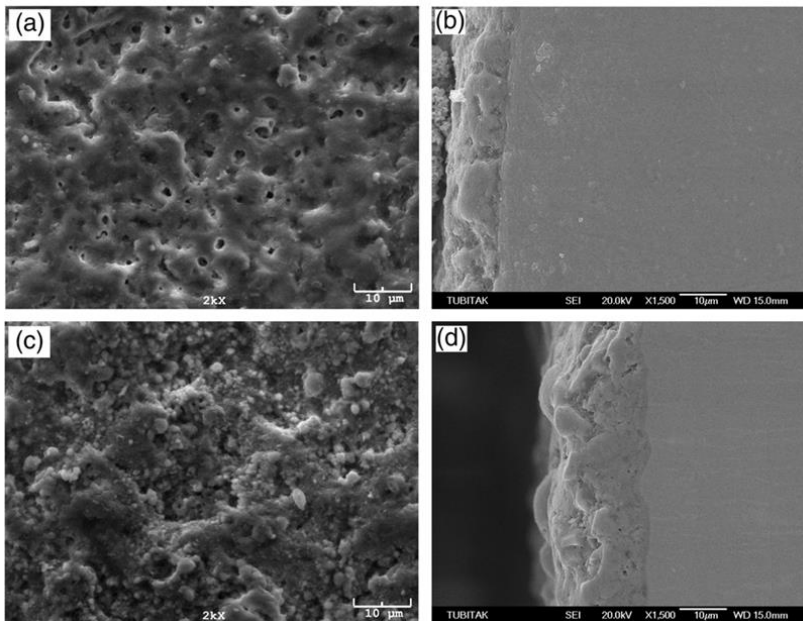
As a result of the studies, oxidation time has a significant effect on the surface microstructure of modified coatings. In the early stages of MAO, a large number of micropores were evenly distributed on the coating surface. With the increase of oxidation time, the number of micropores decreased, while the size of micropores and the roughness of the coatings increased significantly.

### 3. BIOCOMPATIBILITY OF Ti ALLOYS

The increasing use of titanium and its alloys as biomaterials is due to superior biocompatibility and excellent corrosion resistance due to the thin surface oxide layer and good mechanical properties such as a certain elastic modulus and low density which enable these metals to exhibit a mechanical behavior close to that of bones. Lightweight, strong and completely biocompatible, titanium is one of the few materials that naturally meets the requirements for implantation into the human body. Among all titanium and its alloys, the main materials used in the biomedical field are commercially pure titanium (cp Ti, grade 2) and Ti-6Al-4V (grade 5) alloy. These are widely used as hard tissue substitutes in artificial bones, joints and dental implants. As hard tissue substitutes, the low elastic modulus of titanium and its alloys is often viewed as a biomechanical advantage because the smaller elastic modulus can result in smaller stress shielding (de Viteri and Fuentes, 2013).

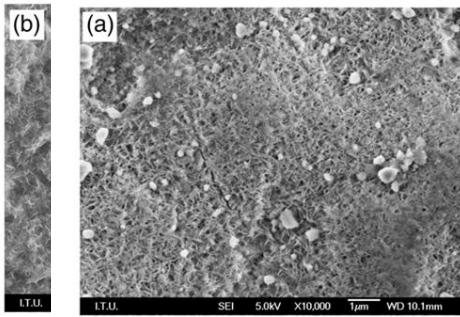
Titanium and its alloys are the most promising biomaterials for implants because titanium-based materials generally rely on the formation of an extremely thin, adherent, protective titanium oxide film. The presence of this oxide film, which forms spontaneously during the passivation or repassivation process, is an important criterion for the excellent biocompatibility and corrosion resistance of titanium and its alloys.

In the study conducted by Cimenoglu et al., (2011) Ti6Al4V and Ti6Al7Nb alloys were examined after their surfaces were changed by micro arc oxidation (MAO) process using electrolyte containing  $(\text{CH}_3\text{COO})_2\text{Ca}\cdot\text{H}_2\text{O}$  and  $\text{Na}_3\text{PO}_4$ . SEM images of the coated surfaces after MAO are shown in the Figure 6.



**Figure 6:** SEM images after the MAO process.(a)Ti6Al4V surface, (b) Ti6Al4V crosssection, (c) Ti6Al7Nb surface and (d) Ti6Al7Nb crosssection. (Cimenoglu et al., 2011)

After MAO treatment, the samples were kept in SBF and the changes on the surface were examined and shown in the Figure 7.



**Figure 7:** After SBF test SEM images of oxidized (a) Ti6Al4V and (b)Ti6Al7Nb alloys. (Cimenoglu et al., 2011)

As a result of the studies, the application of the MAO process had a very beneficial effect on the biocompatibility of Ti6Al4V and Ti6Al7N balls, as a result of the formation of thick, rough surface oxide layers containing calcium and phosphorus. Oxide layer of Ti6Al4V alloy is porous and contains hydroxyapatite. Ti6Al7Nb alloy consists of calcium titanate containing a granular oxide layer. Although oxidized alloys exhibited similar bioactivity during SBF tests, the biocompatibility of the Ti6Al4V alloy was greater than that of the Ti6Al7Nb alloy.

## 4. PARTICLE ADDITION

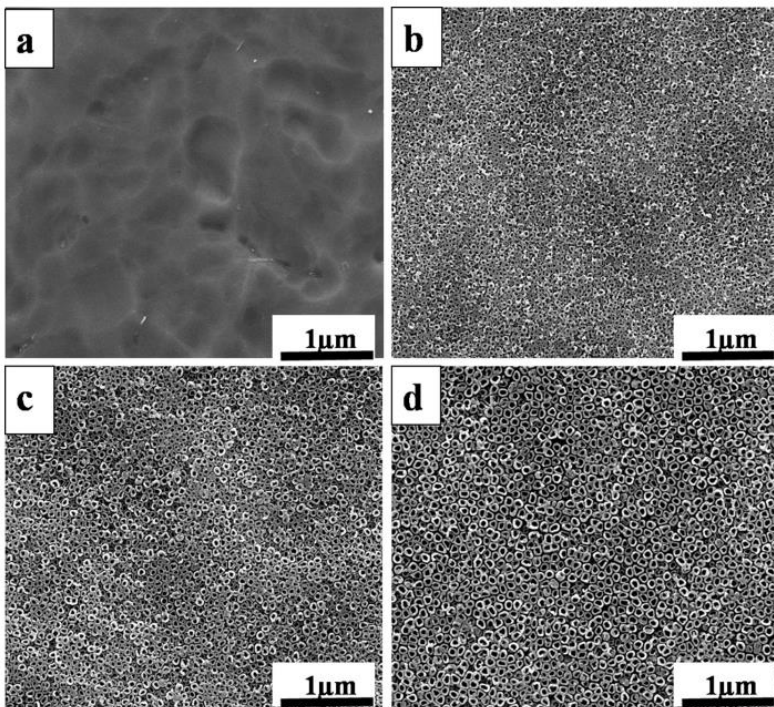
### 4.1. AgNp

Silver particles tend to have a profound effect on the bacteria even at minimum concentrations (Lansdown, 2006). Silver microfine particles with a diameter of less than 20 nm and increased solubility and ion release are recommended for wound healing. Thanks to advances in nanotechnology, synthesis has made silver particles valuable and has made it effective (Rai et al., 2009) . Silver nanoparticles (AgNPs) are used primarily in dentistry for their antimicrobial properties (Zhang et al., 2016).

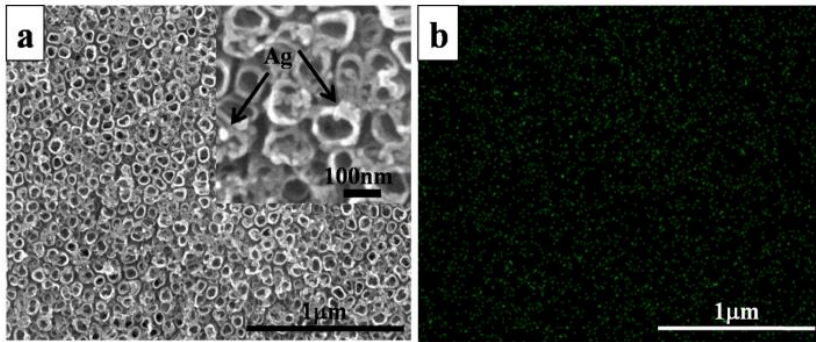
The activity of AgNP depends on many factors such as surface chemistry, morphology, particle size, cell type, among others (Carlson et al., 2008). The size of AgNPs generally ranges from 1 nm to 20 nm (Morones et al., 2005). Particles commonly used in dentistry are smaller than 10 nm, which has maximum bactericidal and bacteriostatic properties. Ion release and antimicrobial activity are further increased when using thinner AgNPs with a size of 10 nm. Due to their small size, the surface area is utilized and more

passage is provided to the cell membranes. Contributes to increased antimicrobial effect (Eckhardt et al., 2013, Yin et al., 2020).

In the study conducted by Zhao et al., (2013), Cp-Ti material was subjected to anodization in a solution containing  $H_3PO_4$  and HF. Titanium nanotubes (TNTs) with diameters of 50, 75 and 100nm (TNTs-50-Ag, TNTs75-Ag and TNTs-100-Ag) were formed on the surface using different voltages. After anodizing, the sample was immersed in  $AgNO_3$  solution. Silver nanoparticles (AgNp) were formed on the sample surface with the help of UV rays. It is shown in the Figure 8. The Figure 9 shows SEM and EDS images of TNTs-100-Ag. Additionally, the antibacterial properties of the produced samples were investigated.



**Figure 8:** SEM images of pure Ti (a), TNT-50 (b), TNTs-75 (c) and TNTs-100 (d). (Zhao et al., 2013)



**Figure 9:** SEM images of TNTs-100-Ag (a-surface) and EDS (b-map scanning) (Zhao et al., 2013)

As a result of the studies, uniformly dispersed Ag nanoparticles, approximately 10 nm in size, were well incorporated into TNTs with the help of UV. All samples showed good antibacterial properties. The TNTs-100-Ag sample had the best antibacterial performance among all these samples, reaching 82.5% against *E. coli* and 82.9% against *S. aureus*.

#### 4.2. Hydroxyapatite

To overcome these surface-related problems, a variety of surface modifications are available for metallic materials, including chemical, physical, and biological techniques (Mozafari et al., 2016, Mehran et al., 2018). Over the past decade, researchers have increasingly focused on modifying the surface properties of biomaterials. It promotes bone healing during the early implantation period. In general, the surfaces of metallic implants interact with the physiological environment of the host, and therefore the surface properties of these implants directly affect their osseoconductive and osseointegration properties (Le Guéhennec et al., 2007, Wang et al., 2015).

Hydroxyapatite (HAp) is generally considered a bioactive coating material that improves the assimilation of bone tissue and implant material (Anselme, 2011). HAp consists of calcium phosphate (Ca-P) and has the chemical structure  $\text{Ca}_{10}(\text{PO}_4)_6(\text{OH})_2$ ; It is the main chemical component of bone tissue (over 70% by weight). Ca-P formation creates a strong chemical bond between implants and surrounding bone tissues (Reis & Weiner, 2005).

The precipitation of Ca-P on the implant surface accelerates the fixation of the implant material to the bone, which increases bone conduction

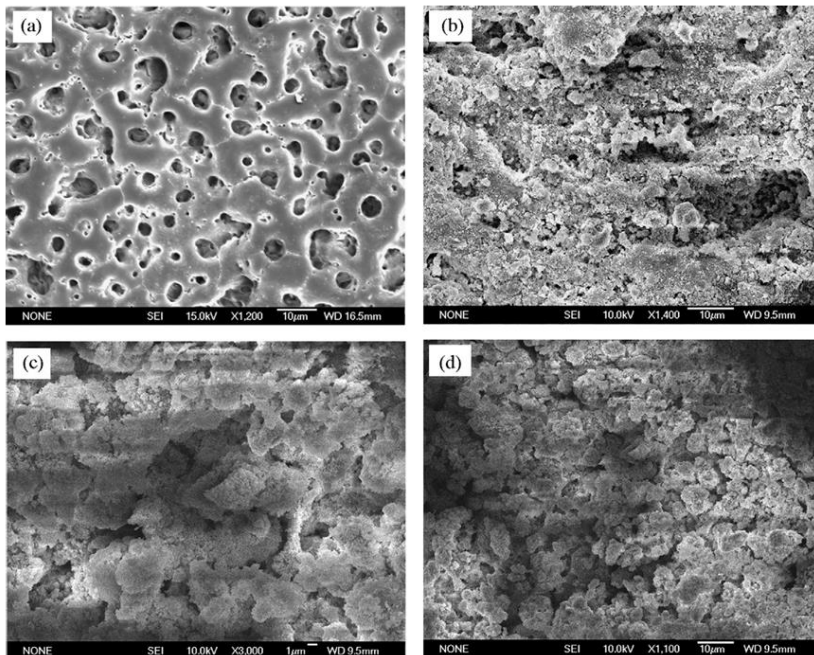
(Kobayashi et al., 2007). Minimum prerequisites for HA coatings are listed in the ISO standards in the US Food and Drug Administration guidelines (Table 1).

**Table 1:** HA coating requirements (Qadir et al., 2018).

Properties Specification	Thickness Not specific	Crystallinity 62% minimum	Phase Purity 95% minimum	Ca/P ratio 1.67-1.76	Density 2.98 g/cm <sup>3</sup>
	Heavy metals <50 ppm	Tensile strength >50.8 MPa	Shear Strength >22 MPa	Abrasion not specific	

Various methods have been used to produce Ca-P coatings on implant surfaces, and one of them is the MAO process.

Ti6Al4V alloy was chosen in the study conducted by Yang et al., (2009). An electrolyte containing calcium and phosphorus was used for the MAO process. MAO treatment was carried out for 10, 15, 20, 25 and 30 minutes. SEM images of the applied MAO processes are shown in the Figure 10.



**Figure 3:** SEM of MAO coatings (a) 10 min (b) 15 min (c) 20 min (d) 25 min. (Yang et al., 2009)

As a result of the studies, bioactive HAp was synthesized on the surface of titanium alloy using the micro arc oxidation technique of the solution containing calcium and phosphorus ions. When the processing time exceeded 20 minutes, the HAp structure also increased and turned into an amorphous phase. MAO time and electric current density play an important role in the formation of phases of ceramic films. The increase of MAO duration and electric current intensity is beneficial for the formation of bioactive HAp in ceramic films on titanium alloy surfaces.

## REFERENCES

- Anselme, K. (2011). Biomaterials and interface with bone. *Osteoporosis International*, 22(6), 2037–2042. <https://doi.org/10.1007/s00198-011-1618-x>
- Carlson, C., Hussein, S. M., Schrand, A. M., Braydich-Stolle, L. K., Hess, K. L., Jones, R. L., & Schlager, J. J. (2008). Unique cellular interaction of silver nanoparticles: Size-dependent generation of reactive oxygen species. *Journal of Physical Chemistry B*, 112(43), 13608–13619. <https://doi.org/10.1021/jp712087m>
- Cimenoglu, H., Gunyuz, M., Kose, G. T., Baydogan, M., Uğurlu, F., & Sener, C. (2011). Micro-arc oxidation of Ti6Al4V and Ti6Al7Nb alloys for biomedical applications. *Materials Characterization*, 62(3), 304–311. <https://doi.org/10.1016/j.matchar.2011.01.002>
- de Viteri, V. S., & Fuentes, E. (2013). Titanium and Titanium Alloys as Biomaterials. In *Tribology - Fundamentals and Advancements*. InTech. <https://doi.org/10.5772/55860>
- Dehnavi, V., Luan, B. L., Shoesmith, D. W., Liu, X. Y., & Rohani, S. (2013). Effect of duty cycle and applied current frequency on plasma electrolytic oxidation (PEO) coating growth behavior. *Surface and Coatings Technology*, 226, 100–107. <https://doi.org/10.1016/j.surfcoat.2013.03.041>
- Eckhardt, S., Brunetto, P. S., Gagnon, J., Priebe, M., Giese, B., & Fromm, K. M. (2013). Nanobio silver: Its interactions with peptides and bacteria, and its uses in medicine. In *Chemical Reviews* (Vol. 113, Issue 7, pp. 4708–4754). <https://doi.org/10.1021/cr300288v>
- Ellingsen, J. E. (1995). *Pre-treatment of titanium implants with fluoride improves their retention in bone*. *J.Mater.sci.* 6, 749–753
- Gabor, R., Cvrček, L., Causidu, S., Drobnikova, K., Večeř, M., Kutlákova, K. M., Buřil, M., Hlinka, J., & Seidlerová, J. (2021). Effect of additive for preparation of reduced-porosity ceramic layer on Ti-6Al-4 V alloy for orthopaedic and trauma implants. *Surfaces and Interfaces*, 25. <https://doi.org/10.1016/j.surfin.2021.101209>
- Geetha, M., Singh, A. K., Asokamani, R., & Gogia, A. K. (2009). Ti based biomaterials, the ultimate choice for orthopaedic implants - A review. In *Progress in Materials Science* (Vol. 54, Issue 3, pp. 397–425). <https://doi.org/10.1016/j.pmatsci.2008.06.004>



- Günyüz, M. (2007). Titanium ve Alaşımalarının Mikro Ark Oksidasyon İşlemi ile Kaplanması. Yüksek Lisans Tezi, İ.T.Ü. Fen Bilimleri Enstitüsü, İstanbul, Türkiye.
- He, X., Zhang, X., Wang, X., & Qin, L. (2017). Review of Antibacterial Activity of Titanium-Based Implants' Surfaces Fabricated by Micro-Arc Oxidation. *Coatings*, 7(3), 45. <https://doi.org/10.3390/coatings7030045>
- Jung, Y. C., Shin, K. R., Ko, Y. G., & Shin, D. H. (2014). Surface characteristics and biological response of titanium oxide layer formed via micro-arc oxidation in K<sub>3</sub>PO<sub>4</sub> and Na<sub>3</sub>PO<sub>4</sub> electrolytes. *Journal of Alloys and Compounds*, 586(SUPPL. 1). <https://doi.org/10.1016/j.jallcom.2013.01.060>
- Kobayashi, E., Ando, M., Tsutsumi, Y., Doi, H., Yoneyama, T., Kobayashi, M., & Hanawa, T. (2007). Inhibition effect of zirconium coating on calcium phosphate precipitation of titanium to avoid assimilation with bone. *Materials Transactions*, 48(3), 301–306. <https://doi.org/10.2320/matertrans.48.301>
- Lansdown, A. B. G. (2006). Silver in Health Care: Antimicrobial Effects and Safety in Use. In *Curr Probl Dermatol. Basel, Karger* (Vol. 33).
- le Guéhennec, L., Soueidan, A., Layrolle, P., & Amouriq, Y. (2007). Surface treatments of titanium dental implants for rapid osseointegration. In *Dental Materials* (Vol. 23, Issue 7, pp. 844–854). <https://doi.org/10.1016/j.dental.2006.06.025>
- Lee, J. M., Kang, S. B., & Han, J. (2008). Dry sliding wear of MAO-coated A356/20 vol.% SiCp composites in the temperature range 25-180 °C. *Wear*, 264(1–2), 75–85. <https://doi.org/10.1016/j.wear.2007.01.044>
- Li, L. H., Sankara Narayanan, T. S. N., Kim, Y. K., Kong, Y. M., Park, I. S., Bae, T. S., & Lee, M. H. (2014). Deposition of microarc oxidation-polycaprolactone duplex coating to improve the corrosion resistance of magnesium for biodegradable implants. *Thin Solid Films*, 562, 561–567. <https://doi.org/10.1016/j.tsf.2014.04.004>
- Liang, J., Hu, L., & Hao, J. (2007). Characterization of microarc oxidation coatings formed on AM60B magnesium alloy in silicate and phosphate electrolytes. *Applied Surface Science*, 253(10), 4490–4496. <https://doi.org/10.1016/j.apsusc.2006.09.064>
- Liu, X., Chu, P. K., & Ding, C. (2004). Surface modification of titanium, titanium alloys, and related materials for biomedical applications. In

- Materials Science and Engineering R: Reports* (Vol. 47, Issues 3–4, pp. 49–121). <https://doi.org/10.1016/j.mser.2004.11.001>
- Malayoglu, U., Tekin, K. C., Malayoglu, U., & Shrestha, S. (2011). An investigation into the mechanical and tribological properties of plasma electrolytic oxidation and hard-anodized coatings on 6082 aluminum alloy. *Materials Science and Engineering: A*, 528(24), 7451–7460. <https://doi.org/10.1016/j.msea.2011.06.032>
- Mehran, Q. M., Fazal, M. A., Bushroa, A. R., & Rubaiee, S. (2018). A Critical Review on Physical Vapor Deposition Coatings Applied on Different Engine Components. In *Critical Reviews in Solid State and Materials Sciences* (Vol. 43, Issue 2, pp. 158–175). Taylor and Francis Inc. <https://doi.org/10.1080/10408436.2017.1320648>
- MORKS, Magdi. F., COLE, I., Corrigan, P., & KOBAYASHI, A. (2011). Electrochemical Characterization of Plasma Sprayed Alumina Coatings. *Journal of Surface Engineered Materials and Advanced Technology*, 01(03), 107–111. <https://doi.org/10.4236/jsemat.2011.13016>
- Morones, J. R., Elechiguerra, J. L., Camacho, A., Holt, K., Kouri, J. B., Ramírez, J. T., & Yacaman, M. J. (2005). The bactericidal effect of silver nanoparticles. *Nanotechnology*, 16(10), 2346–2353. <https://doi.org/10.1088/0957-4484/16/10/059>
- Mostofizadeh, A., Li, Y., Song, B., & Huang, Y. (2011). Synthesis, properties, and applications of low-dimensional carbon-related nanomaterials. In *Journal of Nanomaterials* (Vol. 2011). <https://doi.org/10.1155/2011/685081>
- Mozafari, M., Ramedani, A., Zhang, Y. N., & Mills, D. K. (2016). Thin films for tissue engineering applications. In *Thin Film Coatings for Biomaterials and Biomedical Applications* (pp. 167–195). Elsevier. <https://doi.org/10.1016/B978-1-78242-453-6.00008-0>
- Rai, M., Yadav, A., & Gade, A. (2009). Silver nanoparticles as a new generation of antimicrobials. In *Biotechnology Advances* (Vol. 27, Issue 1, pp. 76–83). <https://doi.org/10.1016/j.biotechadv.2008.09.002>
- Rautray, T. R., Narayanan, R., & Kim, K. H. (2011). Ion implantation of titanium based biomaterials. In *Progress in Materials Science* (Vol. 56, Issue 8, pp. 1137–1177). Elsevier Ltd. <https://doi.org/10.1016/j.pmatsci.2011.03.002>

- Reis, R.L., & Weiner, S. (2005). Learning from nature how to design new implantable biomaterials : from biomineralization fundamentals to biomimetic materials and processing routes.
- Seyfoori, A., Mirdamadi, S., Khavandi, A., & Raufi, Z. S. (2012). Biodegradation behavior of micro-arc oxidized AZ31 magnesium alloys formed in two different electrolytes. *Applied Surface Science*, 261, 92–100. <https://doi.org/10.1016/j.apsusc.2012.07.105>
- Snizhko, L. O., Yerokhin, A. L., Pilkington, A., Gurevina, N. L., Misnyankin, D. O., Leyland, A., & Matthews, A. (2004). Anodic processes in plasma electrolytic oxidation of aluminium in alkaline solutions. *Electrochimica Acta*, 49(13), 2085–2095. <https://doi.org/10.1016/j.electacta.2003.11.027>
- Sun, X., Jiang, Z., Xin, S., & Yao, Z. (2005). Composition and mechanical properties of hard ceramic coating containing  $\alpha$ -Al<sub>2</sub>O<sub>3</sub> produced by microarc oxidation on Ti-6Al-4V alloy. *Thin Solid Films*, 471(1–2), 194–199. <https://doi.org/10.1016/j.tsf.2004.06.096>
- Tang, Y., Zhao, X., Jiang, K., Chen, J., & Zuo, Y. (2010). The influences of duty cycle on the bonding strength of AZ31B magnesium alloy by microarc oxidation treatment. *Surface and Coatings Technology*, 205(6), 1789–1792. <https://doi.org/10.1016/j.surfcoat.2010.05.016>
- Venkateswarlu, K., Rameshbabu, N., Sreekanth, D., Bose, A. C., Muthupandi, V., & Subramanian, S. (2013). Fabrication and characterization of micro-arc oxidized fluoride containing titania films on Cp Ti. *Ceramics International*, 39(1), 801–812. <https://doi.org/10.1016/j.ceramint.2012.07.001>
- Venkateswarlu, K., Suresh, S., Rameshbabu, N., Bose, A. C., & Subramanian, S. (2012). Effect of electrolyte chemistry on the structural, morphological and corrosion characteristics of titania films developed on Ti-6Al-4V implant material by plasma electrolytic oxidation. *Key Engineering Materials*, 493–494, 436–441. <https://doi.org/10.4028/www.scientific.net/KEM.493-494.436>
- Wang, J., Pan, Y., Feng, R., Cui, H., Gong, B., Zhang, L., Gao, Z., Cui, X., Zhang, H., & Jia, Z. (2020). Effect of electrolyte composition on the microstructure and bio-corrosion behavior of micro-arc oxidized coatings on biomedical Ti6Al4V alloy. *Journal of Materials Research and Technology*, 9(2), 1477–1490. <https://doi.org/10.1016/j.jmrt.2019.11.073>

- Wang, Y., Yu, H., Chen, C., & Zhao, Z. (2015). Review of the biocompatibility of micro-arc oxidation coated titanium alloys. *Materials and Design*, 85, 640–652. <https://doi.org/10.1016/j.matdes.2015.07.086>
- Xu, L., Wu, C., Lei, X., Zhang, K., Liu, C., Ding, J., & Shi, X. (2018). Effect of oxidation time on cytocompatibility of ultrafine-grained pure Ti in micro-arc oxidation treatment. *Surface and Coatings Technology*, 342, 12–22. <https://doi.org/10.1016/j.surfcoat.2018.02.044>
- Yang, X., Yu, S., & Li, W. (2009). Preparation of bioceramic films containing hydroxyapatites on Ti-6Al-4V alloy surfaces by the micro-arc oxidation technique. *Materials Research Bulletin*, 44(4), 947–949. <https://doi.org/10.1016/j.materresbull.2008.09.048>
- Yao, Z., Jiang, Y., Jiang, Z., & Wang, F. (2007). Effects of duty ratio at high frequency on growth mechanism of micro-plasma oxidation ceramic coatings on Ti alloy. *Journal of Materials Science*, 42(22), 9434–9439. <https://doi.org/10.1007/s10853-007-1842-0>
- Yin, I. X., Zhang, J., Zhao, I. S., Mei, M. L., Li, Q., & Chu, C. H. (2020). The antibacterial mechanism of silver nanoparticles and its application in dentistry. In *International Journal of Nanomedicine* (Vol. 15, pp. 2555–2562). Dove Medical Press Ltd. <https://doi.org/10.2147/IJN.S246764>
- Zhang, X. F., Liu, Z. G., Shen, W., & Gurunathan, S. (2016). Silver nanoparticles: Synthesis, characterization, properties, applications, and therapeutic approaches. In *International Journal of Molecular Sciences* (Vol. 17, Issue 9). MDPI AG. <https://doi.org/10.3390/ijms17091534>
- Zhao, C., Feng, B., Li, Y., Tan, J., Lu, X., & Weng, J. (2013). Preparation and antibacterial activity of titanium nanotubes loaded with Ag nanoparticles in the dark and under the UV light. *Applied Surface Science*, 280, 8–14. <https://doi.org/10.1016/j.apsusc.2013.04.057>



**CHAPTER 8**  
**INVESTIGATION OF LARGE EXTRA DIMENSIONS IN THE**  
**MUON COLLIDER**

Prof. Dr Salih Cem İNAN<sup>1</sup>

---

<sup>1</sup>Sivas Cumhuriyet Üniversitesi, Fen Fakültesi, Fizik Bölümü, Sivas, Türkiye.  
ORCID ID: <https://orcid.org/0000-0002-2441-2347>, [sceminan@cumhuriyet.edu.tr](mailto:sceminan@cumhuriyet.edu.tr)



## INTRODUCTION

The Hierarchy problem in interactions of particle physics stems from the enormous disparity in energy between the electroweak energy scale of around a few hundred GeV and the Planck scale of approximately  $10^{19}$  GeV in four-dimensional spacetime. String theory has already introduced the existence of extra spatial dimensions beyond the three. In the framework of string theory, the three-dimensional spatial world is referred to as a "wall" or 3-brane, where all Standard Model particles reside. The D-dimensional spacetime, encompassing  $D = 3 + \delta + 1$  dimensions, including  $\delta$  additional spatial dimensions, is termed the "bulk" within which the 3-brane is embedded. The approaches to addressing the hierarchy problem depend on the specific model employed.

In the model which is suggested by the Arkani-Hamed, Dimopoulos, and Dvali (named ADD model), gravity is proposed to propagate within the bulk, while the Standard Model fields are confined to the 3-brane (Arkani-Hamed, Dimopoulos, and Dvali 1998). Solving the linearized equations of motion for the metric field yields the Kaluza-Klein tower in D dimensions. Upon integrating over the extra dimensions, the resulting 4-dimensional fields manifest as the Kaluza-Klein modes. The zero mode of the KK field is massless, giving rise to the 4-dimensional graviton. The excited modes of the KK fields acquire mass. According to this framework, extra dimensions undergo compactification with a radius  $r_c \sim \text{mm-fermi}$  (or  $\frac{1}{r_c} \sim \text{eV-MeV}$ ), defining the spacing of KK modes. This mode spacing is significantly smaller than typical collider energies, enabling the summation over a large number of KK states. The ADD model, also referred to as the large extra dimension model, is characterized by its expansive compactification radius. Strong gravity manifests in  $D = 4 + \delta$  dimensions due to the cumulative effect of KK states. Consequently, its effective interactions with Standard Model particles in 4 dimensions are anticipated to be measurable at collider energies. The relationship between the Planck Mass  $M_{pl}$  and the corresponding scale  $M_D$  in D dimensions can be expressed using the compactified volume  $V_\delta$ .

$$M_{pl}^2 = V_\delta M_D^{2+\delta} \quad (1)$$



Assuming the TeV range for  $M_D$ , the sizable higher-dimensional volume  $V_\delta$  leads to a substantial increase in  $M_{pl}$  for  $\delta$  values between 2 and 7. This outcome suggests that the Planck scale  $M_{pl}$  may not be the fundamental scale after all. The sizable disparity between the electroweak and Planck scales is offset by the large compactification scale of the extra dimensions. It is important to note that this does not resolve the hierarchy problem entirely; instead, the significant gap is shifted to the compactification radius and the inverse of the electroweak scale.

This study aims to scrutinize the ADD model by analyzing the  $\mu^+\mu^- \rightarrow \mu^+\mu^-$  interaction at a proposed muon collider. The concept of the muon collider was introduced by F. Tikhonin in the late 1960s (Tikhonin 1968), and it was further discussed in the early 1980s (Skrinsky and Parkhomchuk 1981). Currently, the remarkable potential of the muon collider for collisions of elementary particles at extremely high energies is under active investigation. Its advantage stems from the ability to accelerate muons in a ring without the constraints imposed by synchrotron radiation, unlike linear or circular electron-positron colliders (Long et. al 2021). For instance, the muon collider could provide a determination of the electroweak couplings of the Higgs boson with significantly higher precision than what is considered achievable at other future colliders (Bandyopadhyay P. and Costantini A. 2021). The interest in designing and constructing a muon collider also arises from its capacity to probe physics beyond the SM. Numerous recent studies have explored the search for such as SUSY particles (Capdevilla et. al 2021 ), WIMPs (Black K., et al.), and dark matter (Jueid and Nasri 2023), vector boson fusion (Costantini et al. 2020) In our recent paper, we investigated axion-like particles (ALPs) at high-energy muon colliders (İnan and Kisselev 2023). For more details on the exceptional opportunity offered by the muon collider in directly exploring the energy frontier, refer to (Black et. al 2023).

## METHOD

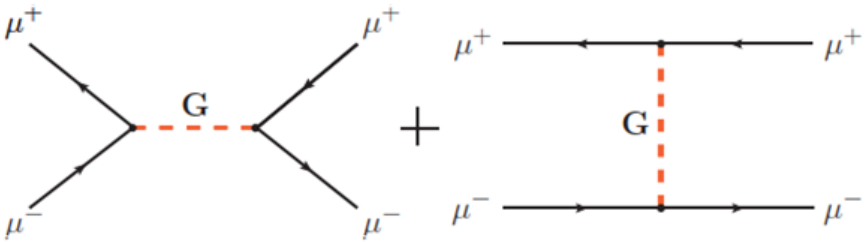
In this study, we have calculated the cross sections for the  $\mu^+\mu^- \rightarrow \mu^+\mu^-$  with contribution of the extra dimensions. The total cross section ( $\sigma$ ) could be obtained by integrating the differential cross section  $\left(\frac{d\sigma}{d\Omega}\right)$  as follows,

$$\sigma = \int_0^{2\pi} \frac{d\sigma}{d\Omega} d\Omega.$$

Here, differential cross section of the  $\mu^+\mu^- \rightarrow \mu^+\mu^-$  process is can be obtained using sum of squared of the helicity amplitudes,

$$\frac{d\sigma}{d\Omega} = \frac{1}{64\pi^2 s^2} \sum_{\lambda_i} |M_{\lambda_i}|^2$$

where,  $s$  is the squared center of mass energy of the muon collider,  $\lambda_i$  are helicities. The total helicities can be obtained as  $M = M_{SM} + M_{KK}$ . Here,  $M_{SM}$  is the SM amplitude and,  $M_{KK}$  is the ADD model amplitude, respectively. The Feynman diagrams for the ADD model contrubitions includes  $s, t$  channels as shown in fig.1.



**Figure 1.** Feynman Diagrams  $\mu^+\mu^- \rightarrow \mu^+\mu^-$  for the extra dimensions contrubition.

The squared amplitudes for the can be obtained as follows ,

$$iM_{KK}(s) = \sum_n \left[ \bar{v}(p_2)\Gamma_1^{\mu\nu}(p_1, p_2)u(p_1) \frac{i}{2} B_{\mu\nu\alpha\beta} \bar{u}(p_3)\Gamma_2^{\alpha\beta}(p_3, p_4)v(p_4) \right],$$

$$iM_{KK}(t) = \sum_n \left[ \bar{u}(p_3)\Gamma_1^{\mu\nu}u(p_1) \frac{i}{2} B_{\mu\nu\alpha\beta} \bar{v}(p_2)\Gamma_2^{\alpha\beta}v(p_4) \right].$$

(4)

The  $\Gamma_i^{\mu\nu}(p_1, p_2)$  vertex factor has been shown in (Guidice, Ratazzi, and Wells 1999). Squared amplitudes can be obtained using these equations. By employing the MONTE CARLO method in our FORTRAN code, we will evaluate the total cross sections. Statistical analysis is imperative to ascertain whether the experimental measurement of Kaluza-Klein graviton contributions to cross sections is feasible. Therefore, we will conduct a statistical analysis. Consequently, the potential of photon-photon reactions at the muon colliders to probe extra dimensions will be elucidated.

### RESULTS

The squared amplitudes for the  $\mu^+\mu^- \rightarrow \mu^+\mu^-$  with extra dimensions contrubitions (as shown in fig.1) can be obtained as follows,

$$|M_{KK}(s)|^2 = \frac{1}{512} |\kappa^2 D(s)|^2 (s^4 + 10s^3t + 42s^2t^2 + 64st^3 + 32t^4)$$

$$|M_{KK}(t)|^2 = \frac{1}{512} |\kappa^2 D(t)|^2 (t^4 + 10t^3s + 42s^2t^2 + 64ts^3 + 32s^4)$$

$$|M_{KK}(s, t)|^2 = \frac{1}{512} Re|\kappa^4 D(s)D(t)^*| (s + t)^2 (4st)$$

$$|M_{int}(s)|^2 = -Re(\kappa^2 D(s)) g_e^2 (s^4 + 16t^3s + 15s^2t^2 + 7ts^3 + 8t^4) / 2st$$

$$|M_{int}(t)|^2 = -Re(\kappa^2 D(s)) g_e^2 (t^4 + 7t^3s + 15s^2t^2 + 16ts^3 + 8s^4) / 2st$$

$$|M_{SM}|^2 = 16g_e^4 (s^2 + ts + t^2)^2 / (st)^2$$

$$|M|^2 = |M_{KK}(t)|^2 + |M_{KK}(s, t)|^2 + |M_{int}(s)|^2 + |M_{int}(t)|^2 + |M_{SM}|^2$$

(5)

Here  $\kappa$  is the coupling constans, s,t, and, u are Mandestam variables and,  $D(s)$  is the ADD model propagator terms which is includes summation over the Kaluza-Klein modes. Due to the infinite nature of the Kaluza-Klein (KK) tower, tree-level processes exhibit ultraviolet divergences. Consequently, a cutoff procedure is necessary. The fundamental steps of the approach employed by Guidice et al. 1999. For phenomenological applications are outlined below:

$$\begin{aligned} &\kappa^2 D(s) \\ &= -\frac{16i\pi}{(\delta - 2)} \end{aligned}$$

The relationship between the unknown cutoff energy  $\Lambda_c$  and the fundamental scale  $M_D$  remains ambiguous without a complete understanding of the underlying theory. String theory suggests the connection  $\Lambda_c > M_D$ . Several studies have demonstrated the equality  $\Lambda_c \approx M_D$ , establishing a lower bound for the fundamental scale  $M_D$ . In this work, we assume  $\Lambda_c \approx M_D$  for the graviton propagator of the ADD model. All calculations in this article we have used  $\delta = 4$ .

The differential cross section for the process is depicted in Figure 2, assuming a collision energy of 100 TeV. The Standard Model predictions are also shown for comparison. As can be seen from the figure, the discrepancy between the cross section and its Standard Model component grows considerably as the collision energy increases.

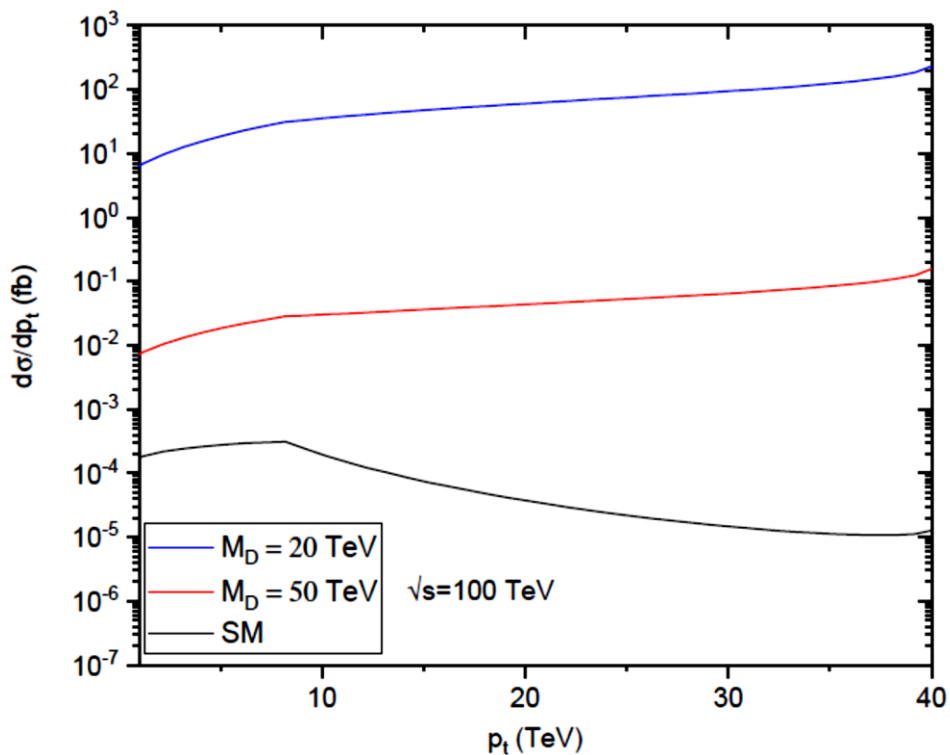
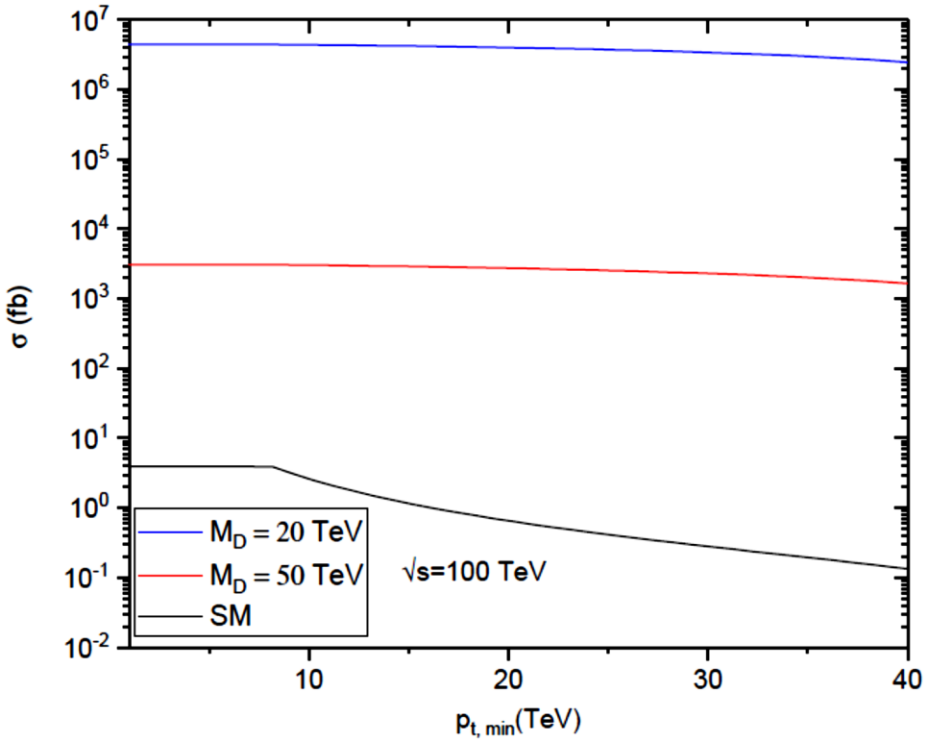


Figure 2. The differential cross sections as a function of the  $p_t$ .

Above trend is also observed for the total cross section, where  $p_{t,min}$ , denotes the minimum transverse momentum of the final muons, as illustrated in Figure 3. As can be seen from this figure, as the  $p_{t,min}$  increases, the new physics contributions almost do not change, while the SM cross section gradually decreases. Thus, sensitivity limits can be further improved by applying a high  $p_t$  cut.



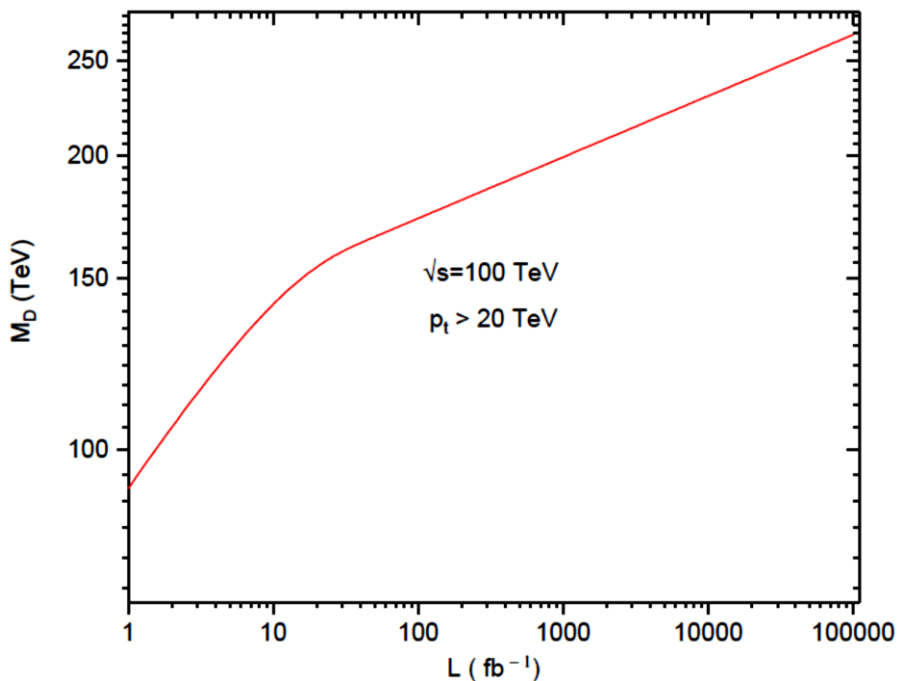
**Figure 2.** The total cross sections as a function of the  $p_{t,min}$ .

Also, in all our calculations, we applied a cut on the rapidity and transverse momentum of the outgoing photons  $|\eta| < 2.5$  and  $p_t > 30$  GeV, respectively.

In order to evaluate the sensitivity, we employ the following equation for the statistical significance SS,

$$SS = \sqrt{2(S - B(1 + \ln[1 + s/B]))}$$

where  $S$  represents the number of signal events and  $B$  represents the number of background events. We identify regions that can be statistically ruled out at the 95% confidence level (C.L.). To reduce the SM background as mentioned above, we implement a cut of 20 TeV. The sensitivity bounds for the product of the coupling strength and the fundamental scale  $M_D$  as a function of the muon collider luminosity are illustrated in Figure 4.



**Figure 4.** % 95 C. L sensitivity bounds  $M_D$  as function of the muon collider luminosity.

## DISCUSSION AND CONCLUSION

The possibility of detecting large extra dimensions using the  $\mu^+\mu^- \rightarrow \mu^+\mu^-$  scattering at a future very high energy muon has been examined. Explicit expressions for the squared amplitudes of the this process which is also included extra dimensions and SM have been derived. Utilizing these squared amplitudes, we obtained the differential cross sections with respect to

the transverse momentum of the final leptons. Additionally, the total cross section as a function of the minimum transverse momentum has been calculated. The study encompasses center of mass energies of  $\sqrt{s} = 100$  TeV. At this energy value in the muon collider, the integrated luminosity increases up to  $1000 \text{ ab}^{-1}$  and this value was used in the calculations.

Consequently, we have established the 95% C.L. sensitivity bounds for the fundamental scale  $M_D$  arising from scattering  $\mu^+\mu^- \rightarrow \mu^+\mu^-$  at the muon collider. The best experimental limits are  $M_D > 11.2$  TeV for the graviton production (Aad et al. (ATLAS) 2021) and,  $M_D > 9.9$  for the virtual graviton effects (Sirunyan et al. (CMS) 2018). As can be seen from Figure 4, the sensitivity limits obtained in this study are much better. In conclusion, muon colliders, with their high energy and luminosity values, have great potential in the search for large additional dimensional model.

**REFERENCES**

- AaD G. et al. (ATLAS) (2021), Search for new phenomena in events with an energetic jet and missing transverse momentum in pp collisions at  $\sqrt{s}=13$  TeV with the ATLAS detector, *Phys. Rev. D* 103, 112006.
- Arkani-Hamed, N., Dimopoulos S., and Dvali G. (1998), The Hierarchy Problem and New Dimensions at a Millimeter *Phys. Lett. B* 429, 263.
- Bandyopadhyay P. and Costantini A. (2021), Obscure Higgs boson at colliders, *Phys. Rev. D* 103, 015025 (2021) [arXiv:2010.02597].
- Black K. M., et al. (2023), Muon collider forum report, arXiv:2209.01318.
- Black K., et al. (2022), Prospects for heavy WIMP dark matter searches at muon colliders, [arXiv:2205.10404].
- Capdevilla R., Meloni F., Simionellod R., and Zurita J. (2021), Hunting wino and higgsino dark matter at the muon collider with disappearing tracks, *JHEP* 06, 133 [arXiv:2102.11292].
- Costantini A. et al., Vector boson fusion at multi-TeV muon colliders, *JHEP* 10, 080 [arXiv:2005.10289].
- Guidice G. F., Ratazzi R., and Wells J. D. (1999), Quantum Gravity and Extra Dimensions at High-Energy Colliders *Nucl. Phys. B* 544, 3.
- Inan S. C., and Kisselev A. V. (2023), Probe of axion-like particles in vector boson scattering at a muon collider, *J. Phys. G: Nucl. Part. Phys.* 50 105002.
- Jueid A., and Nasri S. (2023), Lepton portal dark matter at muon colliders: Total rates and generic features for phenomenologically viable scenarios, [arXiv:2301.12524].
- Long, K.R., Lucchesi, D., Palmer, M. A., Pastrone N., Schulte, D. and Shiltsev V. (2021), Muon colliders to expand frontiers of particle physics, *Nature Phys.* 17, 289 [arXiv:2007.15684].
- Sirunyan A. M. et al. (CMS) (2018), Search for new physics in dijet angular distributions using proton-proton collisions at  $\sqrt{s}=13$  TeV and constraints on dark matter and other models *Eur. Phys. J. C* 78, 9, 789.
- Skrinsky, A. N. and Parkhomchuk V. V. (1981), Cooling methods for beams of charged particles (in Russian), *Sov. J. Part. Nucl.* 12, 223.
- Tikhonin, F.F. (1968) , On the effects of the clashing  $\mu$ -meson beams (in Russian), JINR Report P2-4120, Dubna, On the effects at colliding mu-meson beams, arXiv:0805.3961.





## **CHAPTER 9**

### **DESIGN STRUCTURE MATRIX MODELING FOR SUSTAINABLE PRODUCT DESIGN: A CASE OF THE THERMAL MANAGEMENT SYSTEM OF AN ELECTRIC VEHICLE**

Sheharyar MUMTAZ<sup>1</sup>

Tufail HABIB<sup>2</sup>

---

<sup>1</sup> Department of Industrial Engineering, University of Engineering & Technogolgy, Peshawar, Pakistan.<sup>1</sup>ORCID ID: <https://orcid.org/0000-0000-0000-0000>  
<sup>1</sup>sheharyarmuntaz@outlook.com,

<sup>2</sup> Department of Industrial Engineering, University of Engineering & Technogolgy, Peshawar, Pakistan <sup>2</sup>ORCID ID: <https://orcid.org/0000-0002-1424-5960>  
<sup>2</sup>tufailh@uetpeshawar.edu.pk,



## **1. INTRODUCTION**

With a growing worldwide awareness of environmental concerns and the need for responsible and resource-efficient solutions, sustainable product design has become a major paradigm in engineering and innovation. The automotive industry must create environmentally friendly designs that minimise negative effects on the environment while simultaneously meeting safety and performance criteria as the shift to electric vehicles (EVs) accelerates. One of the main areas of focus for sustainable design in electric vehicles is the Thermal Management System (TMS), which controls the temperature of the vehicle. In line with sustainability principles, efficient heat management not only guarantees maximum operational efficiency but also extends the life of the vehicle's components.

In the context of designing sustainable products, the Design Structure Matrix (DSM) shows itself as a potent tool that provides an organised method for modelling and analysing intricate interdependencies within a system. Through the application of DSM, designers and engineers can acquire a comprehensive grasp of the design process by learning about the complex interrelationships between the many parts of the Thermal Management System. In particular, the use of DSM modelling to sustainable product design for electric car Thermal Management System is examined in this research. DSM is a thorough technique that helps find optimisation opportunities and makes sure sustainability factors are smoothly incorporated into the design process from the beginning.

A number of studies have emphasised the value of using tools like DSM to incorporate sustainability into product design approaches. The use of DSM in sustainable design is crucial for electric car thermal management system optimisation. Moreover, DSM may be used to improve the eco-efficiency of automobile components, offering insightful information for sustainable engineering methods. This research adds to the body of knowledge by exploring the case of the Thermal Management System in electric vehicles and demonstrates how DSM may be used as a tactical instrument to promote sustainable practices in the field of automotive engineering.

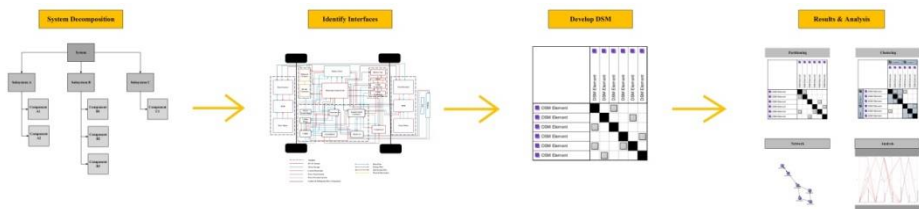
Shorter product life cycles, fast product development and market demands are some of the issues to the manufacturers of vehicular climate control and air conditioning system. In order to address these issues, new

approaches and techniques are required in the product development phase to achieve the benefits of design for manufacturing (DFX) and concurrent engineering.

## 2. RESEACH METHODOLOGY & TECHNIQUE

Complex products can be broken down into subsystems, components, and functions using this methodology's system decomposition technique. In order to construct the system architecture, a software application called Cambridge Advanced Modeler is utilised to model the system elements and their interactions in DSM. The architecture in this example is used to manage relationships between components and subsystems, identify system modules, and show the findings of the structural analysis.

Figure 1 shows the overall approach of system decomposition and DSM modelling in this paper based on (Eppinger & Browning, 2012). The relationships between the system's components are determined via system decomposition. In the instance of the TESLA Model Y Thermal Management System, information on interfaces and the system's physical makeup is gathered via research papers, patents, product films, and expert system breakdowns. The system's components are arranged in a matrix display format along the rows and columns in the following stage. The system matrix is created for this purpose using the Cambridge Advanced Modeller (CAM) software programme (Wynn, Wyatt, Nair, & Clarkson, 2010). Lastly, the system architecture (DSM form) is analysed, including partitioning, clustering, and network diagram display. Although this paper is restricted to product architecture DSM, this DSM can be further expanded to multiple domain matrices (MDM) for analysing issues connected to process and organisation.



**Figure 1:** Product decomposition and analysis approach using DSM modeling (adapted from Eppinger and Browning [1])

## **2.1 System Decomposition**

The main subsystems of **Thermal Management System (TMS) of TESLA Model Y** are HVAC system, power provision and conversion system, electronic control subsystem, and drive unit subsystem.

## **2.2 Interface Identification**

Four types of interfaces were identified between the components of **Thermal Management System (TMS) of TESLA Model Y**. They are given as follows:

- 1 Physical Interaction
- 2 Matter Flow (e.g. refrigerant flow)
- 3 Energy Flow (e.g. thermal, electrical, etc.)
- 4 Information Flow (e.g. actuator commands, sensor signals)

**Spatial interfaces** in **Thermal Management System (TMS) of TESLA Model Y** play critical role in optimizing temperature distribution within the vehicle. **TESLA** employs advanced thermal control mechanisms to efficiently regulate the temperature of the battery, electric motors, and cabin. Utilizing a network of sensors and actuators, the system strategically directs airflow and coolant circulation to dissipate heat generated during operation. This spatially refined approach ensures that thermal energy is effectively managed, enhancing overall performance, extending battery life, and maintaining a comfortable environment for passengers and components within the **TESLA Model Y**.

**Material interfaces** between components in **Thermal Management System (TMS) of TESLA Model Y**, are meticulously designed to facilitate the efficient flow of refrigerant and coolant, crucial for heating and cooling the vehicle. These interfaces ensure a seamless movement of fluids through a network of conduits, passages, and heat exchangers. Refrigerant, typically used for cooling purposes, flows through specialized components like compressors and evaporators, absorbing heat and lowering the temperature in the process. Coolant, on the other hand, circulates through various components to regulate the temperature of the battery, electric motors, and other vital parts. The interfaces between these components and the flow of fluids are engineered to optimize heat transfer, minimize energy loss, and maintain precise thermal conditions within the **TESLA Model Y**. This

precision in fluid flow and component interaction contributes to vehicle's energy efficiency, overall performance, and longevity.









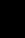

















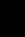

















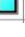


**Information interfaces** between components in **Thermal Management System (TMS) of TESLA Model Y** are fundamental for efficient operation. Sensors strategically placed throughout the system continuously monitor temperature, pressure, and other critical parameters. These sensors gather data and transmit signals to a central control unit, providing real-time information about the thermal state of the vehicle. The control unit processes this data and communicates instructions to actuators and motors, which regulate the flow of refrigerant, coolant, and air to manage the temperature effectively. This seamless exchange of information and signals among the components ensures precise and adaptive control of **Thermal Management System (TMS) of TESLA Model Y**, optimizing thermal performance, enhancing energy efficiency, and ultimately contributing to the seamless functioning of the **TESLA Model Y**.

**Energy interfaces** between components in **Thermal Management System (TMS) of TESLA Model Y**, are essential to power and drive the system's functionality. **Thermal Management System (TMS) of TESLA Model Y** relies on various forms of energy, including thermal, electrical, and potential energy stored in the battery. Electrical energy powers motors, pumps, and fans that facilitate the circulation of refrigerant and coolant, ensuring efficient heat transfer and temperature regulation. Thermal energy is utilized to drive processes like refrigerant compression and absorption, playing a pivotal role in cooling functions. Additionally, potential energy stored in the battery is harnessed to initiate the **Thermal Management System (TMS) of the TESLA Model Y** and sustain its operation. The seamless integration and management of these energy interfaces ensure that the **Thermal Management System (TMS) of the TESLA Model Y** functions optimally, contributing to the overall performance, efficiency, and sustainability of the **TESLA Model Y**.

### 2.3 Design Structure Matrix (DSM)

As we are dealing with a electromechanical system, we'd make use of component DSM. A component DSM is a tool used in project management and systems engineering to represent and analyze the relationships among different components within a system or product. It's often used to visualize dependencies and interactions, making it easier to manage complex systems.

Design Structure Matrix (DSM) is widely used across different streams of research to show the relations between the elements of a system. We'll make use of DSM to model the **Thermal Management System (TMS) of the TESLA Model Y**. Following is an example of component DSM.

	 LCC	 Nylon Coolant Manifold	 Cabin Condenser	 Reservoir	 Battery Pressure Solenoid	 Pentaport Hoses	 Octovalve
 LCC		  		  			
 Nylon Coolant Manifold	  						  
 Cabin Condenser	 					 	
 Reservoir		  					 
 Battery Pressure Solenoid							
 Pentaport Hoses			 				
 Octovalve		  					

**Figure 2:** Sample DSM showing 4 elements of Thermal Management System of the TESLA Model Y

A DSM could be read through two ways. One can read through its row that gives input to the elements in the column. Another way is to consider the elements in the left column as giving inputs to the elements in the first row of the DSM.

I've designed the DSM of **Thermal Management System (TMS) of TESLA Model Y** in the later fashion that is the elements in the column represent inputs to the elements in the column.

The 4 interactions/interfaces between the functional components of the **Thermal Management System (TMS) of TESLA Model Y** are shown with 4 different colors. The representation of the colors is as follows:

1. Red = Energy Flow
2. Sky Blue = Mass Flow



3. Black = Information Flow
4. Orange = Physical Interface

### 2.3.1 DSM Model

Composite DSM model constructed using Cambridge Advanced Modeler (CAM) is displayed in figure 3 below. It shows the decomposition of **Thermal Management System (TMS) of TESLA Model Y** into 36 functional components. 4 types of interfaces such as energy flow, mass flow, information flow, and physical interface are indicated through 4 colors such as red, sky blue, black, and orange, respectively.

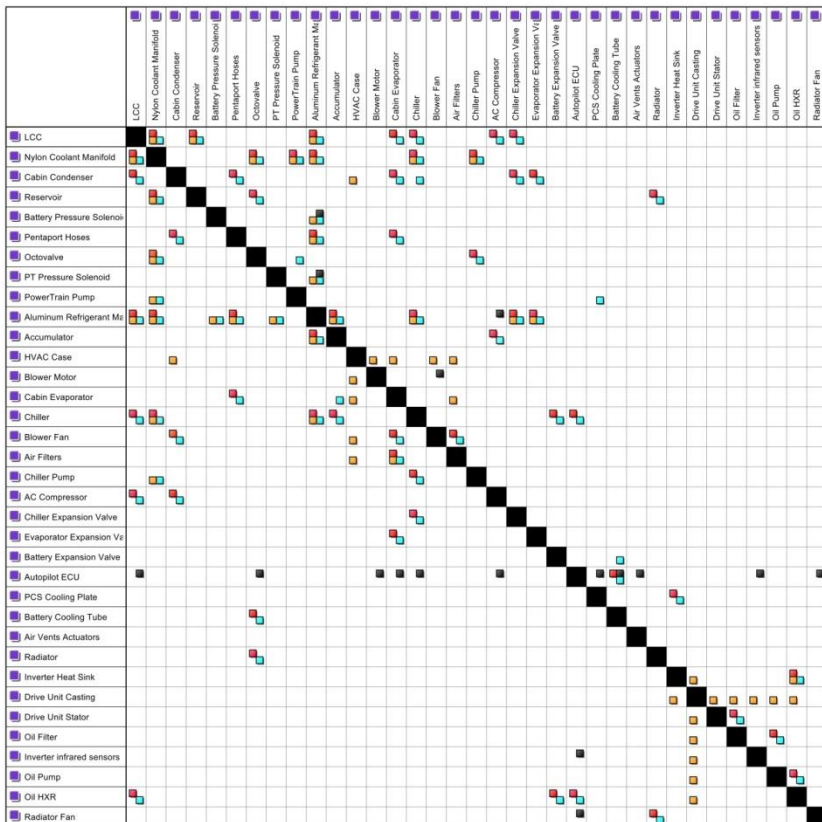


Figure 3: Composite DSM of Thermal Management System of TESLA Model Y

### 3. RESULTS AND ANALYSIS

Once the DSM is developed, analysis could be done through the following tools:

1. Clustering
2. Partitioning
3. Structure Analysis

A DSM only on the physical interactions between the components was analyzed in CAM using the clustering algorithm. The algorithm clustered some of the closely physically interacted components into clusters that represented modules. Other components were scattered throughout the DSM which were more functionally connected rather than spatially.

The components that are more functionally connected than spatially (physically) are the ones that are more integrative rather than modular. Some of these components are Autopilot ECU, Battery Cooling Tube, PCS Cooling Plate, etc. You can see these integrative components being sparsely scattered throughout the DSM.

In the DSM of **Thermal Management System (TMS) of the TESLA Model Y**, there are 3 modules identified strictly based on physical interaction of the comprising components in each module. These modules are:

1. Super Manifold Assembly
2. HVAC Module
3. Drive Unit

The resulting DSM of the clustering algorithm is as follows in figure 4.

ilece

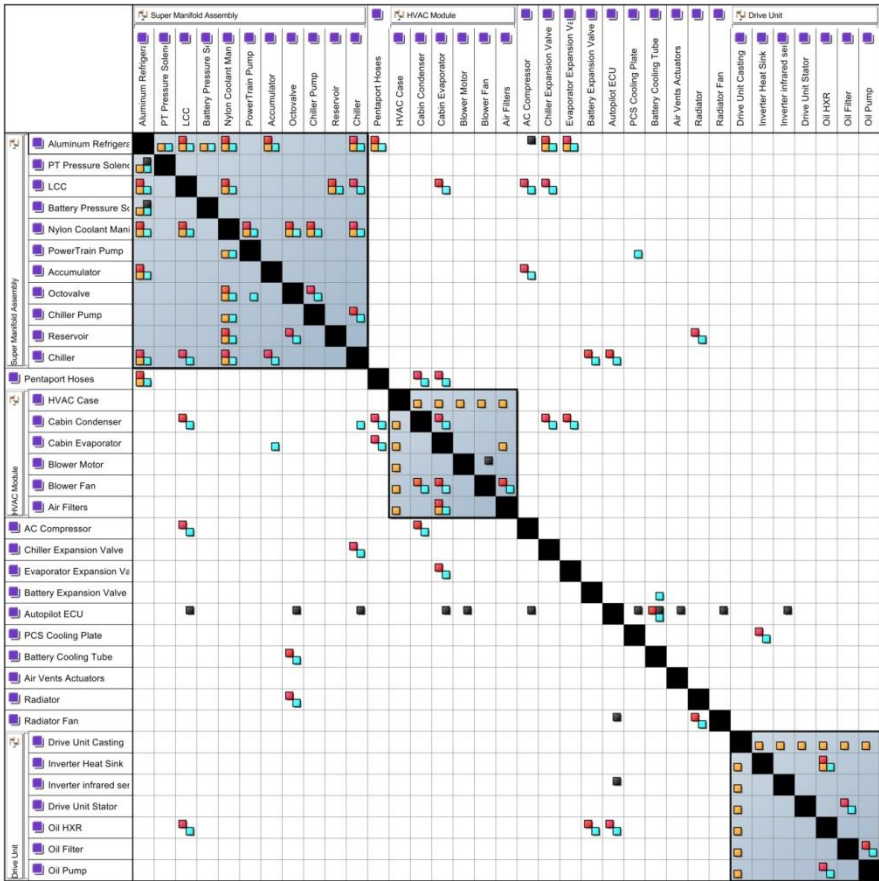


Figure 4: Clustering of Composite DSM Thermal Management System of TESLA Model Y

**Thermal Management System (TMS) of TESLA Model Y** is a relatively complex system. Partitioning enhances the manageability and efficiency of complex systems, allowing for more effective design, development, and maintenance. It is a valuable technique for optimizing various aspects of project management and engineering, ultimately contributing to the success and quality of the final product.

Because of feedback loops, edges in complex structures cannot align on one side of the matrix diagonal. The next step in partitioning is to align as many edges as possible as close to the diagonal and as few edges below it.

Dependencies are accumulated via partitioning on one side of the DSM's diagonal. Bring the interactions as near to the diagonal as you can if that's difficult to understand.

Figure 5 shows the partitioning algorithm applied on composite DSM of Thermal Management System (TMS) of the TESLA Model.

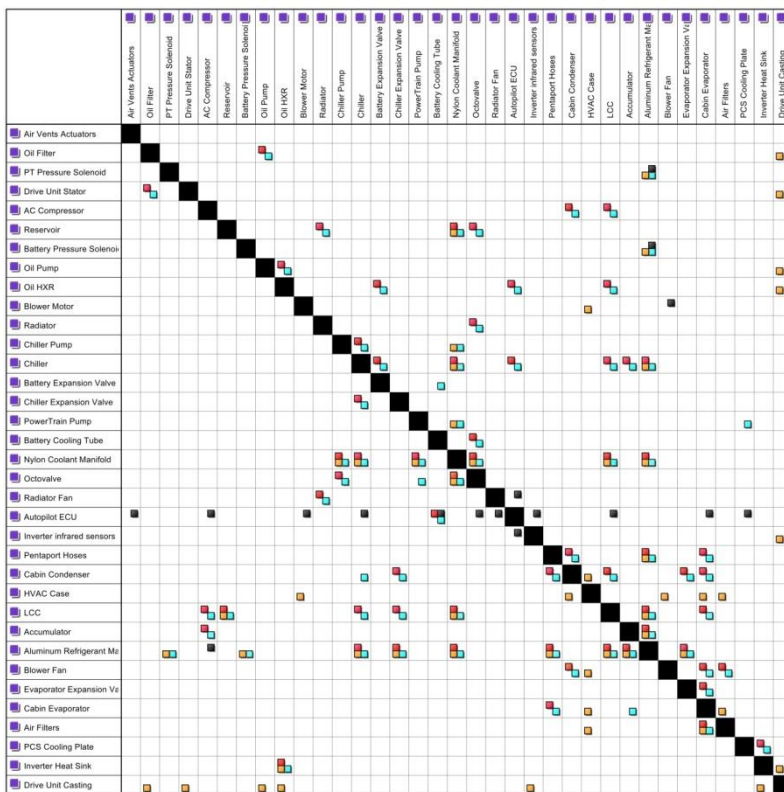


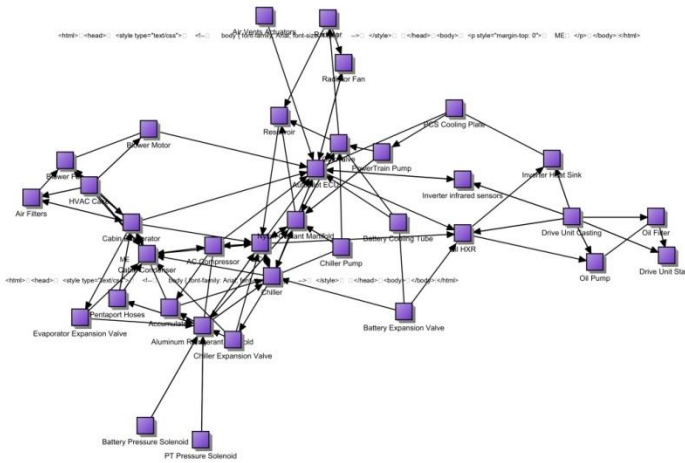
Figure 5: Partitioning of Composite DSM Thermal Management System of TESLA Model Y

### 3.1 Structural Representation and Analysis

Thermal Management System (TMS) of TESLA Model Y is a complex system that needs to be visualized in a network diagram to reduce

the complexity in one's mind. Figure 6 gives a detailed network view of how the components are connected to each other. Each node represent a component and each edge connecting two nodes represents the connections between the components. If you observe the network closely, you'd find Autopilot ECU, Nylon Coolant Manifold and Aluminum Refrigerant Manifold are more connected than other components.

Modular designs ought to have a lower function to component ratio than integral systems, in accordance with Ulrich's definition.



**Figure 6:** Structure representation of Thermal Management System (TMS) of the TESLA Model Y in network view

A structure's attainability is determined by measuring any change in a node and how that change affects the other nodes in the structure. A node's attainability is determined by dividing the number of nodes it actually reaches by the maximum number of nodes it is theoretically capable of reaching. In the above network diagram of **Thermal Management System (TMS) of TESLA Model Y**, Autopilot ECU and Nylon Coolant Manifold have more attainability than the rest of the nodes in the system. When a node has a high value of attainability, each change that is considered for the node can have an impact on a large number of other nodes. In general, in order to modify the

architecture or make structural modifications, the attainability in the nodes needs to be decreased. However, other factors, such as the nodes' lengths and routes, are also important for accurately characterizing the nodes.

### 3.1.1 Structural Analysis

Figure 7 gives us fairly enough information on the intricate mechanics of **Thermal Management System (TMS) of TESLA Model Y**.

Metric	Value
Relational density (Non-zero fraction)	0.09327731092436975
Number of sets	3.0
Singular-value modularity index (SMI)	0.27794285714285716
Number of edges per node	3.1714285714285713
Number of edges that cross a set b...	39.0
Number of nodes (discounting dupli...	35.0
Number of edges	111.0
Number of unconnected nodes	0.0
Number of nodes	35.0

Figure 7: Structure analysis results of composite DSM

Number of Sets in figure 7 represents the number of clusters that exist in the DSM of **Thermal Management System (TMS) of TESLA Model Y**. Figure 7 shows that there exist 3 clusters in the system.

Nodes represents the components on the network diagram and edges are the connections between nodes (components). Structure Analysis of the system shows us that number of nodes as in components in the system are 35 and the number of edges as in the connections between components is 111 while there are no unconnected nodes. Every node (components) is connected to another node (component).

Nodes represent the total number of clusters formed, number of nodes, edges and their connections, non-zero fraction (NZF) as well as

singular valve modularity index (SMI) in the structure. There are in total three clusters, all the nodes are connected with some kind of interface.

### 3.1.2 Relational Density (Non-Zero Fraction)

Relational density in the context of a Design Structure Matrix (DSM) refers to the degree of interconnectedness or dependencies between different elements (components, tasks, modules, etc.) represented in the matrix.

Relational density is a measure of how many connections or dependencies exist between the elements in the DSM. A high relational density indicates a high level of interdependence, meaning that many elements are connected to or dependent on each other. On the other hand, low relational density suggests a lower level of interdependence, where fewer connections exist.

Understanding relational density in a DSM is crucial for assessing the complexity and manageability of a system. Systems with high relational density may pose challenges in terms of coordination, change management, and understanding the overall system structure. Systems with lower relational density may be more modular and easier to manage, as changes to one module may have fewer ripple effects on the rest of the system.

Relational density in DSM is a measure of how tightly interconnected or dependent the elements of a system are, providing insights into the complexity and potential challenges of managing the system.

Non-Zero Fraction is a metric used to quantify relational density. NZF is the percentage of non-zero entities remaining in the DSM after the diagonal cells have been eliminated. The DSM's sparsity is indicated by the NZF. It is computed as follows:

$$\text{Non Zero Fraction} = \frac{\sum_{i=1}^N \sum_{j=1}^N \text{DSM}_{ij}}{N(N-1)}$$

Where, N = number of components

The NZF value of **Thermal Management System (TMS) of the TESLA Model Y** is 0.093 which turns into 9.3%. This implies the density of

the system. It implies that a total of 9.3% of the DSM is occupied while the rest is unoccupied. To put things in perspective, out of 1,225 cells in the DSM of **Thermal Management System (TMS) of the TESLA Model Y**, only 111 are occupied which makes up the density of the system 9.3%.

### 3.1.3 Singular Value Modularity Index (SMI)

The singular value modularity index assesses the general structure of connections among the components; it does not, however, assess the process of grouping the components into modules. The system's singular value decay rate is measured by the SMI.

$$SMI = \frac{1}{N} \arg \min \alpha \sum_{i=1}^N \frac{\sigma_i}{\sigma_1} - e^{-[i-1]/\alpha}$$

Where,  $\sigma$  is the singular values in the matrix, and  $N$  is the number of components and  $\alpha$  determine the decay rate. This index has a theoretical limit and is based on numbers between 0 and 1. A SMI that is closer to 1.0 indicates a larger degree of modularity, where the connectivity information is more dispersed. A system that is closer to zero is said to be more integral.

The SMI of **Thermal Management System (TMS) of TESLA Model Y** is 0.27 which is closer to 0. This indicates that the system is fairly integrative rather than modular. Although the algorithms in CAM clustered some elements and constructed some modules, the overall system is more integrative than modular.

## 4. Discussion and Conclusions

This paper presents a case study that uses the component DSM technique to analyze an existing product. The results largely rely on the type of product and cannot be generalized. The quantity of contacts, component connectivity, and the distribution of these interactions within the matrix are factors that influence a product's degree of modularization.

The multi domain system's architecture is examined in this paper by breaking down the mechatronic product. In order to accomplish this, the DSM technique breaks down the system into its component parts and subsystems, establishing the component interfaces in the process. Following the clustering algorithm's application, the DSM composed solely of physical interfaces differs from the composite DSM. Since there are fewer interfaces in a



physical interface DSM than in a composite DSM, more modules are created via the clustering process. Compared to mechanical parts, elements associated to information and control are more widely distributed and connected to other elements within the structure, resulting in a greater number of interfaces in the composite DSM. The partitioning matrix emphasizes key elements associated with module identification. As you partition things up, group the majority of the components that are potentially suitable for a module together around the diagonal. Because some system elements share numerous interfaces, some interfaces do not accumulate towards the diagonal.

An essential component of system architectural representation that includes nodes, edges, interfaces, and modules is structure analysis. System analysis may be challenging in a structure with a high degree of interconnection. As a structure's elemental connectedness increases, the number of feedback loops may rise sharply. This suggests that products have integrated structures, which leads to more interconnected products that need more work to redesign. The architecture of Thermal Management System of TESLA Model Y is nearly integrative, based on the SMI index and Ulrich's description of product architecture, even though certain modules are created after the application of clustering algorithm in CAM. When a basic system structure needs to be changed in order to establish product platforms and provide variation, structural optimization might be helpful. This helps developers to create customized system versions for their products (Lindemann, Maurer, & Braun, 2009). This suggests that a product platform that may be utilized for product customization can be created from a single product through structural optimization using DSM techniques. Application of several techniques, including ripping and structural Pareto analysis, is required for structure optimization.

The trade-off between modularity and integrality is a major problem in complex system design. To what extent should computer-controlled mechatronic products be modular? Hollta and Whitney (Höltkä-Otto, Suh, & de Weck, 2005; Whitney, 2002) state that modular architecture is driven by business demands such as variety, product modification, engineering standards, and service requirements, whereas integral architecture is driven by product performance (i.e., power consumption, weight, size, speed, etc.) and cost. They contend that, in contrast to low power signal processor type devices, total modularity is not always desirable in the case of high power mechanical items. Certain high-performance systems, like those seen in

automobiles and aircraft, seem to encourage highly linked architectures, in which a single component may execute several tasks (Liebeck, 2004). That means that products with technical performance limitations—like light weight, compact design, power efficiency, and speed—tend to have a higher functions-to-component ratio, meaning they are more essential. Examples of such products are mobile phones and electronic calculators, which don't include batteries or covers. However, while being microprocessor-based products (or sub products), products like computers are much more modular than those that (contain computer control mechanical pieces), like printers, and automobile engines.

## REFERENCES

- [1] Eppinger, S. D., & Browning, T. R. (2012). *Design Structure Matrix Methods and Applications*. The MIT Press. <https://doi.org/10.7551/mitpress/8896.001.0001>
- [2] Wynn, D., Wyatt, D., Nair, S., & Clarkson, P. (2010). *An Introduction to the Cambridge Advanced Modeller. Modelling and Management of Engineering Processes*.
- [3] Lindemann, U., Maurer, M., & Braun, T. (2009). *Structural Complexity Management*. Berlin, Heidelberg: Springer. <https://doi.org/10.1007/978-3-540-87889-6>
- [4] Hölttä-Otto, K., Suh, E. S., & de Weck, O. (2005). Tradeoff between modularity and performance for engineered systems and products. *Proceedings ICED 05, the 15th International Conference on Engineering Design*.
- [5] Whitney, D. E. (2002). *Physical Limits to Modularity* [Working Paper]. Massachusetts Institute of Technology. Engineering Systems Division. Retrieved from Massachusetts Institute of Technology. Engineering Systems Division website: <https://dspace.mit.edu/handle/1721.1/102731>
- [6] Liebeck, R. H. (2004). Design of the Blended Wing Body Subsonic Transport. *Journal of Aircraft*, 41(1), 10–25. <https://doi.org/10.2514/1.9084>

## CHAPTER 10

### DENSIFICATION AND FRACTURE STRENGTH PROPERTIES OF AL<sub>2</sub>O<sub>3</sub> BASED ZRO<sub>2</sub> AND SM<sub>2</sub>O<sub>3</sub> CONTAINING SANDWICH CERAMIC COMPOSITES

Tuğba ŞANLI<sup>1</sup>

Dr. Öğr. Üyesi Betül KAFKASLIOĞLU YILDIZ<sup>2</sup>

Arş. Gör. Elif İŞİK<sup>3</sup>

Prof. Dr. Yahya Kemal TÜR<sup>4</sup>

---

<sup>1</sup>Sivas University of Science and Technology, Institute of Graduate Studies, Department of Defence Technology, Sivas, Turkey..<sup>1</sup>ORCID ID: <https://orcid.org/0009-0003-7260-6650>

<sup>1</sup> [tugbasanli0921@gmail.com](mailto:tugbasanli0921@gmail.com)

<sup>2</sup> Sivas University of Science and Technology, Faculty of Engineering and Natural Sciences, Department of Metallurgical and Materials Engineering, Sivas, Turkey.

<sup>2</sup>ORCID ID: <https://orcid.org/0000-0002-6527-2918>

<sup>2</sup> [bkyildiz@sivas.edu.tr](mailto:bkyildiz@sivas.edu.tr)

<sup>3</sup> Sivas University of Science and Technology, Faculty of Engineering and Natural Sciences, Department of Metallurgical and Materials Engineering, Sivas, Turkey.

<sup>3</sup>ORCID ID: <https://orcid.org/0000-0001-8289-9512>

<sup>3</sup> [elif.isik@sivas.edu.tr](mailto:elif.isik@sivas.edu.tr)

<sup>4</sup> Gebze Technical University, Faculty of Engineering, Department of Materials Science and Engineering, Kocaeli, Turkey.

<sup>4</sup>ORCID ID: <https://orcid.org/0000-0002-9521-8875>

<sup>4</sup>[yktur@gtu.edu.tr](mailto:yktur@gtu.edu.tr)



## INTRODUCTION

Alumina ( $\text{Al}_2\text{O}_3$ ) ceramics is a material with high mechanical, tribological, thermal, and chemical properties that enable its use in many applications (Jiusti et al., 2017). Zirconia ( $\text{ZrO}_2$ ) is a ceramic material that shows different crystal structures at different temperatures. The transformation between these crystal structures (tetragonal-monoclinic) ensures toughening. Therefore, zirconia-reinforced alumina composites are of interest to many researchers and the disadvantages of  $\text{Al}_2\text{O}_3$  can be overcome by  $\text{ZrO}_2$  (Daguano et al., 2007). Samarium oxide ( $\text{Sm}_2\text{O}_3$ ) is a rare earth oxide with high melting temperature, dielectric constant, and thermal stability. The reaction caused by the addition of  $\text{Sm}_2\text{O}_3$  to the  $\text{Al}_2\text{O}_3$  structure results in the formation of the  $\text{SmAlO}_3$  phase. This phase with a rod-like structure can act as short fibers and increase the strength and toughness of  $\text{Al}_2\text{O}_3$  ceramics (Shi et al., 2020).

Laminated ceramics are formed by combining several layers of ceramics on top of each other. There is a thermal expansion difference between the ceramics used in the layers forming the laminated structure. Due to the difference in thermal expansion, residual compressive stresses occur on the surfaces. Because these stresses will play a role in preventing crack propagation, mechanical properties can be improved (Huang & Chen, 2016).

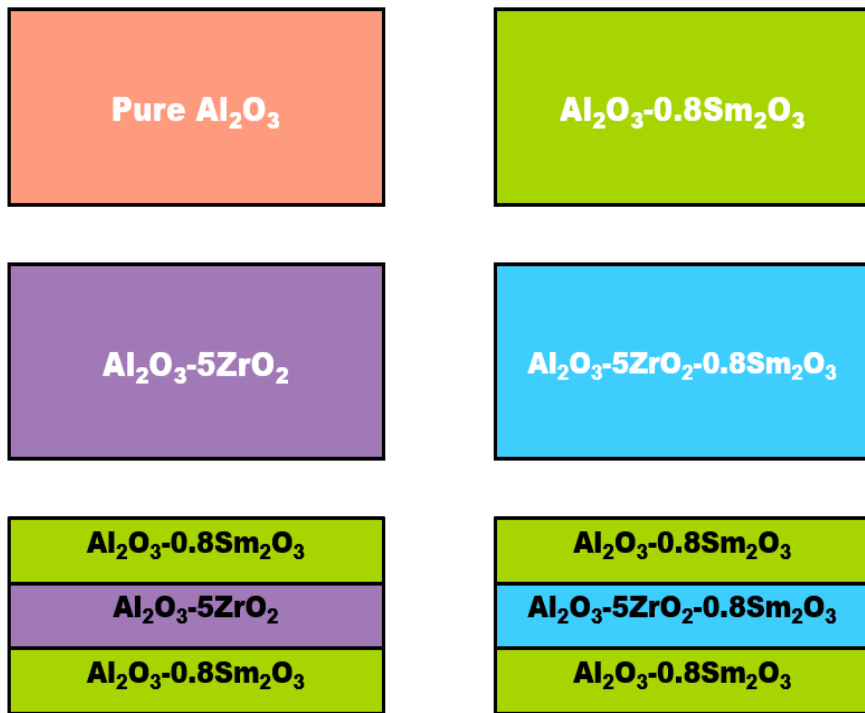
Zhaou et al. aimed to increase toughness and strength by producing an  $\text{Al}_2\text{O}_3$ - $\text{ZrO}_2$  composite in a three-layer structure. While  $\text{Al}_2\text{O}_3$ -5% $\text{ZrO}_2$  composite was used as the middle layer, the  $\text{ZrO}_2$  content in the surface layer was varied as 20, 30, and 40 wt%. As a result of the study, the highest strength and fracture toughness were achieved in the sandwich structure with a surface layer containing 30 wt%  $\text{ZrO}_2$  (Zhou et al., 2011).

When the literature studies were examined; it was seen that there were not many studies related to laminated structures. For this purpose, in this study, the effects of samarium oxide ( $\text{Sm}_2\text{O}_3$ ) and zirconium oxide ( $\text{ZrO}_2$ ) additives at different volume ratios on the microstructure and mechanical properties of  $\text{Al}_2\text{O}_3$  and  $\text{Al}_2\text{O}_3$ -based sandwich structures were examined separately. Especially, the effect of laminated structure and reinforcement materials on densification and mechanical properties were investigated.

## MATERIALS AND METHOD

In this study,  $\alpha$ -Al<sub>2</sub>O<sub>3</sub> powder (Alfa Aesar, Germany) with a grain size of 0.25-0.45  $\mu$ m with 99.5% purity was chosen as the matrix material. Sm<sub>2</sub>O<sub>3</sub> (99.95% purity and ~50 nm powder size, Nanografi, Turkey) and ZrO<sub>2</sub> (%3 mol yttria stabilize, MSE technology, Turkey) were preferred as reinforcement materials. Polyacrylic acid (Darvan 821A, MSE Tech Co. Ltd., Turkey) was used as a dispersant while the binder solution was prepared with polyvinyl alcohol (PVA, Sigma Aldrich) and glycerol (Sigma Aldrich).

In the study, both Al<sub>2</sub>O<sub>3</sub>-based sandwich structures and Al<sub>2</sub>O<sub>3</sub>-based samples with different volume fractions of Sm<sub>2</sub>O<sub>3</sub> and ZrO<sub>2</sub> were fabricated. Firstly, the reinforcement materials and Al<sub>2</sub>O<sub>3</sub> powder were mixed in distilled water with 0.5 wt% polyacrylic acid in a ball mill for 24 hours. Simultaneously, a binder solution with 2 wt% polymer (PVA + glycerol) was prepared. After the binder solution was added to the prepared powder mixture, mixing and drying were performed using a heated magnetic stirrer. The dried powders were crushed in an agate mortar and sieved through a 90  $\mu$ m sieve to prepare for shaping. Then, the powders were shaped in a uniaxial hydraulic press using a 35 mm diameter stainless steel mold. During the shaping of the sandwich samples, the powder of each layer was poured sequentially into the mold and each layer was pre-pressed with a pressure of 20 MPa. After the last layer was spread and pre-pressurized, a final pressure of 100 MPa was applied. Non-sandwich samples were shaped under a pressure of 40 MPa. Then, all samples in disc form were cold isostatic pressed at a pressure of 200 MPa. After binder burn-out at 600°C for 2 hours, the samples were sintered at 1550°C for 2 hours pressurelessly in air environment. The lapping process was performed to parallelize and ground the surfaces of the produced samples. The sample compositions produced are presented in Figure 1.



**Figure 1.** Compositions of the produced samples.

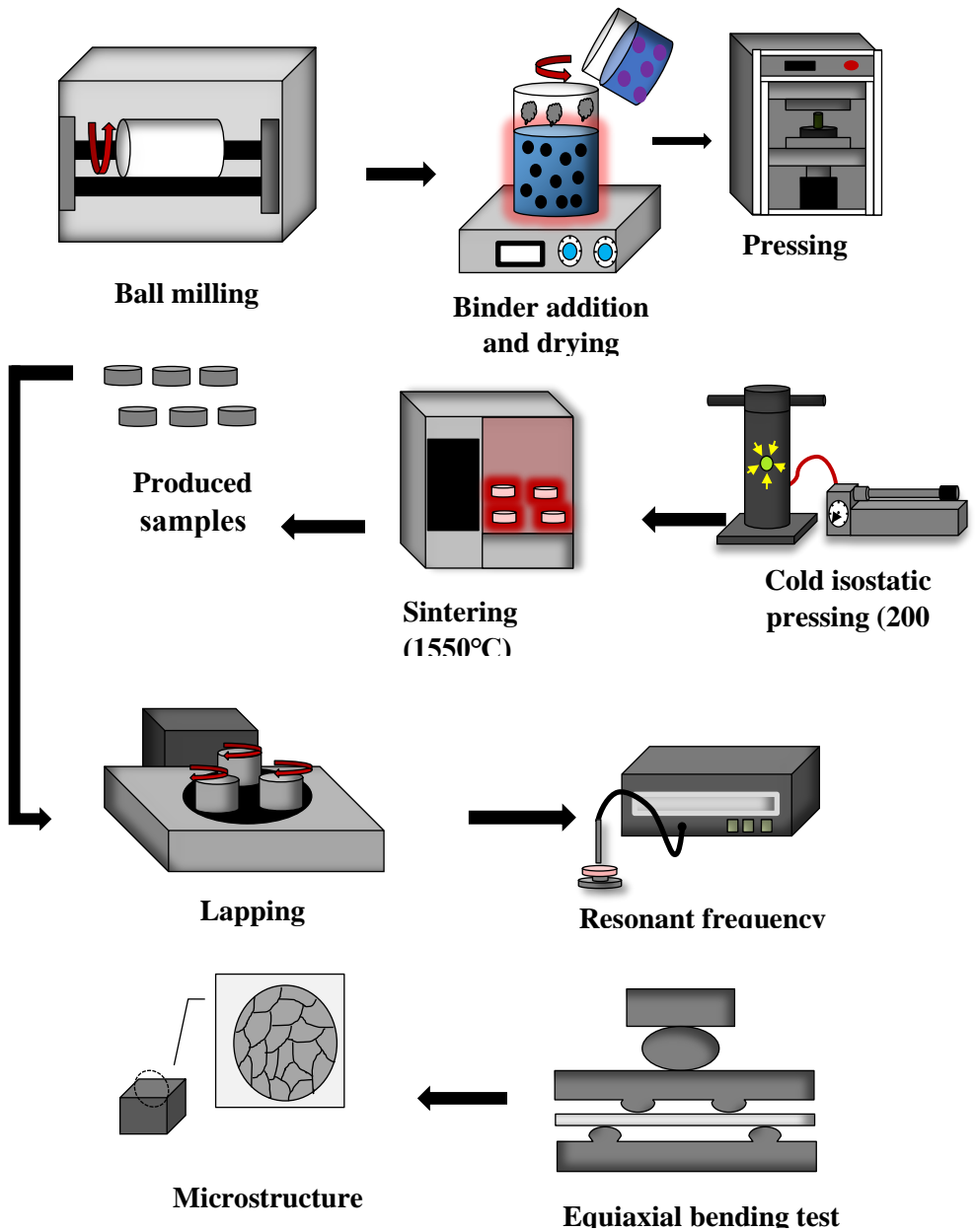
The bulk density measurements of the produced samples were carried out both volumetrically and using the Archimedes method. The resonance frequency method was used for elastic modulus measurements (ASTM C1259). Flexural strength was determined using the equibiaxial flexure strength test (ASTM C1499). SEM analyses were performed to examine microstructural properties. The phase and crystal structure of the samples were analyzed by XRD analysis. A schematic representation of the production process is given in Figure 2.

## RESULTS AND DISCUSSIONS

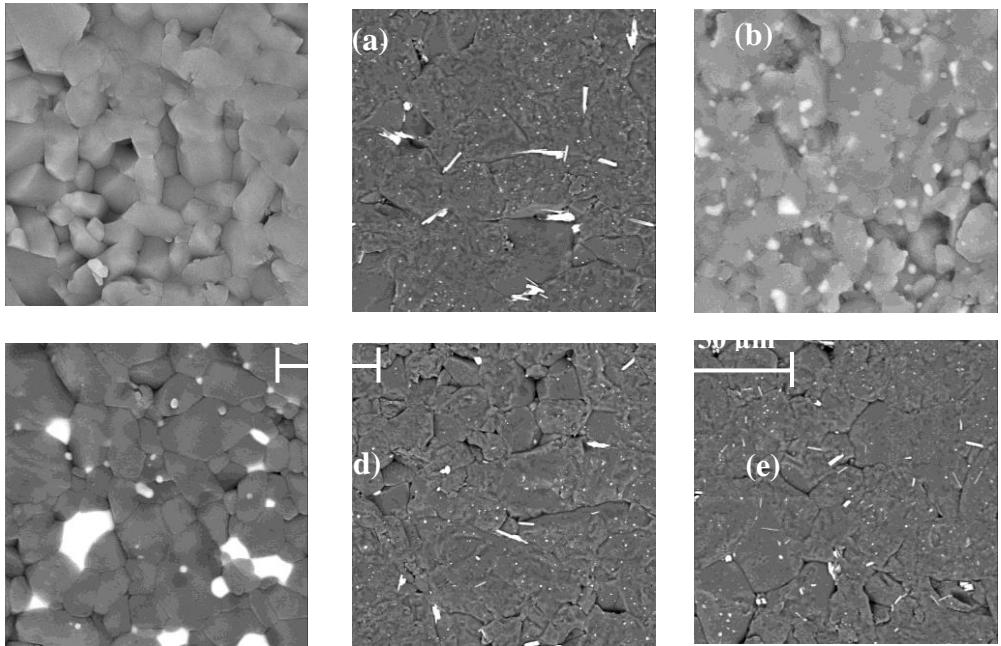
Figure 3 illustrates the SEM images of the surfaces of the produced samples after thermal etching at 1450°C/90 min. In the figures, the gray regions belong to  $\text{Al}_2\text{O}_3$  and the white regions belong to the additives  $\text{Sm}_2\text{O}_3$  and  $\text{ZrO}_2$  phases. From the SEM images, it can be seen that  $\text{ZrO}_2$  and rod-like  $\text{SmAlO}_3$  reinforcements were homogeneously distributed in the microstructure. It was also observed that  $\text{ZrO}_2$  and rod-like  $\text{SmAlO}_3$  phases were mainly located at the grain boundaries. In the  $\text{Al}_2\text{O}_3$ -0.8% $\text{Sm}_2\text{O}_3$ -5% $\text{ZrO}_2$  composite, a reinforcement phase close to the  $\text{Al}_2\text{O}_3$  grain size was



noticed. This is considered to be a secondary phase formed by the reaction of  $\text{Sm}_2\text{O}_3$  and  $\text{ZrO}_2$ . In the sandwich-structured samples, a microstructure similar to that in Figure 3 (b) was obtained since the surface layer was  $\text{Al}_2\text{O}_3$ -0.8% $\text{Sm}_2\text{O}_3$ . Apart from this, abnormal grain growth microstructure was observed in  $\text{Al}_2\text{O}_3$ -0.8% $\text{Sm}_2\text{O}_3$  and sandwich-structured samples..

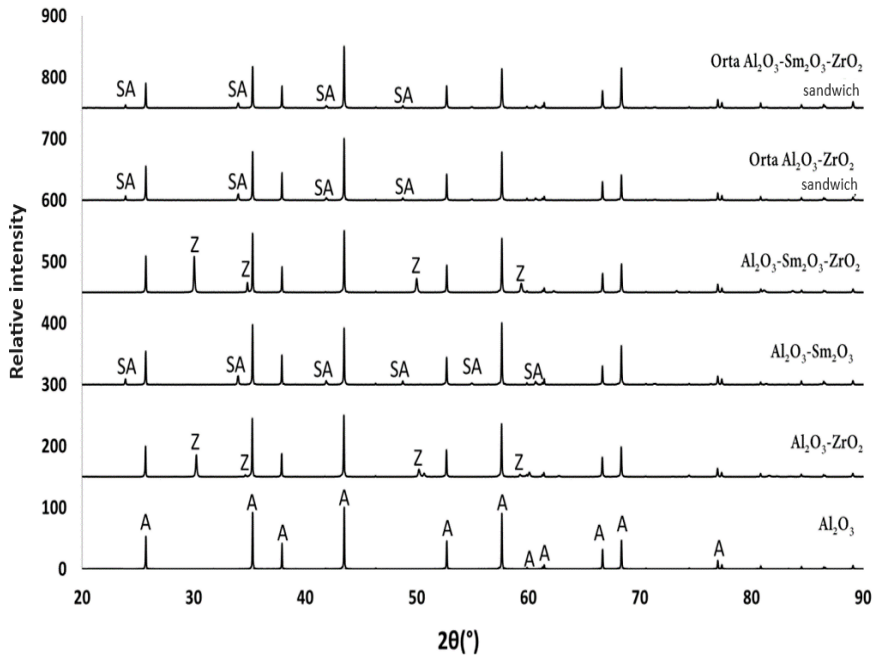


**Figure 2.** Schematic representation of the production process



**Figure 3.** SEM images of pure  $\text{Al}_2\text{O}_3$  (a),  $\text{Al}_2\text{O}_3\text{-}0.8\text{Sm}_2\text{O}_3$  (b),  $\text{Al}_2\text{O}_3\text{-}5\text{ZrO}_2$  (c),  $\text{Al}_2\text{O}_3\text{-}0.8\text{Sm}_2\text{O}_3\text{-}5\text{ZrO}_2$  (d), sandwich with a middle layer of  $\text{Al}_2\text{O}_3\text{-}5\text{ZrO}_2$  (e), sandwich with a middle layer of  $\text{Al}_2\text{O}_3\text{-}0.8\text{Sm}_2\text{O}_3\text{-}5\text{ZrO}_2$  (f).

Figure 4 shows the XRD graphs of the disk samples produced. From XRD graphs, no undesired phase formation was observed in pure  $\text{Al}_2\text{O}_3$ ,  $\text{Al}_2\text{O}_3\text{-ZrO}_2$ , and  $\text{Al}_2\text{O}_3\text{-Sm}_2\text{O}_3$  composites. Due to the composition of  $\text{Al}_2\text{O}_3\text{-SmAlO}_3$  in the upper layer of the sandwich structures and the depth of analysis, a different structure was not determined. In the  $\text{Al}_2\text{O}_3\text{-}0.8\%\text{Sm}_2\text{O}_3\text{-}5\%\text{ZrO}_2$  composite, the peaks belonging to tetragonal zirconia were observed clearly. In addition, the  $\text{Sm}_2\text{Zr}_2\text{O}_7$  phase formed as a result of the dissolution of  $\text{Sm}_2\text{O}_3$  in  $\text{ZrO}_2$  by forming a solid solution was seen by detailed examination of the peaks.



**Figure 4.** The XRD graphs of the disk samples produced.

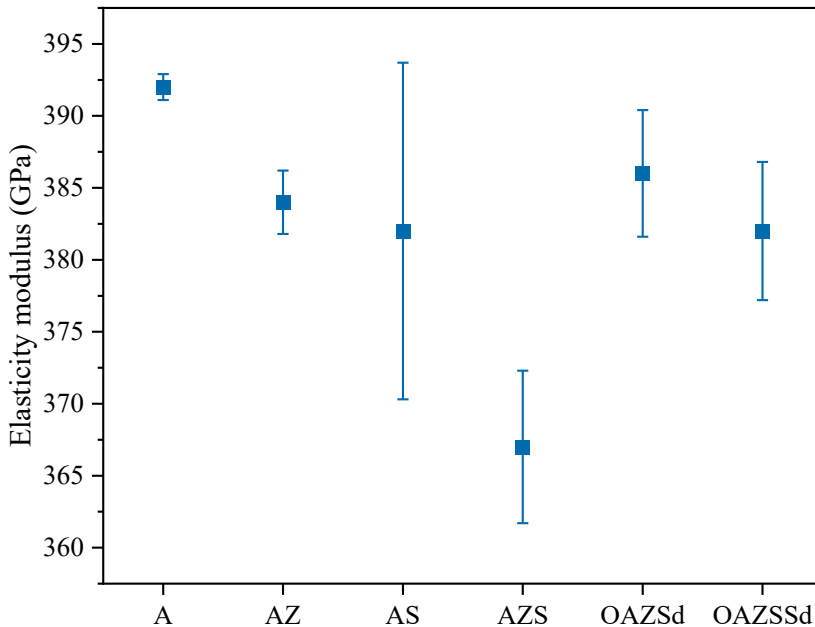
Relative density results of the disc samples are given in Table 1. When the results are analysed; it is seen that the density of pure  $\text{Al}_2\text{O}_3$ ,  $\text{Al}_2\text{O}_3$ -0,8% $\text{Sm}_2\text{O}_3$ , and  $\text{Al}_2\text{O}_3$ -5% $\text{ZrO}_2$  samples is 98,5%. However, it was observed that the density value decreased as a result of the addition of  $\text{Sm}_2\text{O}_3$  and  $\text{ZrO}_2$  together. In sandwich composites, the densification increased (98.6%) in samples with  $\text{Al}_2\text{O}_3$ -5% $\text{ZrO}_2$  as the middle layer. In the samples with  $\text{Al}_2\text{O}_3$ -5% $\text{ZrO}_2$ -0.8% $\text{Sm}_2\text{O}_3$  middle layer, the density value decreased to 97.9%. This is considered to be due to the formation of the second phase formed by the  $\text{ZrO}_2$  and  $\text{Sm}_2\text{O}_3$  reaction.

**Table 1.** The relative density results of disc samples produced

Composition	%Relative Density (Archimedes)	%Relative Density (Volumetrically)
Pure $\text{Al}_2\text{O}_3$ (A)	98.9±0.2	98.5±0.3
$\text{Al}_2\text{O}_3$ -%5 $\text{ZrO}_2$ (AZ)	99.4±0.4	98.5±0.8

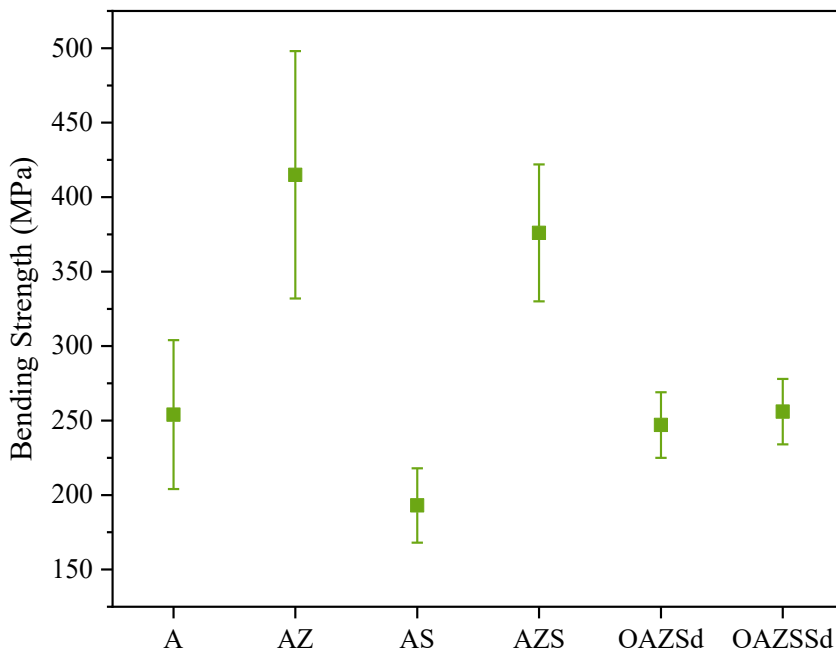
$\text{Al}_2\text{O}_3$ -%0,8 $\text{Sm}_2\text{O}_3$ (AS)	$99.1\pm 0.2$	$98.5\pm 0.4$
$\text{Al}_2\text{O}_3$ -%0,8 $\text{Sm}_2\text{O}_3$ -%5 $\text{ZrO}_2$ (AZS)	$98.3\pm 0.2$	$97.4\pm 0.5$
Middle layer $\text{Al}_2\text{O}_3$ -%5 $\text{ZrO}_2$ sandwich (OAZSd)	$99.4\pm 0.2$	$98.6\pm 0.4$
Middle layer $\text{Al}_2\text{O}_3$ -%0,8 $\text{Sm}_2\text{O}_3$ -%5 $\text{ZrO}_2$ sandwich (OAZSSd)	$98.9\pm 0.4$	$97.9\pm 0.4$

The elastic modulus results of the produced composites are given in Figure 5. The elastic modulus value for pure  $\text{Al}_2\text{O}_3$  decreased from  $392\pm 9$  GPa to  $384\pm 2.2$  GPa with the addition of  $\text{ZrO}_2$ . Similarly, the elastic modulus value decreased with the addition of  $\text{Sm}_2\text{O}_3$  compared to pure  $\text{Al}_2\text{O}_3$ . It was found that the elastic modulus decreased as a result of adding a material with a lower elastic modulus than  $\text{Al}_2\text{O}_3$  to the structure. The lowest elastic modulus was observed in  $\text{Al}_2\text{O}_3$ -5% $\text{ZrO}_2$ -0.8% $\text{Sm}_2\text{O}_3$  ( $367\pm 5.3$  GPa) composite. Since the elastic modulus is directly related to the densification, a higher elastic modulus value was obtained in the samples with  $\text{Al}_2\text{O}_3$ -5% $\text{ZrO}_2$  sandwich structure ( $386\pm 4.4$  GPa) with a high densification ratio compared to the other sandwich structure ( $382\pm 4$  GPa).



**Figure 5.** The elastic modulus results of the produced composites.

Figure 6 illustrates the variation of the flexural test results of pure  $\text{Al}_2\text{O}_3$  and composite samples. Bending strength increased by 63.4% with 5%  $\text{ZrO}_2$  addition by volume. However, the lowest bending strength value was obtained for 0.8 vol.%  $\text{Sm}_2\text{O}_3$  addition. This is due to the formation of a large-grained microstructure with  $\text{Sm}_2\text{O}_3$  addition. In the  $\text{Al}_2\text{O}_3$ -0.8% $\text{Sm}_2\text{O}_3$ -5% $\text{ZrO}_2$  composite, high bending strength ( $376\pm 46$  MPa) was obtained due to the presence of  $\text{ZrO}_2$ . In the sandwich structure composites, strength values close to pure  $\text{Al}_2\text{O}_3$  samples were obtained. The presence of  $\text{ZrO}_2$  in the middle layers of the sandwich structures ensured that the flexural strength values of the samples were higher compared to  $\text{Al}_2\text{O}_3$ -0.8% $\text{Sm}_2\text{O}_3$  composites.



**Figure 6.** The variation of the bending test results of pure  $\text{Al}_2\text{O}_3$  and composite samples.

## CONCLUSIONS

The effect of different volume ratios of additives ( $\text{ZrO}_2$  and  $\text{Sm}_2\text{O}_3$ ) on the microstructure and mechanical properties of  $\text{Al}_2\text{O}_3$  and  $\text{Al}_2\text{O}_3$ -based sandwich structures was investigated. The results obtained in the study are summarized below:

- As a result of SEM analysis, it was seen that the additives were homogeneously distributed in the microstructure. At the same time,  $ZrO_2$  and rod-like  $SmAlO_3$  phases were found to be located at the grain boundaries. Since the top and bottom layers in the sandwich structure samples are  $Al_2O_3-0.8\%Sm_2O_3$ , the microstructure is similar to the structure of this composition. In addition, a large-grained structure was encountered in both sandwich-structured samples and  $Al_2O_3-0.8\%Sm_2O_3$  samples.
- The highest densification after sintering was obtained in a sandwich composite with a middle layer of  $Al_2O_3-5\%ZrO_2$ . The highest elastic modulus ( $392\pm 9$  GPa) was found in the pure  $Al_2O_3$  sample, while the highest flexural strength ( $415\pm 83$  MPa) was achieved in  $Al_2O_3-5\%ZrO_2$  samples.

#### **ACKNOWLEDGMENT**

This work was supported by the Scientific and Technical Research Council of Turkey -TUBITAK through the project no 122M179. The authors also thank Dr. Halil İbrahim Çetintaş for his assistance in the SEM analysis of this study.

## REFERENCES

- Daguano, J. K. M. F., Santos, C., Souza, R. C., Balestra, R. M., Strecker, K., & Elias, C. N. (2007). Properties of ZrO<sub>2</sub>-Al<sub>2</sub>O<sub>3</sub> composite as a function of isothermal holding time. *International Journal of Refractory Metals and Hard Materials*, 25(5–6), 374–379. Retrieved from <https://doi.org/10.1016/j.ijrmhm.2006.12.005>
- Huang, C. Y., & Chen, Y. L. (2016). Effect of mechanical properties on the ballistic resistance capability of Al<sub>2</sub>O<sub>3</sub>-ZrO<sub>2</sub> functionally graded materials. *Ceramics International*, 42(11), 12946–12955. Retrieved from <https://doi.org/10.1016/j.ceramint.2016.05.067>
- Justi, J., Kammer, E. H., Neckel, L., Lóh, N. J., Trindade, W., Silva, A. O., De Noni, A. (2017). Ballistic performance of Al<sub>2</sub>O<sub>3</sub> mosaic armors with gap-filling materials. *Ceramics International*, 43(2), 2697–2704. Retrieved from <https://doi.org/10.1016/j.ceramint.2016.11.087>
- Shi, S., Cho, S., Goto, T., & Sekino, T. (2020). Ti and SmAlO<sub>3</sub> co-affected Al<sub>2</sub>O<sub>3</sub> ceramics: Microstructure, electrical and mechanical properties. *Journal of Alloys and Compounds*, 835. Retrieved from <https://doi.org/10.1016/j.jallcom.2020.155427>
- Zhou, Z., Wang, Z., Yi, Y., Jiang, S., Wang, G., & Chen, J. (2011). Properties and micro-structure of ZrO<sub>2</sub>-Al<sub>2</sub>O<sub>3</sub> composites with three-layer structure. *Composites Part B: Engineering*, 42(5), 1271–1275. Retrieved from <https://doi.org/10.1016/j.compositesb.2011.02.003>





## **CHAPTER 11**

### **DENSIFICATION AND FRACTURE STRENGTH PROPERTIES OF AL<sub>2</sub>O<sub>3</sub> BASED ZRO<sub>2</sub> AND SM<sub>2</sub>O<sub>3</sub> CONTAINING SANDWICH CERAMIC COMPOSITES**

Tuğba ŞANLI<sup>1</sup>

Dr. Öğr. Üyesi Betül KAFKASLIOĞLU YILDIZ<sup>2</sup>

Arş. Gör. Elif IŞIK<sup>3</sup>

Prof. Dr. Yahya Kemal TÜR<sup>4</sup>

---

<sup>1</sup>Sivas University of Science and Technology, Institute of Graduate Studies, Department of Defence Technology, Sivas, Turkey..<sup>1</sup>ORCID ID: <https://orcid.org/0009-0003-7260-6650>

<sup>1</sup> tugbasanli0921@gmail.com

<sup>2</sup> Sivas University of Science and Technology, Faculty of Engineering and Natural Sciences, Department of Metallurgical and Materials Engineering, Sivas, Turkey.

<sup>2</sup>ORCID ID: <https://orcid.org/0000-0002-6527-2918>

<sup>2</sup> bkyildiz@sivas.edu.tr

<sup>3</sup> Sivas University of Science and Technology, Faculty of Engineering and Natural Sciences, Department of Metallurgical and Materials Engineering, Sivas, Turkey.

<sup>3</sup>ORCID ID: <https://orcid.org/0000-0001-8289-9512>

<sup>3</sup> elif.isik@sivas.edu.tr

<sup>4</sup> Gebze Technical University, Faculty of Engineering, Department of Materials Science and Engineering, Kocaeli, Turkey.

<sup>4</sup>ORCID ID: <https://orcid.org/0000-0002-9521-8875>

<sup>4</sup>yktur@gtu.edu.tr



## INTRODUCTION

Alumina ( $\text{Al}_2\text{O}_3$ ) ceramics is a material with high mechanical, tribological, thermal, and chemical properties that enable its use in many applications (Jiusti et al., 2017). Zirconia ( $\text{ZrO}_2$ ) is a ceramic material that shows different crystal structures at different temperatures. The transformation between these crystal structures (tetragonal-monoclinic) ensures toughening. Therefore, zirconia-reinforced alumina composites are of interest to many researchers and the disadvantages of  $\text{Al}_2\text{O}_3$  can be overcome by  $\text{ZrO}_2$  (Daguano et al., 2007). Samarium oxide ( $\text{Sm}_2\text{O}_3$ ) is a rare earth oxide with high melting temperature, dielectric constant, and thermal stability. The reaction caused by the addition of  $\text{Sm}_2\text{O}_3$  to the  $\text{Al}_2\text{O}_3$  structure results in the formation of the  $\text{SmAlO}_3$  phase. This phase with a rod-like structure can act as short fibers and increase the strength and toughness of  $\text{Al}_2\text{O}_3$  ceramics (Shi et al., 2020).

Laminated ceramics are formed by combining several layers of ceramics on top of each other. There is a thermal expansion difference between the ceramics used in the layers forming the laminated structure. Due to the difference in thermal expansion, residual compressive stresses occur on the surfaces. Because these stresses will play a role in preventing crack propagation, mechanical properties can be improved (Huang & Chen, 2016).

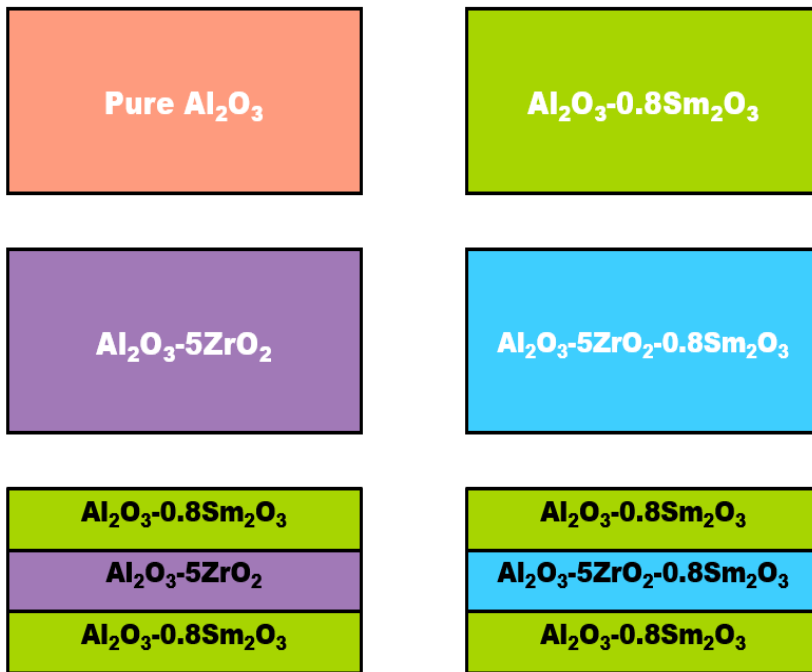
Zhaou et al. aimed to increase toughness and strength by producing an  $\text{Al}_2\text{O}_3$ - $\text{ZrO}_2$  composite in a three-layer structure. While  $\text{Al}_2\text{O}_3$ -5% $\text{ZrO}_2$  composite was used as the middle layer, the  $\text{ZrO}_2$  content in the surface layer was varied as 20, 30, and 40 wt%. As a result of the study, the highest strength and fracture toughness were achieved in the sandwich structure with a surface layer containing 30 wt%  $\text{ZrO}_2$  (Zhou et al., 2011).

When the literature studies were examined; it was seen that there were not many studies related to laminated structures. For this purpose, in this study, the effects of samarium oxide ( $\text{Sm}_2\text{O}_3$ ) and zirconium oxide ( $\text{ZrO}_2$ ) additives at different volume ratios on the microstructure and mechanical properties of  $\text{Al}_2\text{O}_3$  and  $\text{Al}_2\text{O}_3$ -based sandwich structures were examined separately. Especially, the effect of laminated structure and reinforcement materials on densification and mechanical properties were investigated.

## MATERIALS AND METHOD

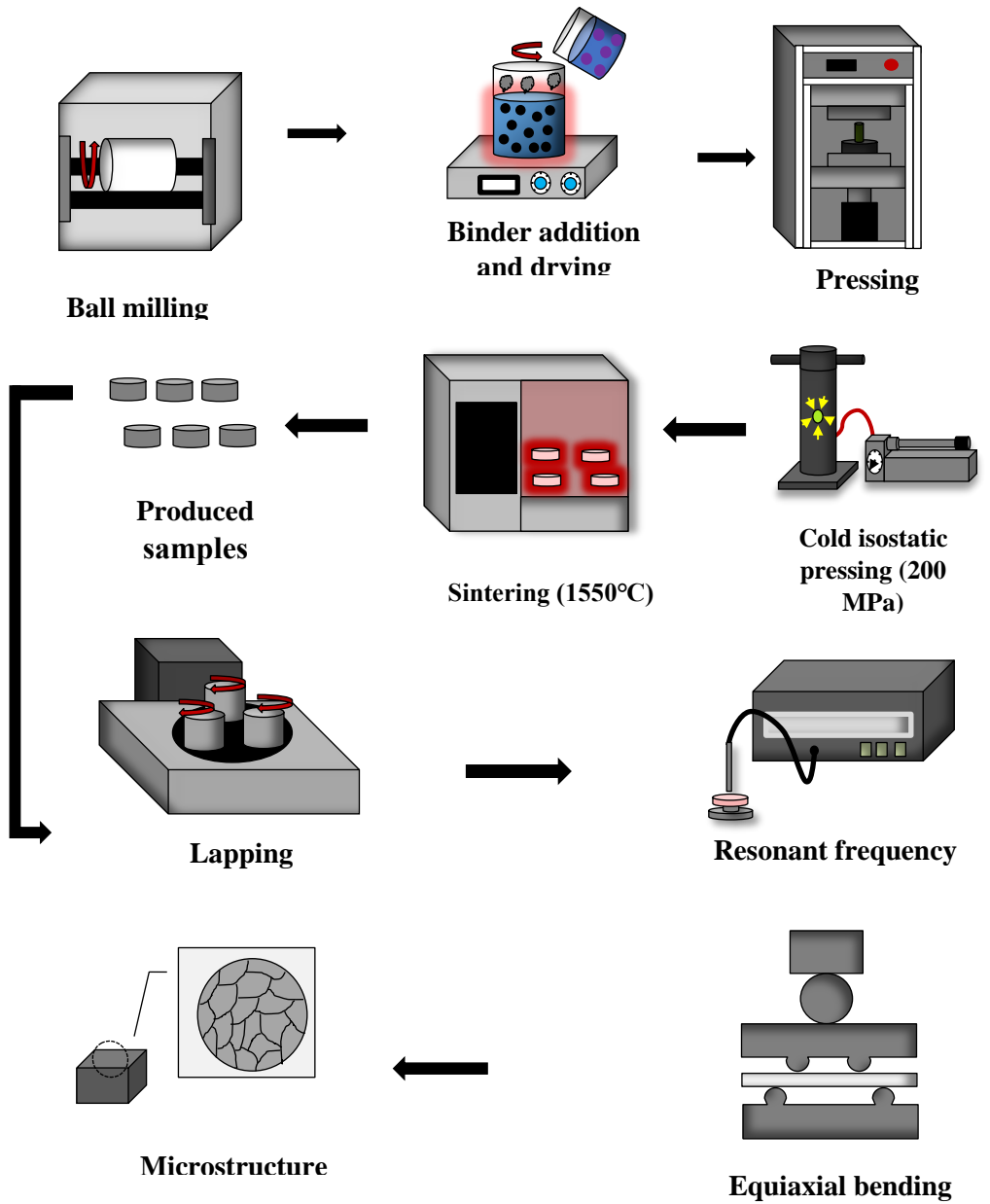
In this study,  $\alpha$ - $\text{Al}_2\text{O}_3$  powder (Alfa Aesar, Germany) with a grain size of 0.25-0.45  $\mu\text{m}$  with 99.5% purity was chosen as the matrix material.  $\text{Sm}_2\text{O}_3$  (99.95% purity and  $\sim 50$  nm powder size, Nanografi, Turkey) and  $\text{ZrO}_2$  (%3 mol yttria stabilize, MSE technology, Turkey) were preferred as reinforcement materials. Polyacrylic acid (Darvan 821A, MSE Tech Co. Ltd., Turkey) was used as a dispersant while the binder solution was prepared with polyvinyl alcohol (PVA, Sigma Aldrich) and glycerol (Sigma Aldrich).

In the study, both  $\text{Al}_2\text{O}_3$ -based sandwich structures and  $\text{Al}_2\text{O}_3$ -based samples with different volume fractions of  $\text{Sm}_2\text{O}_3$  and  $\text{ZrO}_2$  were fabricated. Firstly, the reinforcement materials and  $\text{Al}_2\text{O}_3$  powder were mixed in distilled water with 0.5 wt% polyacrylic acid in a ball mill for 24 hours. Simultaneously, a binder solution with 2 wt% polymer (PVA + glycerol) was prepared. After the binder solution was added to the prepared powder mixture, mixing and drying were performed using a heated magnetic stirrer. The dried powders were crushed in an agate mortar and sieved through a 90  $\mu\text{m}$  sieve to prepare for shaping. Then, the powders were shaped in a uniaxial hydraulic press using a 35 mm diameter stainless steel mold. During the shaping of the sandwich samples, the powder of each layer was poured sequentially into the mold and each layer was pre-pressed with a pressure of 20 MPa. After the last layer was spread and pre-pressurized, a final pressure of 100 MPa was applied. Non-sandwich samples were shaped under a pressure of 40 MPa. Then, all samples in disc form were cold isostatic pressed at a pressure of 200 MPa. After binder burn-out at 600°C for 2 hours, the samples were sintered at 1550°C for 2 hours pressurelessly in air environment. The lapping process was performed to parallelize and ground the surfaces of the produced samples. The sample compositions produced are presented in Figure 1.



**Figure 1.** Compositions of the produced samples.

The bulk density measurements of the produced samples were carried out both volumetrically and using the Archimedes method. The resonance frequency method was used for elastic modulus measurements (ASTM C1259). Flexural strength was determined using the equibiaxial flexure strength test (ASTM C1499). SEM analyses were performed to examine microstructural properties. The phase and crystal structure of the samples were analyzed by XRD analysis. A schematic representation of the production process is given in Figure 2.

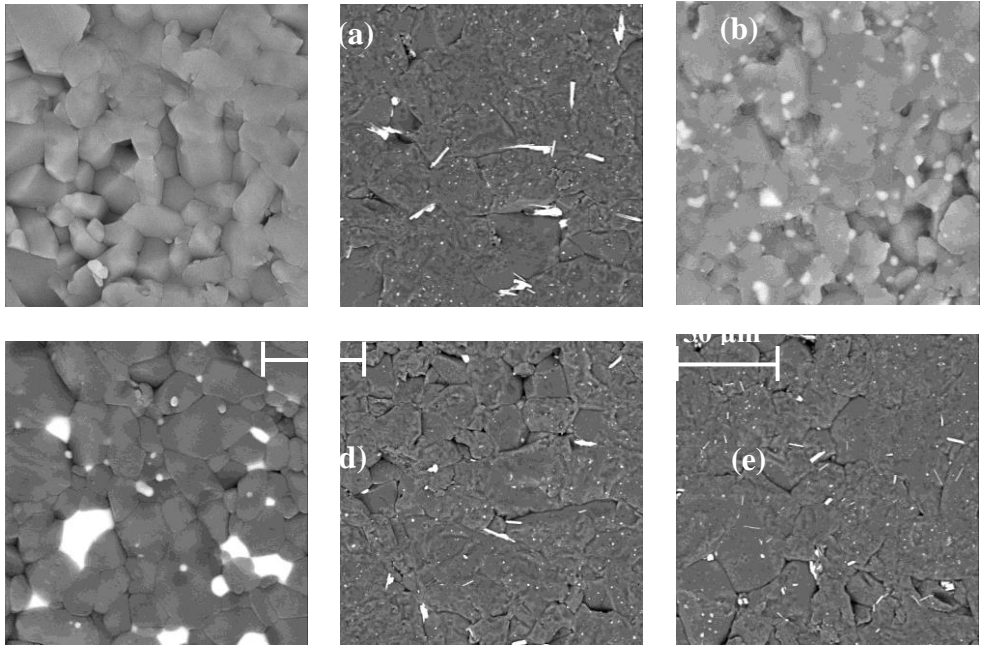


**Figure 2.** Schematic representation of the production process.

## RESULTS AND DISCUSSIONS

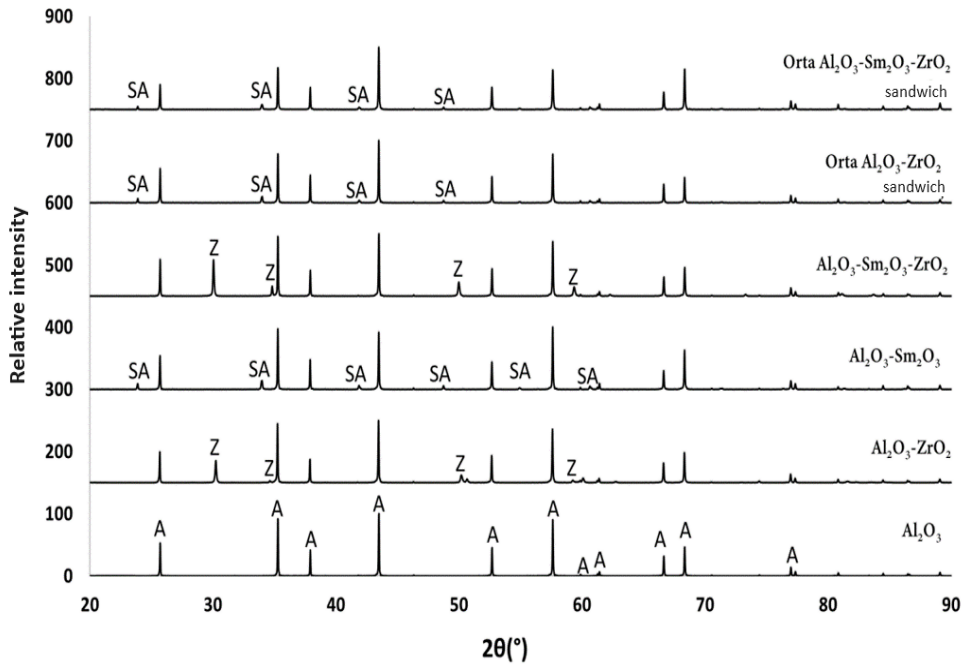
Figure 3 illustrates the SEM images of the surfaces of the produced samples after thermal etching at 1450°C/90 min. In the figures, the gray regions belong to  $\text{Al}_2\text{O}_3$  and the white regions belong to the additives  $\text{Sm}_2\text{O}_3$  and  $\text{ZrO}_2$  phases. From the SEM images, it can be seen that  $\text{ZrO}_2$  and rod-like  $\text{SmAlO}_3$  reinforcements were homogeneously distributed in the microstructure. It was also observed that  $\text{ZrO}_2$  and rod-like  $\text{SmAlO}_3$  phases were mainly located at the grain boundaries. In the  $\text{Al}_2\text{O}_3$ -0.8% $\text{Sm}_2\text{O}_3$ -5% $\text{ZrO}_2$  composite, a reinforcement phase close to the  $\text{Al}_2\text{O}_3$  grain size was noticed. This is considered to be a secondary phase formed by the reaction of  $\text{Sm}_2\text{O}_3$  and  $\text{ZrO}_2$ . In the sandwich-structured samples, a microstructure similar to that in Figure 3 (b) was obtained since the surface layer was  $\text{Al}_2\text{O}_3$ -0.8% $\text{Sm}_2\text{O}_3$ . Apart from this, abnormal grain growth microstructure was observed in  $\text{Al}_2\text{O}_3$ -0.8% $\text{Sm}_2\text{O}_3$  and sandwich-structured samples.





**Figure 3.** SEM images of pure  $\text{Al}_2\text{O}_3$  (a),  $\text{Al}_2\text{O}_3\text{-}0.8\text{Sm}_2\text{O}_3$  (b),  $\text{Al}_2\text{O}_3\text{-}5\text{ZrO}_2$  (c),  $\text{Al}_2\text{O}_3\text{-}0.8\text{Sm}_2\text{O}_3\text{-}5\text{ZrO}_2$  (d), sandwich with a middle layer of  $\text{Al}_2\text{O}_3\text{-}5\text{ZrO}_2$  (e), sandwich with a middle layer of  $\text{Al}_2\text{O}_3\text{-}0.8\text{Sm}_2\text{O}_3\text{-}5\text{ZrO}_2$  (f).

Figure 4 shows the XRD graphs of the disk samples produced. From XRD graphs, no undesired phase formation was observed in pure  $\text{Al}_2\text{O}_3$ ,  $\text{Al}_2\text{O}_3\text{-ZrO}_2$ , and  $\text{Al}_2\text{O}_3\text{-Sm}_2\text{O}_3$  composites. Due to the composition of  $\text{Al}_2\text{O}_3\text{-SmAlO}_3$  in the upper layer of the sandwich structures and the depth of analysis, a different structure was not determined. In the  $\text{Al}_2\text{O}_3\text{-}0.8\%\text{Sm}_2\text{O}_3\text{-}5\%\text{ZrO}_2$  composite, the peaks belonging to tetragonal zirconia were observed clearly. In addition, the  $\text{Sm}_2\text{Zr}_2\text{O}_7$  phase formed as a result of the dissolution of  $\text{Sm}_2\text{O}_3$  in  $\text{ZrO}_2$  by forming a solid solution was seen by detailed examination of the peaks.



**Figure 4.** The XRD graphs of the disk samples produced.

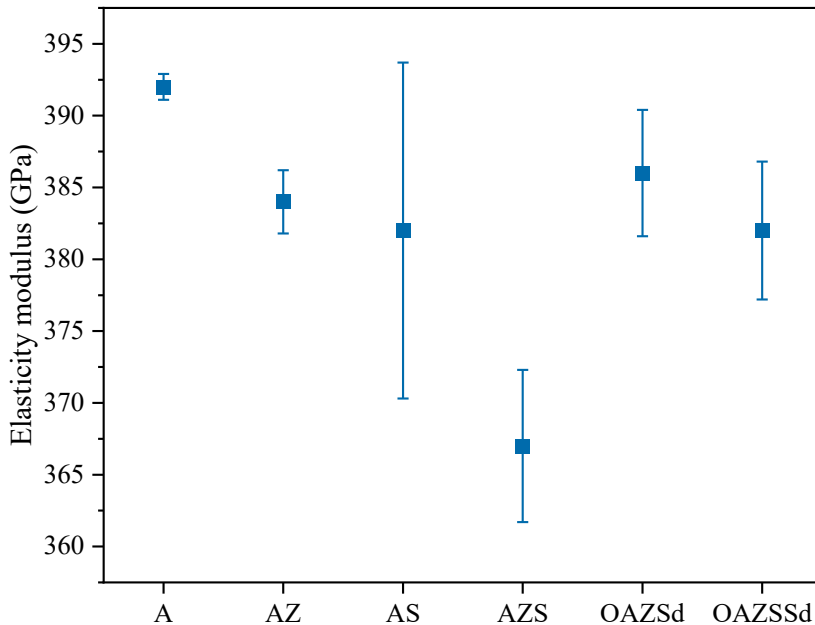
Relative density results of the disc samples are given in Table 1. When the results are analysed; it is seen that the density of pure Al<sub>2</sub>O<sub>3</sub>, Al<sub>2</sub>O<sub>3</sub>-0,8%Sm<sub>2</sub>O<sub>3</sub>, and Al<sub>2</sub>O<sub>3</sub>-5%ZrO<sub>2</sub> samples is 98,5%. However, it was observed that the density value decreased as a result of the addition of Sm<sub>2</sub>O<sub>3</sub> and ZrO<sub>2</sub> together. In sandwich composites, the densification increased (98.6%) in samples with Al<sub>2</sub>O<sub>3</sub>-5%ZrO<sub>2</sub> as the middle layer. In the samples with Al<sub>2</sub>O<sub>3</sub>-5%ZrO<sub>2</sub>-0.8%Sm<sub>2</sub>O<sub>3</sub> middle layer, the density value decreased to 97.9%. This is considered to be due to the formation of the second phase formed by the ZrO<sub>2</sub> and Sm<sub>2</sub>O<sub>3</sub> reaction.

**Table 1.** The relative density results of disc samples produced

Composition	%Relative Density (Archimedes)	%Relative Density (Volumetrically)
Pure Al <sub>2</sub> O <sub>3</sub> (A)	98.9±0.2	98.5±0.3
Al <sub>2</sub> O <sub>3</sub> -%5ZrO <sub>2</sub> (AZ)	99.4±0.4	98.5±0.8

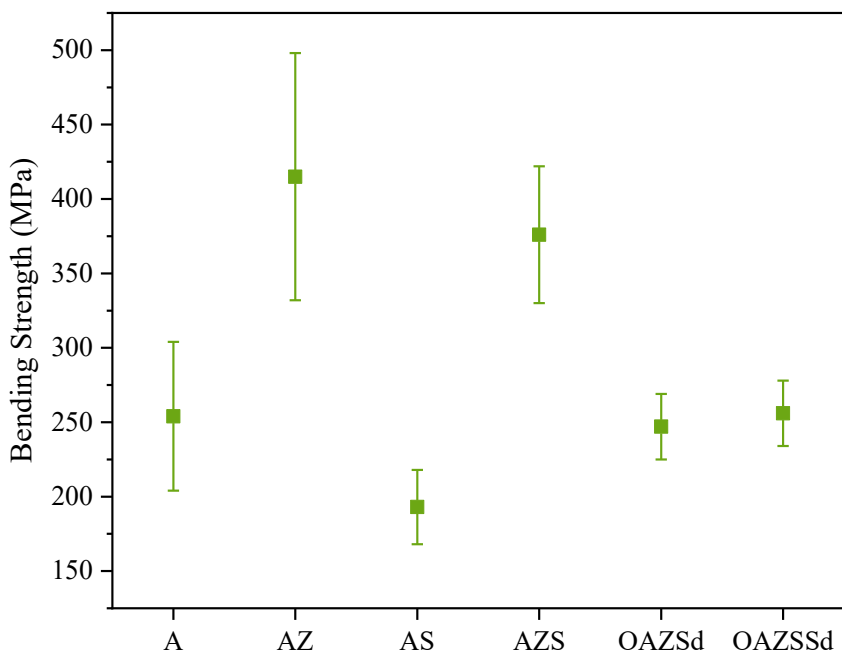
$\text{Al}_2\text{O}_3$ -%0,8 $\text{Sm}_2\text{O}_3$ (AS)	$99.1\pm 0.2$	$98.5\pm 0.4$
$\text{Al}_2\text{O}_3$ -%0,8 $\text{Sm}_2\text{O}_3$ -%5 $\text{ZrO}_2$ (AZS)	$98.3\pm 0.2$	$97.4\pm 0.5$
Middle layer $\text{Al}_2\text{O}_3$ -%5 $\text{ZrO}_2$ sandwich (OAZSd)	$99.4\pm 0.2$	$98.6\pm 0.4$
Middle layer $\text{Al}_2\text{O}_3$ -%0,8 $\text{Sm}_2\text{O}_3$ -%5 $\text{ZrO}_2$ sandwich (OAZSSd)	$98.9\pm 0.4$	$97.9\pm 0.4$

The elastic modulus results of the produced composites are given in Figure 5. The elastic modulus value for pure  $\text{Al}_2\text{O}_3$  decreased from  $392\pm 9$  GPa to  $384\pm 2.2$  GPa with the addition of  $\text{ZrO}_2$ . Similarly, the elastic modulus value decreased with the addition of  $\text{Sm}_2\text{O}_3$  compared to pure  $\text{Al}_2\text{O}_3$ . It was found that the elastic modulus decreased as a result of adding a material with a lower elastic modulus than  $\text{Al}_2\text{O}_3$  to the structure. The lowest elastic modulus was observed in  $\text{Al}_2\text{O}_3$ -5% $\text{ZrO}_2$ -0.8% $\text{Sm}_2\text{O}_3$  ( $367\pm 5.3$  GPa) composite. Since the elastic modulus is directly related to the densification, a higher elastic modulus value was obtained in the samples with  $\text{Al}_2\text{O}_3$ -5% $\text{ZrO}_2$  sandwich structure ( $386\pm 4.4$  GPa) with a high densification ratio compared to the other sandwich structure ( $382\pm 4$  GPa).



**Figure 5.** The elastic modulus results of the produced composites.

Figure 6 illustrates the variation of the flexural test results of pure  $\text{Al}_2\text{O}_3$  and composite samples. Bending strength increased by 63.4% with 5%  $\text{ZrO}_2$  addition by volume. However, the lowest bending strength value was obtained for 0.8 vol.%  $\text{Sm}_2\text{O}_3$  addition. This is due to the formation of a large-grained microstructure with  $\text{Sm}_2\text{O}_3$  addition. In the  $\text{Al}_2\text{O}_3$ -0.8% $\text{Sm}_2\text{O}_3$ -5% $\text{ZrO}_2$  composite, high bending strength ( $376\pm 46$  MPa) was obtained due to the presence of  $\text{ZrO}_2$ . In the sandwich structure composites, strength values close to pure  $\text{Al}_2\text{O}_3$  samples were obtained. The presence of  $\text{ZrO}_2$  in the middle layers of the sandwich structures ensured that the flexural strength values of the samples were higher compared to  $\text{Al}_2\text{O}_3$ -0.8% $\text{Sm}_2\text{O}_3$  composites.



**Figure 6.** The variation of the bending test results of pure  $\text{Al}_2\text{O}_3$  and composite samples.

## CONCLUSIONS

The effect of different volume ratios of additives ( $\text{ZrO}_2$  and  $\text{Sm}_2\text{O}_3$ ) on the microstructure and mechanical properties of  $\text{Al}_2\text{O}_3$  and  $\text{Al}_2\text{O}_3$ -based sandwich structures was investigated. The results obtained in the study are summarized below:

- As a result of SEM analysis, it was seen that the additives were homogeneously distributed in the microstructure. At the same time,  $ZrO_2$  and rod-like  $SmAlO_3$  phases were found to be located at the grain boundaries. Since the top and bottom layers in the sandwich structure samples are  $Al_2O_3-0.8\%Sm_2O_3$ , the microstructure is similar to the structure of this composition. In addition, a large-grained structure was encountered in both sandwich-structured samples and  $Al_2O_3-0.8\%Sm_2O_3$  samples.
- The highest densification after sintering was obtained in a sandwich composite with a middle layer of  $Al_2O_3-5\%ZrO_2$ . The highest elastic modulus ( $392\pm 9$  GPa) was found in the pure  $Al_2O_3$  sample, while the highest flexural strength ( $415\pm 83$  MPa) was achieved in  $Al_2O_3-5\%ZrO_2$  samples.

#### **ACKNOWLEDGMENT**

This work was supported by the Scientific and Technical Research Council of Turkey -TUBITAK through the project no 122M179. The authors also thank Dr. Halil İbrahim Çetintaş for his assistance in the SEM analysis of this study.

## REFERENCES

- Daguano, J. K. M. F., Santos, C., Souza, R. C., Balestra, R. M., Strecker, K., & Elias, C. N. (2007). Properties of  $ZrO_2$ - $Al_2O_3$  composite as a function of isothermal holding time. *International Journal of Refractory Metals and Hard Materials*, 25(5–6), 374–379. Retrieved from <https://doi.org/10.1016/j.ijrmhm.2006.12.005>
- Huang, C. Y., & Chen, Y. L. (2016). Effect of mechanical properties on the ballistic resistance capability of  $Al_2O_3$ - $ZrO_2$  functionally graded materials. *Ceramics International*, 42(11), 12946–12955. Retrieved from <https://doi.org/10.1016/j.ceramint.2016.05.067>
- Jiusti, J., Kammer, E. H., Neckel, L., Lóh, N. J., Trindade, W., Silva, A. O., De Noni, A. (2017). Ballistic performance of  $Al_2O_3$  mosaic armors with gap-filling materials. *Ceramics International*, 43(2), 2697–2704. Retrieved from <https://doi.org/10.1016/j.ceramint.2016.11.087>
- Shi, S., Cho, S., Goto, T., & Sekino, T. (2020). Ti and  $SmAlO_3$  co-affected  $Al_2O_3$  ceramics: Microstructure, electrical and mechanical properties. *Journal of Alloys and Compounds*, 835. Retrieved from <https://doi.org/10.1016/j.jallcom.2020.155427>
- Zhou, Z., Wang, Z., Yi, Y., Jiang, S., Wang, G., & Chen, J. (2011). Properties and micro-structure of  $ZrO_2$ - $Al_2O_3$  composites with three-layer structure. *Composites Part B: Engineering*, 42(5), 1271–1275. Retrieved from <https://doi.org/10.1016/j.compositesb.2011.02.003>

